Title
Hard X-ray Constraints on Faint Transient Events in the Solar Corona

Author
Marsh, Andrew

Publication Date
2017

UNIVERSITY OF CALIFORNIA
SANTA CRUZ

HARD X-RAY CONSTRAINTS ON FAINT TRANSIENT EVENTS IN THE SOLAR CORONA

A dissertation submitted in partial satisfaction of the
requirements for the degree of

DOCTOR OF PHILOSOPHY

in

PHYSICS

by

Andrew J. Marsh

June 2017

The Dissertation of Andrew J. Marsh
is approved:

Professor David M. Smith, Chair

Professor Lindsay Glesener

Professor David A. Williams

Tyrus Miller
Vice Provost and Dean of Graduate Studies

Table of Contents

List of Figures vi

List of Tables xv

Abstract xvi

Dedication xviii

Acknowledgments xix

1 Introduction 1
- 1.1 Origins . . . 1
- 1.2 Structure of the Sun . . . 2
  - 1.2.1 The Interior . . . 2
  - 1.2.2 Lower Atmosphere . . . 4
  - 1.2.3 Outer Atmosphere (Corona) . . . 5
- 1.3 Solar Cycle . . . 8
- 1.4 Summary . . . 9

2 Flares, Transient Events and Coronal Heating 12
- 2.1 Flare Physics . . . 12
  - 2.1.1 Standard Flare Model . . . 13
  - 2.1.2 Magnetic Reconnection . . . 14
  - 2.1.3 Particle Acceleration . . . 17
- 2.2 Emission from the Solar Corona . . . 20
  - 2.2.1 Thermal Bremsstrahlung . . . 21
  - 2.2.2 Non-thermal Bremsstrahlung . . . 23
  - 2.2.3 Emission Lines . . . 24
- 2.3 Observing the Corona . . . 27
  - 2.3.1 Instruments . . . 27
  - 2.3.2 Non-Flaring Active Regions . . . 30
  - 2.3.3 Flares . . . 31

2.3.4 The Quiet Sun . . . 33
2.4 The Coronal Heating Problem . . . 34
2.4.1 Flare Heating . . . 37
2.4.2 Nanoflare Heating . . . 38

3 Imaging Hard X-rays with Focusing Optics 42
3.1 Focusing Optics . . . 42
3.2 FOXSI . . . 48
3.2.1 Optics . . . 48
3.2.2 Detectors . . . 49
3.2.3 Science Goals . . . 49
3.2.4 Science Results . . . 50
3.3 NuSTAR . . . 51
3.3.1 Optics . . . 52
3.3.2 Detectors . . . 52
3.3.3 Science Goals and Results . . . 53

4 First *NuSTAR* Limits on Quiet Sun Hard X-Ray Transient Events 67
4.1 Introduction . . . 68
4.2 Solar Observing with *NuSTAR* . . . 70
4.3 Analysis and Results . . . 71
4.3.1 Data reduction . . . 71
4.3.2 Adding the telescopes . . . 73
4.3.3 Transient Search . . . 74
4.3.4 Low Energy (Thermal) Limits . . . 77
4.3.5 High Energy Limits . . . 79
4.4 Discussion . . . 80
4.4.1 Event Duration and Flux Loss . . . 80
4.4.2 Coronal Heating . . . 81
4.4.3 Future Observations . . . 81

5 Hard X-Ray Constraints on Small-Scale Coronal Heating Events 83
5.1 Introduction . . . 84
5.2 Solar Observations with *NuSTAR* and *FOXSI* . . . 88
5.3 Methods . . . 90
5.3.1 Parameters and Their Selection . . . 90
5.3.2 Constraints on the Nanoflare Parameter Space . . . 98
5.4 Results and Discussion . . . 102
5.5 Conclusions . . . 105

6 Future Work and Conclusions **108**
6.1 Future Work 108
6.2 Conclusions 111

Bibliography **112**

List of Figures

1.1 The layers of the Sun from the center to the outer atmosphere. The photosphere, chromosphere, and corona appear as they do to imaging instruments designed to see each specific layer. Images cannot be made of the solar interior. Image courtesy of NASA. 3
1.2 (Left) The solar photosphere imaged in visible light by the *SOHO* satellite. Several sunspot groups are visible near the equator, with less visible structure towards the poles. (Right) High-resolution image of a sunspot and the surrounding granulation, taken by the Solar Optical Telescope onboard the *Hinode* mission. The dimensions of this image are 218×109 arcseconds^2, which is approximately $166{,}000\times83{,}000$ kilometers^2. Images courtesy of NASA. 5
1.3 Temperature and density models of the chromosphere (Fontenla et al. 1990; FAL-C model) and lower corona (Gabriel 1976). At the transition region the temperature suddenly rises and the density suddenly drops by orders of magnitude. This is also the boundary between partial and full plasma ionization, indicated by the much steeper drop in the hydrogen density than the electron density. Figure from Aschwanden (2004). 6
1.4 Loop structures in the corona imaged by the *SDO*/AIA instrument at 171 Å. The plasma seen in this image ranges in temperature from $\sim$0.3 to 2 MK. Image courtesy of NASA. 7
1.5 Line-of-sight magnetic field maps (magnetograms) for an active region (left) and a quiet Sun region (right), measured with the *Hinode* satellite. Black and white indicate negative and positive magnetic polarities (into and out of the page, respectively). The magnetic field strength is measured at the photosphere in this image. Figure from Iida (2012) 10

1.6 (Left) Full-Sun images from the *Yohkoh*/SXT X-ray telescope over the course of 10 years (1992 January 8 to 1999 July 25). The X-ray flux is significantly higher at solar maximum. (Right) Full-Sun magnetograms recorded with the Vacuum Telescope at Kitt Peak National Observatory over the same period as the X-ray images. White and black represent positive and negative magnetic field polarity (parallel to the line-of-sight). Blue indicates regions with zero field. Figures from Aschwanden (2004). 11

2.1 The standard model of solar flares. Magnetic reconnection in the corona is caused by a rising flux rope that subsequently erupts as a CME. This causes the acceleration of particles, many of which stream down magnetic loops to their footpoints. Plasma is heated at the footpoints and subsequently rises into the corona. Typical locations of HXR sources are indicated by black circles; for a detailed discussion see Section 2.3.3. Figure from Christe et al. (2017). 13

2.2 (Left) Sweet-Parker reconnection geometry with a long, narrow diffusion region. (Right) Petschek reconnection geometry with a symmetrical diffusion region.(Zweibel & Yamada 2009). 15

2.3 Magnetic reconnection at different times during a solar flare on 2011 August 17. The white line in each frame marks the edge of the photosphere, and image coordinates are in solar arcseconds. (Top) *SDO*/AIA images at 211, 193, 171 and 304 Å show inflowing loops with temperatures between ∼0.05 and 2 MK (Middle) Same images as top row, with images from a minute earlier subtracted. White and black indicate increases and decreases in intensity, respectively. The red line marks the initial location where inflowing loops seem to merge and disappear; red arrows show the inflow directions. (Bottom) AIA images at 131 Å show plasma heated to ∼10 MK at the center of the inflowing loops. Co-temporal X-ray images from *RHESSI* (not shown) provide additional evidence for plasma heating following reconnection. The observed (unitless) reconnection rates $v_{\rm in}/v_{\rm out}$ for this event were 0.05–0.5, with inflow / outflow velocities ranging from ∼few to ∼100 km s^{-1}. Figure from Su et al. (2013). 18

2.4 The observed solar flux spectrum per unit wavelength (thick line). The thin line is a blackbody spectrum of temperature T = 5762 K. Figure from Aschwanden (2004). 21

2.5 Example emission measure distribution from *Hinode*/EIS observations of flare footpoints. (Left) Temperature response functions for each spectral line that was used in this analysis, calculated using coronal abundances, the CHIANTI 7.0 ionization equilibrium, and a constant density of 10^{11}cm^{3}. (Right) Emission measure distribution generated from the spectral lines in the left panel. The colored curves are known as EM loci and indicate the maximum possible emission for each line. Figure from (Graham et al. 2013). 26
2.6 (Left) A solar flare imaged by *RHESSI* with a standard loop plus footpoints geometry. Footpoint emission is generally higher in energy. Figure from Krucker et al. (2008) (Right) *RHESSI* spectrum of a large flare including a thermal component (red), a non-thermal power law (violet) and an ensemble of gamma-ray spectral lines (blue). The majority of flares observed by *RHESSI* do not have detectable emission above 100 keV. Figure from Lin (2011). 28
2.7 Two *GOES* time series from different parts of the solar cycle. (Left) *GOES* flux approaching the current solar minimum. (Right) *GOES* flux towards the end of solar maximum in solar cycle 23. Images courtesy of NOAA/SWPC. 29
2.8 Flare locations from the *RHESSI* HXR satellite and the *Nobeyama* radio telescope over a fifteen year period beginning in 2002. Notably all flares occur at fairly low latitudes, corresponding to the locations of active regions. A greater number of flares is seen on the limb due to projection effects. All events and positions were taken from the *RHESSI* and *Nobeyama* flare catalogs. The former may contain duplicates if satellite night or SAA passage occurred during a long flare, and the latter is less sensitive to small flares. Figure courtesy of P. J.A. Simões (private communication) 32
2.9 Time profiles of a quiet Sun transient event observed in Fe XI/X and Fe XII lines at 171 Å and 195 Å by EIT/SOHO. (Top) Temperature averaged over the area of the event (Top middle) Emission measure averaged over the area of the event. (Bottom middle) VLA radio fluxes at 6 and 3.6 cm at the location of the 6 cm peak. (Bottom) VLA radio fluxes at 6 and 3.6 cm at the location of the 3.6 cm peak. Figure from Benz (2017), adapted from Krucker & Benz (2000). 33
2.10 Magnetic field lines can become braided and tangled due to the random walk of their photospheric footpoints. Figure from Parker (1983). . . 36

2.11 Flare frequency distributions from multiple instruments with different energy ranges. (Top) Thermal events are shown both from active regions (microflares seen by*RHESSI* Hannah et al. 2008 and *Yohkoh*/SXT Shimizu 1995) and the quiet Sun (*TRACE*, Parnell & Jupp 2000; Aschwanden et al. 2000; *SOHO*/EIT, Benz & Krucker 2002). (Bottom) Non-thermal energy distributions shown are *RHESSI* microflares above the low-energy cutoff (E_C) (Hannah et al. 2008), *CGRO*/BATSE microflares >8 keV (Lin et al. 2001), and large flares >25 keV observed with *SMM*/HXRBS (Crosby et al. 1993). Note that the methodology and flare locations used to derive different distributions can vary greatly. Figure from Hannah et al. (2011). 39

2.12 Integrated intensity map of the Fe XIX spectral line (peak T $\approx$ 8.9 MK) from the EUNIS sounding rocket. Contour levels are 4 (yellow), 8, 16, and 32 erg cm^{-2} s^{-1} sr^{-1} (red) overlaid on a 94 Å image from *SDO*/AIA. Figure from Brosius et al. (2014). 41

3.1 (Top) Wolter Type-I focusing telescope design. This is the most commonly used design for X-ray focusing telescopes, both at SXR and HXR energies. (Middle) Wolter Type-II focusing telescope design. (Bottom) Wolter Type-III focusing telescope design. Images courtesy of NASA. 44

3.2 Schematic of a depth-graded multilayer coating with alternating layers of a heavy element (dark gray) and light material. The light material acts as a spacer so that the heavy layers can coherently reflect wavelengths that satisfy the Bragg condition (Eqn 3.1). Different wavelengths (energies) are reflected at different depths in the multilayer. Image from Gorenstein (2012). 45

3.3 Effective area curves for *NuSTAR*, *FOXSI-2*, and *RHESSI*. The *NuSTAR* area includes both telescopes (FPMA & FPMB). The *FOXSI-2* area includes all seven detectors, and the *RHESSI* area includes all nine detectors (front segments). 46

3.4 Ray-trace drawing of a Wolter-I telescope with properly focused double-bounce photons and one unfocused single-bounce photon (ghost ray) from a source outside the telescope FoV. Image adapted from Wikipedia (`https://en.wikipedia.org/wiki/File:Wolter-I_01.svg`). 47

3.5 (Left) Simulated off-axis point source images that show the spatial patterns created by single-bounce ghost rays in the *NuSTAR* FoV. The panels show the flux from a source located 6, 12, 20, and 30' off-axis (clockwise from the top left). (Right) Simulated *NuSTAR* count flux integrated over the instrument FoV for a large number of off-axis angles, shifted in both RA and DEC (left-right and top-bottom across the focal plane). The central peak with rates $>10^4$ counts sec^{-1} occurs when the source is still in the FoV and is imaged with double-bounced (properly focused) photons. A sharp drop-off occurs as soon as it leaves the FoV, with ghost-ray fluxes 1–2 orders of magnitude lower than the focused flux. Figure from Grefenstette et al. (2016). 56
3.6 The *FOXSI* sounding rocket payload. The seven optics modules focus X-rays onto seven solid-state detectors. The primary solar aspect system for sounding rocket payloads is the SPARCS (Solar Pointing Attitude Rocket Control System), which consists of two small sensors (LISS & MASS). An additional aspect and alignment system (SASS) was added for the *FOXSI-2* flight in order to determine the precise alignment between the SPARCS and the X-ray optics. Figure from Christe et al. (2016). 57
3.7 Hard X-ray images of a B2.7 flare during the first *FOXSI* flight on 2012 November 2. (Left) *RHESSI* image made using the CLEAN algorithm. Due to the indirect imaging there are significant sidelobes in the PSF which contribute noise throughout the reconstructed image FoV. (Right) *FOXSI* image with much better signal-to-noise ratio resulting from the use of focusing optics. Both images are shown for the *FOXSI* FoV, which is smaller than *RHESSI*'s. The same color scale is used in both panels. Figure from Krucker et al. (2013). 58
3.8 Differential emission measure of a nonflaring active region observed during the first *FOXSI* flight. The combination *Hinode*/XRT, *Hinode*/EIS, and *FOXSI* was used to calculate the DEM for $5.5 < \log(\mathrm{T}) < 7.5$. *FOXSI* is able to set strong constraints on plasma at $\mathrm{T} >$ 10 MK that aren't possible with the EUV and SXR data alone. Figure from Ishikawa et al. (2014); note that the x-axis units should be Temperature [log(K)]. 59
3.9 The *NuSTAR* HXR astrophysics satellite. The gray rectangular objects on the optics module are part of the laser metrology system. Image courtesy of NASA. 60
3.10 (Right) One of two *NuSTAR* optics on the assembly machine at Columbia University. (Left) Zoomed-in image of individual layers separated by graphite spacers. Image from the *NuSTAR* website (`http://www.nustar.caltech.edu/page/optics`.) 61

3.11 (Top) One of the *NuSTAR* detector plane modules comprising 4 pixellated CdZnTe detectors. (Bottom) Detector names and focal point for an on-axis source. Image from Harrison et al. (2013). 62

3.12 (Left) Active region *DEM* distribution from Warren et al. (2011). (Right) Simulated *NuSTAR* image of the Warren et al. (2011) active region in detector coordinates (mm). The gaps between the four detectors are clearly visible. 62

3.13 (Left) *NuSTAR* tiled images of the full Sun during its first solar pointing on 10 September 2014. An X-class flare had occurred near disk center before this observation began, resuling in high levels of X-ray flux. The center-right images are missing because the instrument FoV included the flaring region; this resulted in count rates so high that every *NuSTAR* event was rejected by on-board software. Image from Grefenstette et al. (2016). (Right) Integrated *NuSTAR* image from a slew away from the Sun during the same observation. The solar limb is marked by a red circle, and two bright active regions near disk center with green circles. The bright streak is a result of stray X-ray light (zero-bounce, not to be confused with single-bounce ghost rays) from the flaring active region hitting the detectors through an unbaffled part of the optics. 63

3.14 (Top) *NuSTAR* 2–4 and 4–6 keV HXR images of active regions near the limb on 2014 November 1, along with the differential hardness ratio. (Bottom) SXR and EUV images of the same regions from *GOES*/SXI, *SDO*/AIA 9 Å, and the Fe XVIII component of the 94 Å channel which isolates hotter plasma. White boxes indicate the regions used for subsequent spectral analysis. Figure from Hannah et al. (2016). . 64

3.15 *NuSTAR* spectra and isothermal fits for active regions near the limb on 2014 November 1. Fits are done separately for the two telescope modules (FPMA & FPMB), which can disagree due to slightly different exposure times and pointing alignment. Integrated images from both modules are shown at top left, along with the exposure time and livetime for each. Figure from Hannah et al. (2016). 65

4.1 (Left) *NuSTAR* image >2 keV in the FPMA telescope integrated over the 2014 November 1 north pole pointing. The detected emission is consistent with ghost rays produced by active regions outside the instrument FoV. (Right) Time profiles of the *NuSTAR* livetime (top panel), the *GOES* 1–8 Å flux (middle panel), and the *RHESSI* 3–6 and 6–12 keV fluxes (bottom panel). The slow rise detected by *RHESSI* at 22:18 UT is solar in origin, but outside *NuSTAR*'s field of view. . . . 69

4.2 (Left) Single frame of a *NuSTAR* FPMA image cube, with the solar limb overlaid in black. Spatial binning is $60'' \times 60''$ and temporal binning is 100 seconds. (Right) *NuSTAR* count spectra from both telescopes, integrated over the full north pole pointing and the full FoV. Error bars shown are the square root of the number of counts in each bin. Most or all of the photons in both panels are due to ghost rays from active regions outside the FoV. 72

4.3 (Left) The "just detectable" emission measure distributions for temperatures 2–12 MK, calculated for summed (FPMA+FPMB) north pole image cubes. These distributions include every macropixel from two image cubes: one with no time shift and one with a half-bin time shift. The "just detectable" limit corresponds to the intensity that gives a count excess above background at the 95% confidence level. (Right) The *NuSTAR* sensitivity for this observation with $t_{bin} = 100$s and $s_{bin} = 60'' \times 60''$. The black diamonds correspond to the peaks of the EM distributions in the left plot. The pink contour is the level at which *RHESSI* would detect 10 cts s^{-1} $\mathrm{detector}^{-1}$, approximately the instrument limit for imaging and spectroscopy. The soft X-ray transient brightenings observed by *Yohkoh*/SXT in Krucker et al. (1997) are shown as a red striped box; these events are below the sensitivity limit for this observation. *Yohkoh*/SXT upper limits on higher-temperature network flares are shown as brown arrows. 74

4.4 *NuSTAR* limits on 10–20 keV photon flux for this observation, calculated for the sum of FPMA & FPMB and three different temporal binnings (dwells). Each distribution includes every macropixel from two image cubes: one with no time shift and one with a half-bin time shift. The dashed line is the *RHESSI* detection limit at 10 keV. The dotted line is the average *RHESSI* microflare flux at 10 keV from Hannah et al. (2008). 76

4.5 Cumulative probability distributions of flux loss for several different values of flare duration divided by bin width. For values of $\tau/T < 0.5$ there is no flux loss in the best time bin, which we select for every trial. For $\tau/T = 1.5$ the probability curve is a delta function; the flux loss is exactly 50% for every start time and every bin. Results are shown for a top-hat profile (solid lines) and a triangular profile (dashed lines). . 78

5.1 Combined EUV and HXR image of five active regions observed by *NuSTAR* on 2014 November 1 with an effective exposure time of 3.11 s. *NuSTAR* 2–4 keV flux contours (5, 10, 25, 50, and 80%) from the FPMA telescope are overlaid in yellow on a *SDO*/AIA 94 Å image showing plasma >1 MK within each region. White boxes are the areas used for analysis. 87

5.2 *NuSTAR* spectrum from the FPMA module for one of the on-disk active regions observed on 2014 November 1. Isothermal fits and uncertainties are labelled on the plot. 89
5.3 *FOXSI-2* 4–15 keV HXR contours from Det. 6 overlaid on a *SDO*/AIA image of AR 12234. The AIA image is shown on a log scale with a colorbar that indicates the brightness in each pixel. The *FOXSI-2* contours have been chosen to show 30, 50, 70, and 90% of the maximum value, and the *FOXSI-2* exposure time is 38.5 s. 91
5.4 *FOXSI-2* count spectrum of AR 12234 from Det. 6. The best-fit isothermal T, EM, and 1-sigma uncertainties are written on the plot, and the fit range is marked by the dashed box. 92
5.5 Examples of high-frequency ($t_N = 500$ s) and low-frequency ($t_N = 5000$ s) EBTEL simulations of nanoflare heating in a single loop strand with $\mathrm{H}_0 = 0.05$ erg cm^{-3} s^{-1}, $\tau = 100$ s, and L = 2×10^9 cm. Low-frequency values are indicated with solid lines and high-frequency values with dashed lines. The high-frequency train was started 5000 s before the plotted times to erase the initial plasma conditions. (Top left) Volumetric heating rate as a function of time. (Top right) Average loop temperature as a function of time. (Bottom left) Time-averaged DEM distributions. The discontinuity in the high-frequency curve is the intersection of the coronal and TR DEM curves. (Bottom right) Simulated X-ray spectra integrated over the full DEM and a 60×60 arcsecond area. 93
5.6 (Left) Log chi-square intensity maps for the *FOXSI*-observed AR spectrum. Parameter pairs are H_0 vs. τ, H_0 vs. t_N, and t_N vs. τ with the third (unplotted) parameter optimized at every location. Brighter pixels indicate better fits. (Right) Heat maps showing the optimized values of the unplotted parameter for each intensity map in the same row. No constraints have been applied to the parameter space. Black lines in the left panels show 90% confidence levels for the case of 3 relevant parameters (Avni 1976). 96
5.7 (Left) As Figure 5.6, but the energy flux limit (Equation 5.2) and EUV/SXR limits from *SDO*/AIA and *Hinode*/XRT have been applied to the full parameter space. White (instead of black) lines in the left panels show 90% confidence levels for the case of 3 relevant parameters. 99
5.8 *FOXSI-2* spectrum of AR 12234 and three model fits at three different points in the re-optimized heating vs. duration parameter space with no limits (Figure 5.6, top left). The [H_0, τ] coordinates for models 1, 2, and 3 are [0.013, 79], [0.032, 126], and [0.079, 199] respectively. . . 100
5.9 Histograms of the chi-square (top) and fill factor (bottom) for the FOXSI AR and three different sets of limits: no limits, energy flux limits, and AIA+XRT limits. 101

5.10 (Left column) Log chi-square intensity maps for two *NuSTAR* AR spectra (D1 and L1) with same formatting as Figure 5.7. Blue lines in the left panels show 90% confidence levels for the case of 3 relevant parameters. 103
5.11 *NuSTAR* spectrum of AR D1 and three model fits at three different points in the re-optimized heating vs. duration parameter space with energy and EUV limits included (Figure 5.10, top left). The [H_0, τ] coordinates for models 1, 2, and 3 are [0.013, 79], [0.032, 126], and [0.079, 199] respectively. 104
5.12 Histograms of the chi-square (top) and fill factor (bottom) for the 5 *NuSTAR*-observed ARs and three different sets of limits: no limits, energy flux limits, and AIA limits. 106

6.1 (A) Simulated 22–27 keV HXR sources, including footpoints, a heated loop, and accelerated particles above the looptop. (B) Simulated *RHESSI* image of this configuration. The coronal sources are not visible due to limited dynamic range. (C) Simulated image from the proposed *FOXSI/FXI* satellite. Better sensitivity and dynamic range result in reduced sidelobes. (D) *FOXSI/FXI* image including the PSF deconvolution. All of the simulated sources are now clearly visible, showing the advantage of a dedicated solar HXR focusing instrument. Figure from Christe et al. (2017). 109
6.2 Examples of four different nanoflare trains. (Top) Nanoflares with identical heating amplitudes and $t_N = 1000$ s. (Middle) Nanoflares with identical heating amplitudes at $t_N = 5000$ s. (Bottom) Nanoflares with heating amplitudes from a power-law distribution with index -1.5. Events shown in blue have uniform delay times, and events shown in red have delay times that depend on the previous event energy (the average delay for both is 2000 s). Figure from Barnes et al. (2016b). . 110

List of Tables

2.1 Temperatures and energy losses for the corona and chromosphere, from Withbroe & Noyes (1977). Losses are tabulated separately for active regions and the quiet Sun. 35

5.1 Table of estimated loop lengths for the 5 *NuSTAR* and single *FOXSI-2* active regions. Numbers were obtained from manual selection of loop footpoints in *SDO*/AIA 171 Å images. 95
5.2 Range of physical parameters for simulated nanoflare trains. 97

Abstract

Hard X-ray Constraints on Faint Transient Events in the Solar Corona

by

Andrew J. Marsh

The solar corona is an extremely hot, dynamic region of the solar atmosphere. Hard X-ray (HXR) observations of the corona have revealed the temporal and spatial properties of solar flares that release energy between $\sim 10^{25}$ and $\sim 10^{33}$ ergs in active regions. Flare-like events with energies $<10^{26}$ ergs have been seen in the quiet Sun by extreme ultraviolet (EUV) and soft X-ray (SXR) instruments. However, non-flaring active regions and quiet coronal regions cannot be imaged by the *Reuven Ramaty High Energy Solar Spectroscopic Imager (RHESSI)*, the current solar-dedicated HXR observatory, due to a lack of sensitivity and dynamic range.

Even in the absence of heating and particle acceleration from solar flares, the corona maintains an average peak temperature 1–4 MK. This is several hundred times hotter than the photosphere; this discrepancy is known as the coronal heating problem. While the precise physical mechanisms that heat the corona are still unknown, observations at multiple wavelengths can constrain the properties of unresolved impulsive heating events ("nanoflares") in active regions and the quiet Sun. Until recently, only EUV and SXR data were available to investigate the nature of these events.

Focusing optics that directly image HXRs have recently been used to observe the Sun. The *Nuclear Spectroscopic Telescope Array (NuSTAR)* satellite is an astrophysics mission that was launched in 2013 and has pointed at the Sun on nine occasions to date. The *Focusing Optics X-ray Solar Imager (FOXSI)* sounding rocket was designed for solar observing and has flown two times (2012 and 2014). Both *NuSTAR* and *FOXSI* have observed non-flaring active regions and quiet Sun regions. In this text two analysis projects will be described in detail: *NuSTAR* observations of a quiet Sun region and the resulting limits on transient flare-like events, and constraints on the physical properties of nanoflares in active regions observed by *NuSTAR* and *FOXSI*.

NuSTAR first observed quiet Sun regions on 2014 November 1, although out-of-view active regions contributed a notable amount of background in the form of single-bounce (unfocused) X-rays. These data are used to search for quiet Sun transient brightenings on time scales of 30, 60, and 100 s and set upper limits on emission in two energy bands. 2.5–4 keV limits are expressed as the temperature T and emission measure EM of a thermal plasma, and 10–20 keV limits as model-independent photon fluxes. The limits in both bands are well below previous HXR microflare detections, though not low enough to detect events of equivalent T and EM as quiet Sun brightenings seen in previous soft X-ray observations. Future observations during solar minimum will increase the *NuSTAR* sensitivity by over two orders of magnitude due to higher instrument livetime and reduced background.

Active region spectra from the *FOXSI-2* sounding rocket and the *NuSTAR* satellite are used to constrain the physical properties of nanoflares simulated with the EBTEL field-line-averaged hydrodynamics code. X-ray spectra are modeled for various nanoflare heating amplitudes, durations, delay times, and filling factors. Additional constraints on the nanoflare parameter space are determined from energy flux limits and EUV/SXR data. For trains of homogeneous nanoflares, the *FOXSI*-observed region is well fit by nanoflares with large heating amplitudes > 0.02 erg cm^{-3} s^{-1} and a wide range of delay times and durations. The very best fits for this region occur when the delay time is $>$1700 s. The *NuSTAR*-observed regions are not fit as well by the homogeneous nanoflare model, and the good-fit regions of parameter space are fairly different. Three of the *NuSTAR*-observed regions are fit by smaller heating amplitudes $<$0.04 erg cm^{-3} s^{-1} and shorter delay times, and the other two regions are not well-fit by homogeneous nanoflares. Additional studies of active regions observed by HXR instruments are needed to determine if similar nanoflare distributions can provide good fits to a range of ARs.

Dedication

I would like to dedicate this thesis to my grandparents Eliana and Pedro Turina (also known as Mima and Nonno). They nurtured my curiosity from a young age and contributed significantly to my interest in science, both things I am extremely grateful for. I love you both very much!

Acknowledgments

I have led a very privileged life, mostly thanks to the hard work and love of my parents Rossana Turina Marsh and William Joseph Marsh. I had an incredible upbringing that I often took for granted, but I now realize how rare it was. Both they and my younger siblings Noël and Chris are really intelligent, kind, and goofy people and I love them dearly.

I consider myself very lucky to have worked with David Smith, as I believe he was the best advisor I could have asked for. He kindly and patiently taught me more about physics and statistics in my seven years of graduate school than I learned in all the years leading up to it. Even more importantly, he taught me what it means to be a careful and ethical scientist.

I think of Lindsay Glesener as a second advisor because she offered so much guidance and wisdom during my time as a grad student. She helped keep me excited about the work I was doing while also encouraging a rigorous research process. Her positive attitude and attention to detail are just two of the many ways she inspires me.

I want to thank the third member of my thesis committee, David Williams. David was the co-leader of an astrophysics journal club I participated in and learned a lot from. He also gave me extremely valuable feedback on my thesis; it is much the better for his input.

My time at UCSC was made particularly memorable by all the friends and colleagues I spent time with. I want to thank Trevor Keiber, of my physics grad cohort, for frequent motivation to go on epic backpacking adventures and to bring people together through music. Angelo Monteaux (the fantastic navigator) and Gregory Kaminsky (the soft-spoken Russian with a heart of gold) are similarly special friends and members of the same cohort (we had a good one)!

Justin Mosley has been an inspiration ever since we met a couple years ago. I thoroughly enjoyed our times playing music together and spreading joy to so many people in the Santa Cruz community. I have learned many valuable lessons from our friendship and hope to learn many more.

I met fellow physics PhD Richard Smith at the UCSC visit day and we became friends almost instantly. He is like a brother to me, and I am very happy to have shared the last seven years with him. His array of life skills and ability to make magic happen are truly impressive, and help me aspire to realize my own goals.

Daniel Weisberg has been a friend for eleven years, longer than anyone else I know. Through good times and bad he has been a unique, intelligent, and inspiring presence in my life. I hope that our paths continue to cross, one way or another, well into the future.

Alex Cuttitta has been a constant source of love and support over the last six years, and I feel truly blessed to share my life with her. She is a multi-talented and amazing cook, artist, photographer, and philosopher, as well as the most caring and compassionate person I have known. Many of my posters and talks would not have been nearly as good without her feedback! She was also incredibly patient, understanding, and motivating while I worked on my degree, and I am very grateful to her. The next chapter in our lives is destined to be an exciting one for both of us.

Special thanks is owed to our cat Jack Jack, who spent countless hours curled up next to me or on my lap while I worked on this dissertation. If I could add him as a co-author I would!

Chapter 1

Introduction

1.1 Origins

The Sun is a medium age, yellow dwarf star that is approximately 4.6 billion years old. It provides the vast majority of heat, light, and energy flux incident on the Earth. Because of its omnipresence and importance to life, the Sun has been revered as a sacred object and deity for thousands of years. At the same time, solar activity has been regularly recorded since at least 2500 BC (Henriksson 2009). More recently, the 19th century saw several important scientific advances including the first photograph of the Sun, the first observations of a solar flare and a coronal mass ejection, and the first measurement of solar spectroscopic lines. The 20th century saw heliophysics develop into a full-fledged scientific field, with satellite and ground-based observations made regularly in wavelengths including radio, visible, UV, X-rays, and gamma rays. Observations of the Sun in a variety of wavelengths have led to an improved understanding of many plasma physics processes. The construction of new instruments that are capable of directly imaging high-energy or hard X-rays (HXRs) has led to unique observations of the solar corona. This chapter serves as an introduction to aspects of the Sun's structure and properties that are necessary to understand the other chapters of this thesis.

1.2 Structure of the Sun

The Sun's radius is 6.957×10^5 km = $1R_\odot$, which corresponds to an angular diameter of ∼1920 arcseconds or 32 arcminutes (Mullan 2009). Over 73% of its composition is hydrogen, another 25% is helium, and heavier elements make up the remaining 1–2%. Overviews of the solar interior and atmosphere can be found in Mullan (2009), Phillips (1995), and Gibson (1977). Figure 1.1 shows the different interior and atmospheric components of the Sun, which will be discussed in the following sections.

1.2.1 The Interior

The basic physics of the solar interior are described in Mullan (2009), which I follow here. The heat and light emitted by the Sun are a product of nuclear reactions happening in its core, where hydrogen atoms are fused into helium under immense temperature (15–16 million K) and pressure (250 billion atmospheres). 99% of the Sun's energy is produced within $0.25R_\odot$, and from there it slowly propagates outward through the radiative and convective zones. The radiative zone is a region of the solar interior $\sim$0.2–$0.7R_\odot$ in which thermal radiation is the dominant mechanism of energy transfer. At the outer edge of the radiative zone large thermal currents evolve to carry heat towards the surface. This convective zone extends from $\sim0.7R_\odot$ to $1.0R_\odot$. Once material reaches the surface (radius at which the plasma becomes optically thin) it loses most of its heat and sinks down to the bottom of the convection zone, where it is heated once more and repeats the same process. The tops of these convection cells are visible as on the Sun as "granules"; the dense ensemble of granular cells is referred to as "granulation". A typical granule has a diameter of about 1500 km and lasts 10–20 minutes before dissipating (Bahng & Schwarzschild 1961).

The convective circulation of plasma produces the Sun's global magnetic field through a dynamo process that isn't fully understood; for a review see Tobias (2002). A dynamo converts kinetic energy into electromagnetic energy, and can amplify small-scale fields in an electrically conducting fluid. Convection combined with the Sun's differential rotation (sidereal periods are ∼25 days at the equator and >34 days near

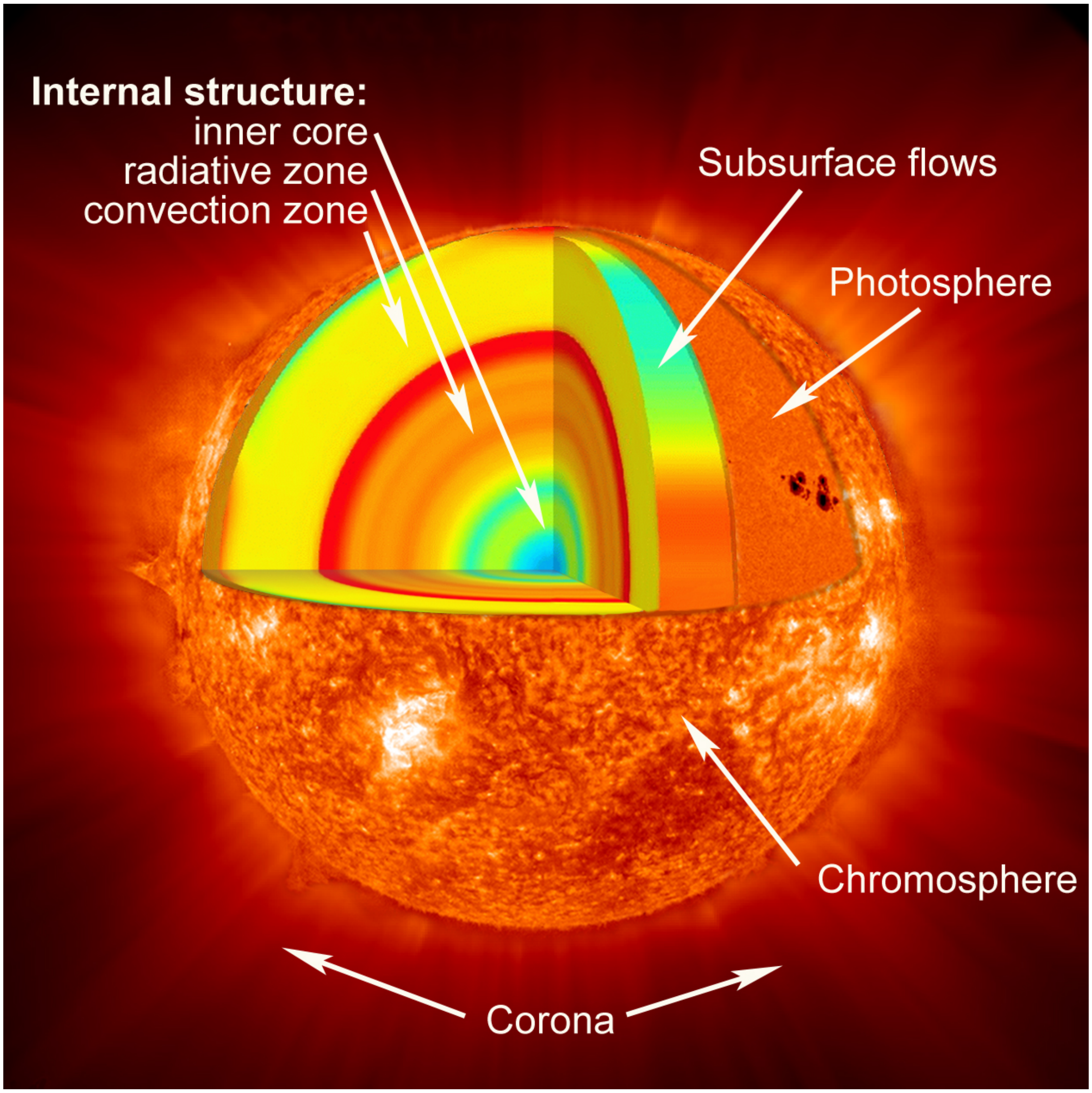

Figure 1.1: The layers of the Sun from the center to the outer atmosphere. The photosphere, chromosphere, and corona appear as they do to imaging instruments designed to see each specific layer. Images cannot be made of the solar interior. Image courtesy of NASA.

the poles, e.g. Beck 2000) builds up large-scale magnetic fields in plasma below the photosphere. Regions of high magnetic field form cylindrical structures known as flux tubes that are buoyant relative to the surrounding plasma. These flux tubes can rise to the solar surface (photosphere) and emerge as bipolar features (see Section 1.2.3).

1.2.2 Lower Atmosphere

The physical properties of the photosphere, chromosphere, and corona are described in detail by Mullan (2009) and Aschwanden (2004). Here I discuss the most salient features.

Photosphere

The visible surface of the Sun has a temperature that ranges from 4500 to 6000 K with an effective (blackbody) temperature of approximately 5700 K. Notable features of the photosphere include the granulation mentioned above and dark regions known as sunspots. Sunspots are darker than the rest of the photosphere because their strong magnetic fields suppress convection of hot material. Figure 1.2 shows a full-Sun image of the photosphere along with a close-up image of sunspot and granulation. The unceasing motion of photospheric plasma in and on the edges of granules is the primary source of magnetic energy release in the chromosphere and corona (see Sections 2.1.2 and 2.4).

Chromosphere

The "sphere of color" is a thin (1000–2000 km) layer of the Sun's atmosphere that lies between the photosphere and the corona. It is normally invisible at optical wavelengths, but can be seen at the start and end of eclipses as a reddish ring around the Sun. The density in the chromosphere (10^{-9} kg m^{-3}) is about a thousand times lower than at the Sun's surface. The temperature of the chromosphere drops from 6000 K at its inner edge to a minimum of $\sim$3800 K, before increasing to $\geq$35,000 K at the outer edge where it meets the corona. The boundary between the chromosphere and the corona is known as the "transition region". Over the mere $\sim$100 km thickness

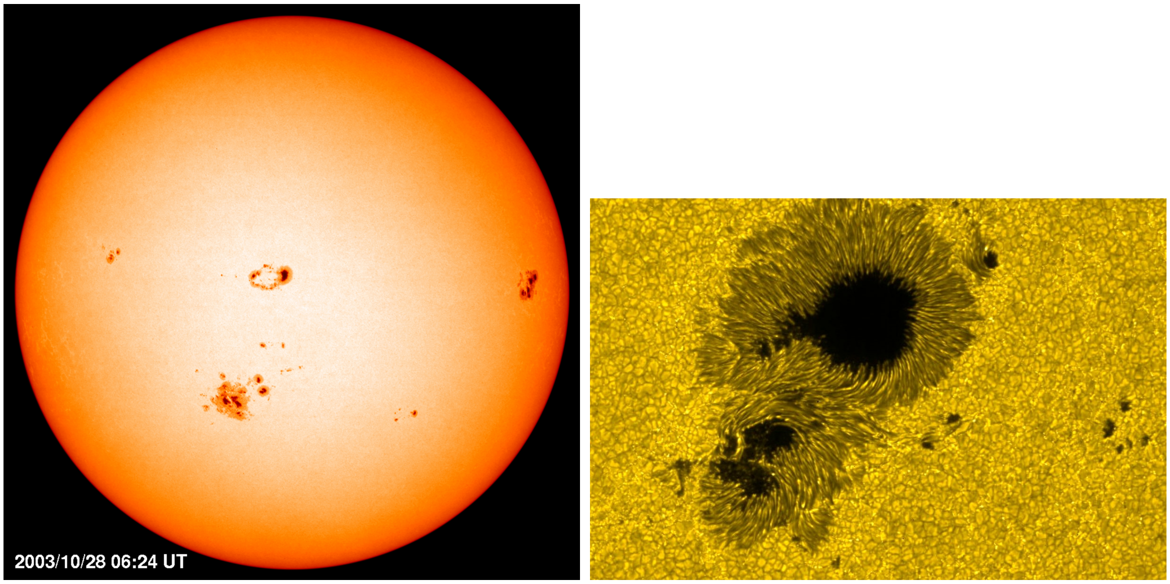

Figure 1.2: (Left) The solar photosphere imaged in visible light by the *SOHO* satellite. Several sunspot groups are visible near the equator, with less visible structure towards the poles. (Right) High-resolution image of a sunspot and the surrounding granulation, taken by the Solar Optical Telescope onboard the *Hinode* mission. The dimensions of this image are 218×109 arcseconds^2, which is approximately 166,000×83,000 kilometers^2. Images courtesy of NASA.

of this layer, the temperature and density rise and fall respectively by about two orders of magnitude (Figure 1.3). In addition, the dominant physical force switches from gas pressure below to magnetic pressure above.

1.2.3 Outer Atmosphere (Corona)

The corona is the outermost part of the Sun's atmosphere. It is extremely faint in visible light because its density is $\sim 10^{-12}$ times that of the photosphere. However, it can be seen by eye during total eclipses as wispy tendrils around the obscured solar disk. The most striking feature of the corona is its temperature, which is several million K on average. This makes it 150–450 times hotter than the photosphere, an unsolved mystery known as the "coronal heating problem" (see Section 2.4).

In the corona the ratio of plasma pressure to magnetic pressure, β, is much smaller than unity. This means that magnetic forces dominate the behavior of particles.

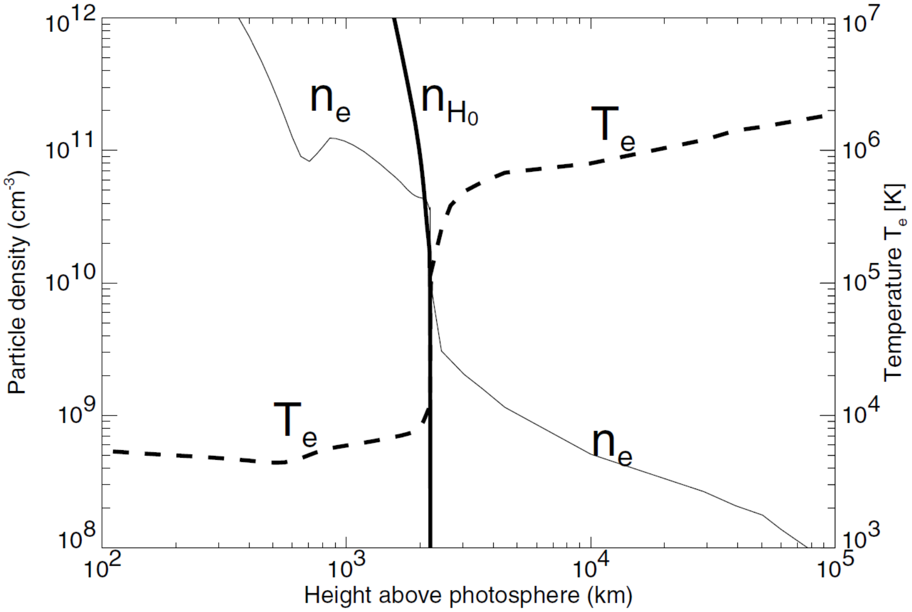

Figure 1.3: Temperature and density models of the chromosphere (Fontenla et al. 1990; FAL-C model) and lower corona (Gabriel 1976). At the transition region the temperature suddenly rises and the density suddenly drops by orders of magnitude. This is also the boundary between partial and full plasma ionization, indicated by the much steeper drop in the hydrogen density than the electron density. Figure from Aschwanden (2004).

Because of this, plasma emission typically comes from loop-like structures that follow magnetic field lines rooted in the chromosphere or photosphere. Cross-field transport or diffusion is severely limited, and electrons and ions propagate along field lines. Figure 1.4 shows an example of these ubiquitous coronal loop features.

Active and Quiet Regions

Active regions (ARs) are bright coronal features of high magnetic field strength and complexity, visible across a wide range of wavelengths. Large ARs correspond to sunspots in the photosphere. The physical properties mentioned below are compiled in the Encyclopedia of Astronomy and Astrophysics (Maran 2001). ARs generally emerge as bipolar regions within ±60 degrees latitude, though large regions typically emerge within ±30 degrees. Magnetic field strengths in ARs range from ∼1000 to

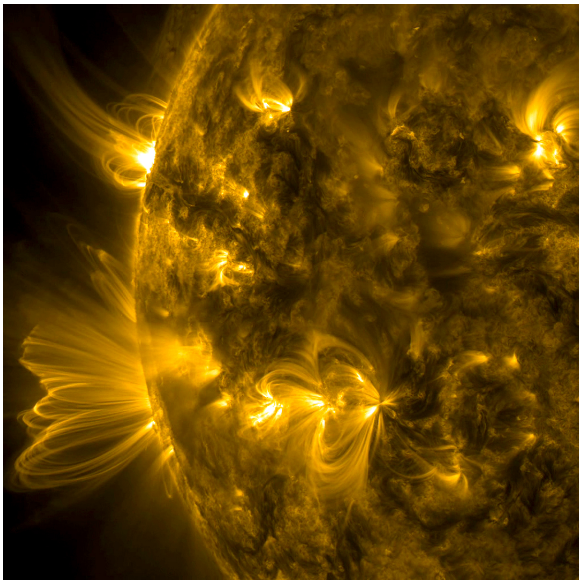

Figure 1.4: Loop structures in the corona imaged by the *SDO*/AIA instrument at 171 Å. The plasma seen in this image ranges in temperature from ∼0.3 to 2 MK. Image courtesy of NASA.

5000 Gauss, compared to the Sun's global average field strength of ∼1 Gauss (values measured at the photosphere). In addition, active regions exhibit higher average coronal temperatures (peak T 2–6 MK) and higher densities ($\sim 10^9$ particles cm^{-3}) than other parts of the Sun.

Quiet Sun regions of the corona have peak temperatures of ∼1 to 2 MK and densities between 10^7 and 10^8 particles cm^{-3} (Aschwanden 2004). The weak magnetic field patterns in the quiet Sun are known as the network field; background fields are typically 0.1–0.5 G and resolved elements have strengths of 10–50 G (at the photosphere). Figure 1.5 shows the contrast between the magnetic field strength in active regions and the quiet Sun. With more sensitive observations it has become clear that the "quiet Sun" is actually filled with dynamic processes, though on smaller scales and at lower energies than active regions.

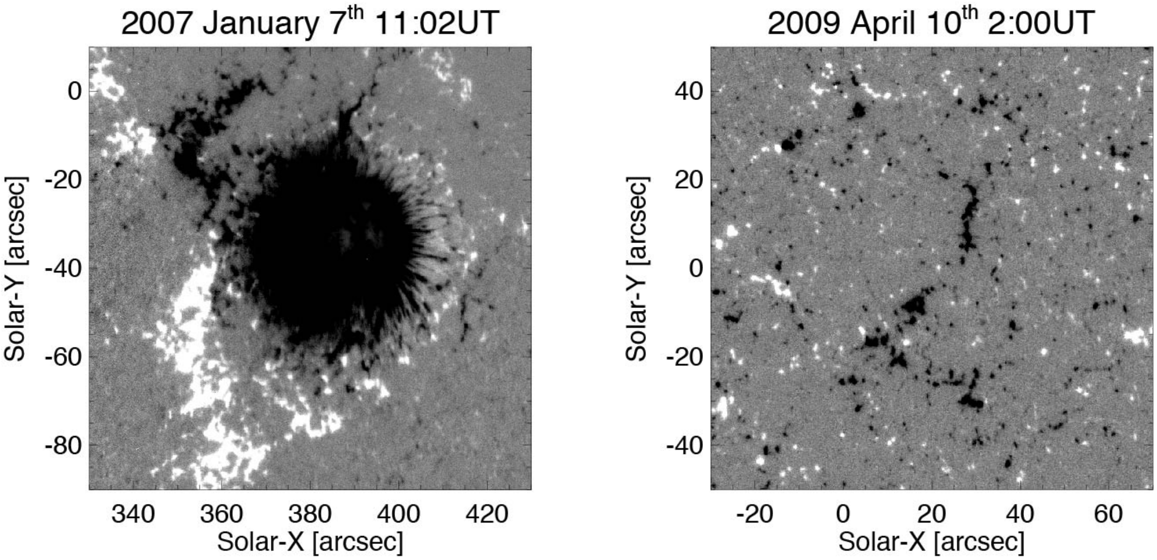

Figure 1.5: Line-of-sight magnetic field maps (magnetograms) for an active region (left) and a quiet Sun region (right), measured with the *Hinode* satellite. Black and white indicate negative and positive magnetic polarities (into and out of the page, respectively). The magnetic field strength is measured at the photosphere in this image. Figure from Iida (2012)

.

1.3 Solar Cycle

The Sun exhibits a regular activity cycle that goes from a maximum to a minimum every ∼11 years (half-cycle). The global magnetic field polarity reverses and returns to its original configuration after ∼ 22 years (full cycle). In addition, the total unsigned magnetic flux is greatest during solar maximum and smallest during solar minimum. This cycle was first discovered by Schwabe (1844) due to the associated increase and decrease in the number of sunspots. Because many solar radiation mechanisms are a result of magnetic energy dissipation (see Chapter 2) the radiation output in many wavelengths is correspondingly modulated by the solar cycle. Figure 1.6 shows X-ray maps and magnetograms over a ten-year interval, nearly an entire solar cycle. It is clear from this image that the Sun emits significantly more X-rays at the peak of the cycle; this is true of many observed wavelengths.

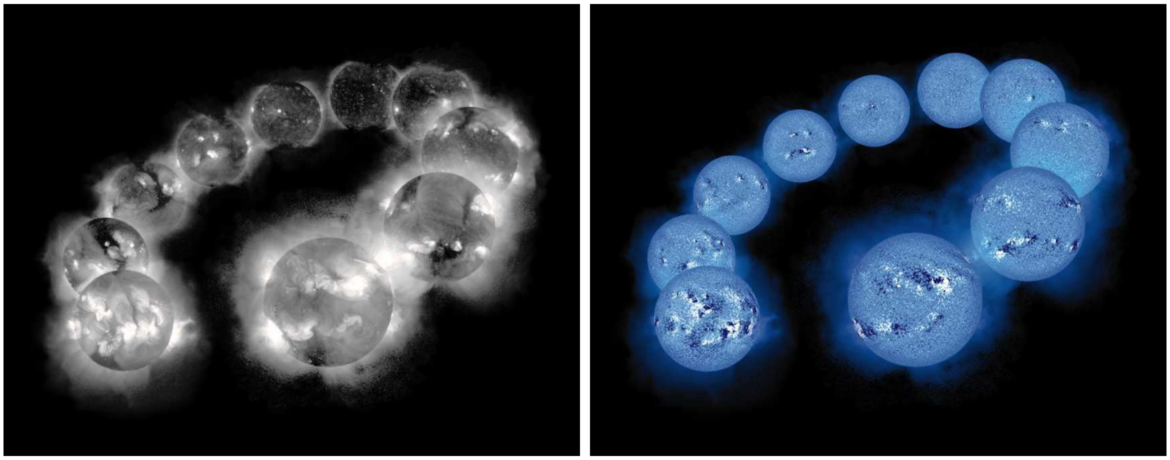

Figure 1.6: (Left) Full-Sun images from the *Yohkoh*/SXT X-ray telescope over the course of 10 years (1992 January 8 to 1999 July 25). The X-ray flux is significantly higher at solar maximum. (Right) Full-Sun magnetograms recorded with the Vacuum Telescope at Kitt Peak National Observatory over the same period as the X-ray images. White and black represent positive and negative magnetic field polarity (parallel to the line-of-sight). Blue indicates regions with zero field. Figures from Aschwanden (2004).

Solar Flares

Solar flares are localized brightenings in the Sun's atmosphere that can release up to 10^{33} ergs of energy in minutes across a wide range of wavelengths (Benz 2017). Solar flares occur predominantly in active regions, although flare-like brightenings have been seen in the quiet Sun (see Sections 2.3.3 and 2.3.4). The biggest flares often coincide with large ejections of hot plasma into interplanetary space; these "coronal mass ejections" (CMEs) can have damaging effects on electronic devices in orbit and on the surface of Earth. Smaller flares do not generally have associated CMEs.

The first observed solar flare was seen simultaneously by Richard C. Carrington and Richard Hodgson in 1859 (Carrington 1859; Hodgson 1859). This event was a "white-light" flare, or one that brightened enough in visible wavelengths to be noticeable to observers. Flares are much easier to detect with other wavelengths, particularly ultraviolet and X-rays. The *Reuven Ramaty High Energy Solar Spectroscopic Imager (RHESSI)* has made significant contributions to our understanding of flares through HXR imaging spectroscopy of over 114,000 X-ray events[1]. I discuss the detailed physics of flares in Chapter 2.

1.4 Summary

This dissertation presents outstanding problems in high-energy solar physics and describes HXR observations that can contribute to their solution. Chapter 2 covers the physics of flares, coronal emission, and the coronal heating problem and observations of these phenomena. Chapter 3 describes the novel observing capabilities of HXR instruments with focusing optics, particularly the *Nuclear Spectroscopic Telescope Array* (*NuSTAR*) satellite and *Focusing Optics X-ray Solar Imager* (*FOXSI*) sounding rocket. Focusing HXRs leads to much higher sensitivity and dynamic range compared to non-focusing instruments. The increased sensitivity of *NuSTAR* and *FOXSI* enabled studies of the quiet Sun and active regions that could not be performed with *RHESSI*, the current solar-dedicated HXR telescope. Chapter 4 is an analysis of a quiet Sun region observed with *NuSTAR* in which I led a search for transient events similar to flares. Chapter 5 is an analysis of multiple active regions observed by *NuSTAR* and one active region observed by *FOXSI* in which I used statistical tests to constrain the physical properties of so-called "nanoflares": tiny transient energy releases that may be the dominant source of hot coronal plasma. Chapter 6 describes future analysis that can build on the work described here, and outlines my conclusions.

---

[1] `https://hesperia.gsfc.nasa.gov/rhessi2/`

Chapter 2

Flares, Transient Events and Coronal Heating

Abstract

Solar flares have been frequently observed in active regions with hard X-ray (HXR) instruments. However, flare-like events also occur in the quiet Sun and have not been seen in HXRs. This chapter explores the physical mechanisms that are associated with solar flares and flare-like brightenings. These include magnetic reconnection, particle acceleration, and heating. In addition, it gives an overview of observational methods used to characterize flare processes in extreme ultraviolet (EUV), soft X-ray (SXR), and HXR wavelengths. EUV, SXR, and HXR observations can constrain solutions to the coronal heating problem, which is discussed in detail. New HXR instruments with focusing optics can put strong limits on coronal heating mechanisms.

2.1 Flare Physics

Solar flares are associated with rapid energy release in the corona and are believed to be driven by magnetic energy. They heat coronal and chromospheric plasma and accelerate particles into non-thermal distributions. Increased radiative output associated with these events occurs in almost every wavelength, from radio to X-rays to gamma-rays (observed only in the largest flares).

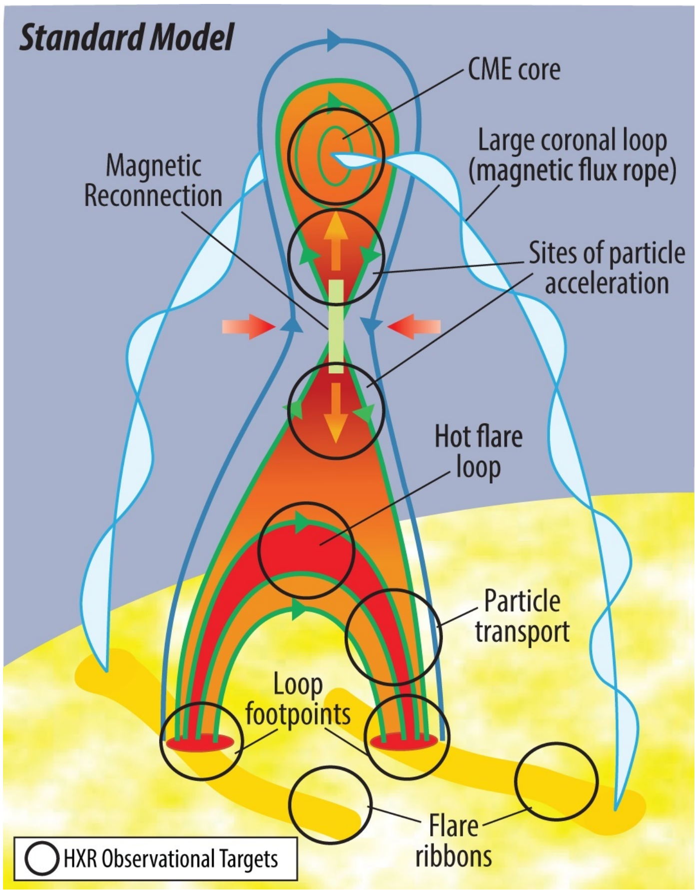

Figure 2.1: The standard model of solar flares. Magnetic reconnection in the corona is caused by a rising flux rope that subsequently erupts as a CME. This causes the acceleration of particles, many of which stream down magnetic loops to their footpoints. Plasma is heated at the footpoints and subsequently rises into the corona. Typical locations of HXR sources are indicated by black circles; for a detailed discussion see Section 2.3.3. Figure from Christe et al. (2017).

2.1.1 Standard Flare Model

Solar flares are driven by the restructuring of magnetic fields (Section 2.1.2). Neither thermal energy nor nuclear energy, the only other remotely viable sources, can provide the required energy in the corona. A standard model for flares was first laid out in a series of papers in the 1960s and 1970s, and is sometimes referred to as the CSHKP model after the authors' initials (Carmichael 1964; Sturrock 1966; Hirayama 1974; Kopp & Pneuman 1976). Of course not all flares can be explained by a single model, but it is a useful unifying picture that is consistent with a large number of observations and has a fairly strong theoretical basis.

Figure 2.1 shows the basic features of this model. A solar flare begins with magnetic reconnection (Section 2.1.2) in the corona; this process releases energy stored in the magnetic fields. Particles (electrons and ions) are accelerated through one or more physical mechanisms that are not well understood (Section 2.1.3). They subsequently propagate down magnetic field lines towards the chromosphere where they collide with ambient particles and lose their energy. This energy deposition heats the plasma at the loop footpoints and causes it to expand and ablate into the corona, a process known as chromospheric evaporation. These processes can happen with or without the erupting flux rope (a volumetric plasma structure with magnetic field lines twisted around a central axis, e.g. Filippov et al. 2015).

2.1.2 Magnetic Reconnection

Magnetic reconnection is a fundamental physical process that occurs in astrophysical and earth-bound systems such as stellar coronae, planetary magnetospheres, accretion disks, and tokomaks. It is broadly defined as a topological change in the magnetic connectivity of field lines in time. Since ideal magnetohydrodynamics (MHD) requires that magnetic flux remains frozen, reconnection is a non-ideal MHD process. It can result in a transfer of magnetic energy into other forms including heating and particle acceleration. Here I discuss steady-state 2D theories of reconnection; 3D geometries (see Janvier 2017 for a review) and time-dependence add additional levels of complexity .

Sweet-Parker Reconnection

Sweet (1958) and Parker (1957) developed the first quantitative model of reconnection. They assumed reconnection in a thin layer of electric current (current sheet)

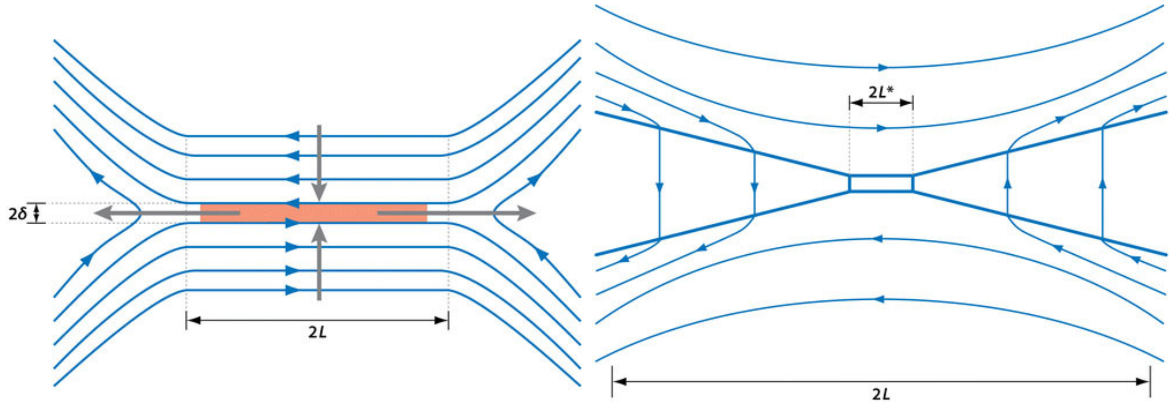

Figure 2.2: (Left) Sweet-Parker reconnection geometry with a long, narrow diffusion region. (Right) Petschek reconnection geometry with a symmetrical diffusion region.(Zweibel & Yamada 2009).

with a length L much longer than its width δ (Figure 2.2). Oppositely-directed horizontal magnetic fields are present above and below the current sheet. Magnetic energy is converted to thermal and kinetic energy within the current sheet region. Using conservation of energy, I can show that the maximum outflow speed from this region is the Alfvén velocity v_a:

$$\frac{B^2}{2\mu_0} = \frac{1}{2}\rho v_{\text{out}}^2 \tag{2.1}$$

$$v_{\text{out}} = \frac{B}{\sqrt{\mu_0 \rho}} \equiv v_A \tag{2.2}$$

Plasma flows into the current sheet with a speed v_{in} given by

$$v_{\text{in}} = v_a S^{-1/2} \tag{2.3}$$

where $S = \mu_o L v_a/\eta$ is the Lundquist number and η is the magnetic diffusivity. S is equivalent to the magnetic Reynolds number with a system scale velocity equal to the Alfvén velocity. High values of S correspond to highly conducting plasmas and low values of S to resistive plasmas.

The unitless reconnection rate for the Sweet-Parker model is given by the ratio of the inflow speed to the outflow speed:

$$M_{SP} = v_{\text{in}}/v_a = 1/\sqrt{(}S) \tag{2.4}$$

In the highly-conductive corona $S \approx 10^8$–10^{12} and this rate is very small (10^{-4}–10^{-6}, equivalent to solar flare durations of years). Sweet-Parker reconnection cannot explain the rapid energy release in solar flares, which happens on time scales of seconds to minutes.

Petschek Reconnection

Petschek (1964) proposed a faster reconnection model with a much shorter diffusion region (Figure 2.2). In this model slow-mode shocks separate the inflow and outflow regions. Those shocks are where most of the energy conversion (from magnetic to kinetic and thermal) occurs. In Petschek's model the reconnection rate is given by

$$M_P = \frac{\pi}{8\ln(S)} \tag{2.5}$$

For the corona this rate is 10^{-1}–10^{-2}, or hundreds of seconds: this is only an order of magnitude slower than observed (Aschwanden 2004). However, Petschek reconnection requires a local, strongly-enhanced resistivity in the diffusion region to be seen in MHD simulations. If this is not included then models tend to show a Sweet-Parker geometry.

Hall Reconnection

Both Sweet-Parker and Petschek reconnection are collisional processes, as particles decouple from magnetic field lines due to collisions in the diffusion region. Simulations have shown that neither is fast enough to account for magnetic reconnection under coronal conditions. However, recent work has shown that collisionless reconnection can occur on extremely short time scales.

The generalized Ohm's law is given by

$$\vec{E} + \vec{v} \times \vec{B} = \eta\,\vec{J} + \frac{1}{e\,n_e}\left(\vec{J} \times \vec{B} - \vec{\nabla} P_e\right) \tag{2.6}$$

where $\vec{E}$ is the electric field, $\vec{B}$ is the magnetic field, η is the resistivity, and P_e is is the electron pressure. In the ideal MHD approximation all three of the terms on the right are neglected; Sweet-Parker and Petschek reconnection are ideal processes (except in the diffusion region where the resistive term becomes important). The Hall ($\vec{J} \times \vec{B}$) term can lead to important physical effects on spatial scales smaller than an ion gyroradius. At these scales ions will decouple from magnetic field lines (and from the electrons that remain coupled). The resulting Hall electric and magnetic fields widen the outflow region for electrons and ions (Drake et al. 2008), allowing reconnection to proceed much faster: about 6–8 orders of magnitude faster than Sweet-Parker reconnection, without the Petschek models requirement of anomalous resistivity (Birn et al. 2001). Collisionless reconnection without the Hall term has also been shown to yield fast reconnection rates, so the primary physical driving force of fast reconnection rates is still debated (Cassak & Shay 2012). However, it is clear that Sweet-Parker type (collisional) reconnection is not fast enough for solar flares, and may not even occur under coronal conditions (Cassak & Shay 2012).

High resolution observations by the *SDO* satellite have been used in coordination with other instruments to clearly image reconnection sites in the corona (Su et al. 2013; Sun et al. 2015; Reeves et al. 2015). From these results it has become clear that an important component of understanding coronal magnetic reconnection is 3D effects, which in simulations can lead to significantly altered reconnection rates versus 2D (Zharkova et al. 2011). Regardless of the exact physical mechanisms at work, it is clear that reconnection plays a significant role in coronal energy release and is the most efficient way to extract magnetic energy (Priest & Forbes 2000).

2.1.3 Particle Acceleration

Flare acceleration mechanisms can raise electrons to MeV energies and ions to GeV energies. Observations have shown that these mechanisms must accelerate particles on time scales of 0.1–1.0 s for durations of minutes or even substantial fractions of an hour, efficiently convert ∼50% of magnetic energy into kinetic energy (Emslie et al. 2012; Aschwanden et al. 2017), efficiently accelerate a large fraction (∼50%) of particles to non-thermal energies, and produce power-law particle distributions (Raymond et al. 2012). For a theoretical review of particle acceleration in flares, see Zharkova et al. (2011).

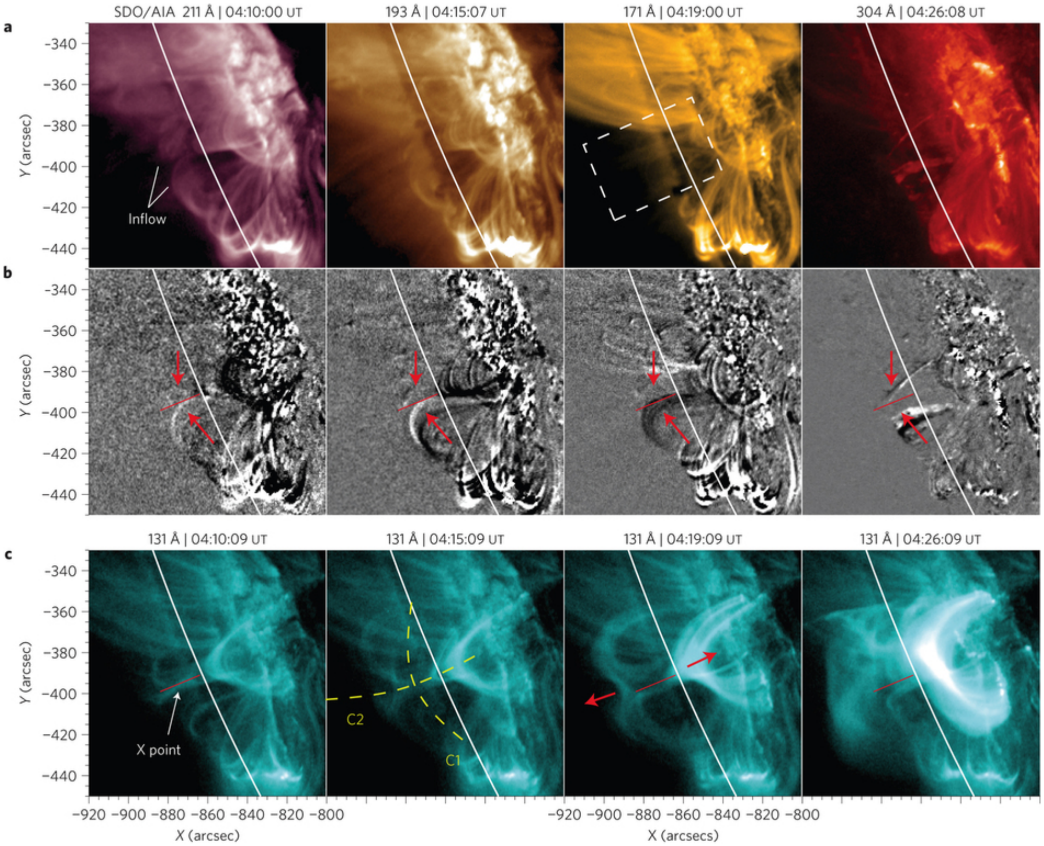

Figure 2.3: Magnetic reconnection at different times during a solar flare on 2011 August 17. The white line in each frame marks the edge of the photosphere, and image coordinates are in solar arcseconds. (Top) *SDO*/AIA images at 211, 193, 171 and 304 Å show inflowing loops with temperatures between ∼0.05 and 2 MK (Middle) Same images as top row, with images from a minute earlier subtracted. White and black indicate increases and decreases in intensity, respectively. The red line marks the initial location where inflowing loops seem to merge and disappear; red arrows show the inflow directions. (Bottom) AIA images at 131 Å show plasma heated to ∼10 MK at the center of the inflowing loops. Co-temporal X-ray images from *RHESSI* (not shown) provide additional evidence for plasma heating following reconnection. The observed (unitless) reconnection rates $v_{\mathrm{in}}/v_{\mathrm{out}}$ for this event were 0.05–0.5, with inflow / outflow velocities ranging from ∼few to ∼100 km s^{-1}. Figure from Su et al. (2013).

At the most basic level, charged particles are accelerated by electric fields. Open questions for coronal particle acceleration relate to the large-scale structure and temporal evolution of these fields. Three physical mechanisms often considered are 1) electric fields parallel to the magnetic field, 2) shocks (Fermi acceleration), and 3) stochastic acceleration (resonant acceleration by waves). While one of these processes may dominate, it is likely that some or all of them operate during flares to varying degrees.

DC electric fields can accelerate electrons through a “runaway” process if the electric force is strong enough to overcome the ion drag force (Holman 1985). Small-scale fields are likely to be generated during magnetic reconnection in a bursty fashion (e.g. in magnetic islands). Strong fields at these scales may play a part in flare acceleration, but weaker fields at larger spatial scales are problematic because of the immense currents they imply and because current sheets would become unstable at the required lengths (Aschwanden 2004; Zharkova et al. 2011).

Shock acceleration occurs at discontinuous boundaries (i.e. shock fronts) which can transfer energy and momentum to traversing particles. Shocks are well known to accelerate particles at CME fronts, events that produces bursts of radio waves (Gosling 1993; Reames 1999). In addition, several scientists have developed models of shock acceleration near reconnection outflows in solar flares (e.g. Somov & Kosugi 1997; Tsuneta & Naito 1998). However, their application to solar flares is questionable for several reasons: shocks generally dont appear in 3D MHD simulations, require an injection of “seed” particles above thermal energies, and require a scattering agent (such as turbulence or magnetic mirrors) for efficient energization (Zharkova et al. 2011).

Stochastic acceleration (e.g. Petrosian & Liu 2004) occurs when waves at frequencies resonant with particle gyrofrequencies provide a net gain of energy to those particles. There are many wave types in the corona that could provide the necessary energy; however, wave populations and a certain level of turbulence are ill-constrained by observations and must be assumed in models. This mechanism is particularly compelling in cases where bulk acceleration of most or all the particles in a coronal region has occurred (e.g. Krucker et al. 2010). As opposed to DC electric field models, stochastic acceleration avoids the generation of extremely strong currents that may not be physically possible.

The electron number problem is a particularly strong constraint on flare acceleration mechanisms (Raymond et al. 2012). A large flare produces $\sim 10^{39}$ energetic electrons, which corresponds to the entire electron content of a substantial volume of the corona. Thus the acceleration mechanism must be extremely efficient, energizing most of the electrons that enter the reconnection region (assuming a coronal location). The propagation of this many electrons to loop footpoints also implies an enormous electric current, which necessitates a return current to cancel the large inductive electric and magnetic fields. One additional acceleration mechanism that has been invoked to avoid the number and return current problems is the Alfvén wave model of Fletcher & Hudson (2008). This model posits bulk energy transport via wave pulses that induce particle acceleration in the chromosphere, as opposed to the standard model of particle beams coming down from the corona. However it still invokes magnetic reconnection as the primary mechanism of energy release, which leaves open the possibility of coronal acceleration through the means listed above.

X-ray and multi-wavelength observations can help validate or disprove the various acceleration mechanisms discussed. Simultaneous imaging and spectroscopy of particle acceleration sites and energy deposition sites can set stringent constraints on particle numbers, density, and energy. The current generation of instruments such as *NuSTAR* and *FOXSI* (Chapter 3) have produced new data to help clarify our picture of how particles are energized in solar flares. Continued regular, direct imaging of accelerated particles in the corona with increased instrumental sensitivity and dynamic range is sure to yield new discoveries.

2.2 Emission from the Solar Corona

Coronal plasma can be seen in wavelengths ranging from ultraviolet to gamma-rays (Figure 2.4). Here I focus on emission from $\gtrsim 1$ MK plasma that is visible to extreme ultraviolet (EUV), soft X-ray (SXR) and hard X-ray (HXR) instruments. This temperature range is well suited for imaging and spectroscopy of the quiet corona, active

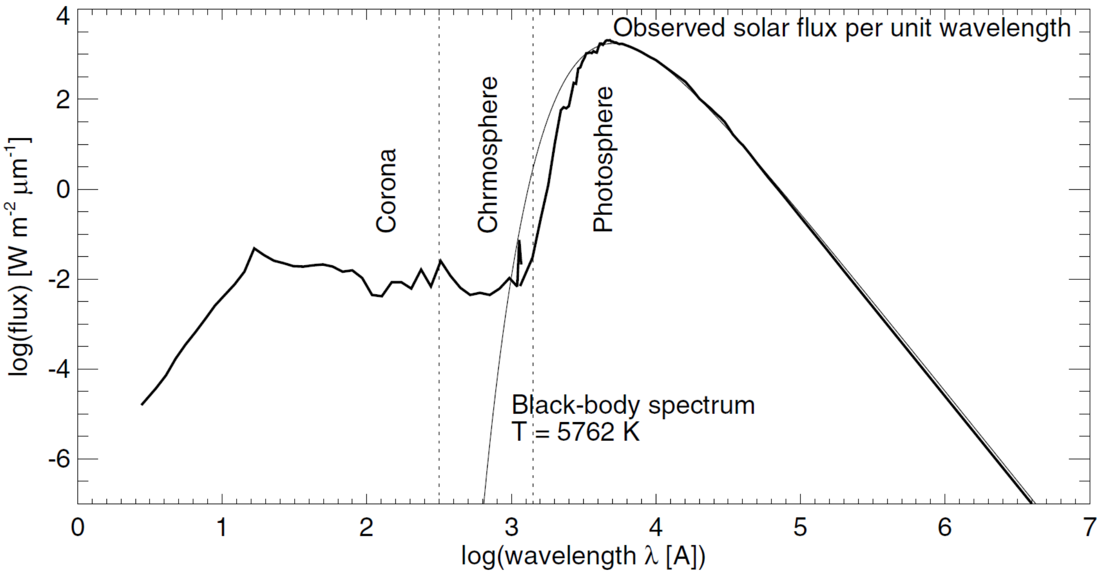

Figure 2.4: The observed solar flux spectrum per unit wavelength (thick line). The thin line is a blackbody spectrum of temperature T = 5762 K. Figure from Aschwanden (2004).

regions, and flares.

As discussed in Section 1.2, the corona is a fully ionized plasma in which electrons and ions can move separately. The most common interaction between these particle species is a free electron scattering in the electric field of an ion; a photon can be emitted as a result of this *bremsstrahlung* (braking radiation, also referred to as *free-free* emission). The emitted photon's energy is equal to the kinetic energy lost by the electron in this scattering event. The spectrum resulting from an ensemble of such scattering processes is derived below (Section 2.2.1). At longer wavelengths (EUV, SXR) there are important spectral components from emission lines of highly ionized metals (e.g. Mg, Si, Ca, Fe).

2.2.1 Thermal Bremsstrahlung

HXR observations can provide a direct measure of particle acceleration and heating in solar eruptive events for several important reasons. First, the corona is optically thin and the photons can propagate to Earth unimpeded. Second, the relevant emission mechanisms are not affected by ionization equilibrium time scales that can affect the interpretation of spectral line temperatures at EUV/SXR wavelengths (e.g. Bradshaw & Klimchuk 2011; see additional discussion in Section 2.4). Third, the cross-sections for bremsstrahlung (the primary radiation source at HXR energies) are well understood. What follows is a brief derivation of the photon spectrum produced by bremsstrahlung in a single-temperature (isothermal) plasma.

The differential cross-section $\frac{d\sigma}{d\Omega}$ of an electron scattering off an ion was first derived by Rutherford (1911):

$$\frac{d\sigma}{d\Omega} = \frac{Z}{4}\left(\frac{e^2}{m_e v^2}\right)^2 \frac{1}{\sin^4(\theta/2)} \tag{2.7}$$

Here Z is the proton number, v is the electron velocity, m_e is the electron mass, e is the electron charge, and θ is the scattering angle. Ω is the solid angle into which the electron is scattered and is related to the deflection angle θ by $d\Omega = 2\pi \sin\theta \, d\theta$. The total cross-section for bremsstrahlung can be calculated using energy and momentum conservation; in the non-relativistic limit this reduces to the widely used Bethe-Heitler form (Koch & Motz 1959):

$$\sigma(E, \epsilon) \approx \frac{8\alpha r_e^2 m_e c^2}{3} \frac{1}{\epsilon E} \ln\left[\sqrt{\frac{E}{\epsilon}} + \sqrt{\frac{E}{\epsilon} - 1}\right] \tag{2.8}$$

Here E is the electron energy, ϵ is the photon energy, α is the fine structure constant, and $r_e = \frac{e^2}{m_e c^2}$ is the classical electron radius. The total emitted bremsstrahlung power from a thermal plasma is given by the convolution of the total power emitted by a given electron with the velocity distribution of the electrons in that plasma. A plasma at temperature T follows the Maxwell-Boltzmann distribution of velocities:

$$f(v) = \sqrt{\frac{2}{\pi}}\left(\frac{m}{k_B T}\right)^{3/2} v^2 e^{-mv^2/2k_B T} \tag{2.9}$$

The observed X-ray flux at Earth from this plasma as a function of energy can then be calculated (see Aschwanden 2004 for a full derivation):

$$F(\epsilon) \approx 8.1 \times 10^{-39} \int \frac{\exp(-\epsilon/k_B T)}{T^{1/2}} n^2 dV \quad (\text{keV s}^{-1}\text{ cm}^{-2}\text{ keV}^{-1}) \tag{2.10}$$

where T is the plasma temperature, k_B is Boltzmann's constant, and ϵ is the photon energy. It has been assumed throughout that the electron and ion densities are equal

($n_e = n_i = n$). While coronal plasmas are generally multi-thermal, HXR spectra are often fit well by a single temperature model. For an isothermal plasma the bremsstrahlung spectrum can be characterized by two parameters: the temperature T and emission measure EM. The plasma density at a given temperature is squared and integrated over the region of interest:

$$EM = \int n^2 dV \qquad \text{Volumetric} \tag{2.11}$$

$$EM = \int n^2 dz \qquad \text{Line-of-sight} \tag{2.12}$$

Emission measure has units of either cm^{-3} or cm^{-5}. After integrating, dividing by ϵ to obtain the photon number, and re-writing in terms of EM, this equation becomes:

$$I(\epsilon) \approx 8.1 \times 10^{-39} \frac{EM}{\epsilon T^{1/2}} \exp(-\epsilon/k_B T) \quad (\text{photons s}^{-1}\text{ cm}^{-2}\text{ keV}^{-1}) \tag{2.13}$$

We can now see that a purely thermal (bremsstrahlung) spectrum falls off quickly with energy at a rate that depends on the temperature. Note that this emission differs from a thermal blackbody spectrum in which the medium is optically thick. In the X-ray energy range ($\gtrsim$1 keV) bremsstrahlung is the dominant emission mechanism (compared to e.g. inverse Compton scattering, synchrotron emission, or recombination; Kontar et al. 2011). In solar flares, thermal X-ray emission is produced by hot ($\gtrsim$10 MK) plasma in loop structures. It should be noted that thermal X-ray spectra can include significant fractions ($\lesssim$30% in the range ~10–30 keV) of recombination (free-bound) emission. However, free-free emission is the dominant component for thermal and non-thermal emission at keV energies.

2.2.2 Non-thermal Bremsstrahlung

Solar flares are known to accelerate particles to high energies such that they form non-Maxwellian (non-thermal) distributions. This acceleration is thought to occur in the corona (see 2.1.1); bremsstrahlung collisions can occur either in-situ or in the high-density chromosphere. Therefore I distinguish between "thin-target" and "thick-target" bremsstrahlung. The latter occurs when electrons deposit most of their energy in a dense collisional medium, and the former occurs when electrons deposit small amounts of energy and/or are continuously accelerated such that their distribution is not significantly changed by the medium.

Let us consider an electron with energy E_o colliding with a fully-ionized hydrogen plasma of density n_p. Photons with energy ϵ are produced at a rate of $n_p \sigma_\epsilon(E_o) v(E_o)$, where $v(E_o)$ is the electron speed and $\sigma_\epsilon(E_o)$ is the electron bremsstrahlung cross-section. For a distribution of electrons with differential number density $N(E)dE$ incident on a target volume V, the emitted photon flux can be expressed as (Brown 1971)

$$I(\epsilon) = n_p V \int_\epsilon^\infty \sigma_\epsilon(E) v(E) N(E) dE \quad (\text{photons s}^{-1}\text{ cm}^{-2}\text{ keV}^{-1}) \tag{2.14}$$

Flare-accelerated electrons typically follow a power-law distribution in energy:

$$f(E) \propto E^{-\delta} \tag{2.15}$$

For both the thick- and thin-target cases, the photon spectrum resulting from a power-law electron distribution will also be a power-law with a different spectral index

$$I(\epsilon) \propto \epsilon^{-\gamma} \tag{2.16}$$

Brown (1971) and Lin (1974) derived the following relations between the observed photon power-law index and the initial electron power-law index:

$$\gamma = \delta + 1 \quad \text{Thin-target} \tag{2.17}$$

$$\gamma = \delta - 1 \quad \text{Thick-target} \tag{2.18}$$

Spatially integrated spectra of solar flares generally show both a thermal and a power law (non-thermal) component resulting from the bremsstrahlung processes described above. Hard X-rays observed at the footpoints of magnetic loops are interpreted in the standard flare model as thick-target emission from electron beams impacting the chromosphere. These sources are usually higher energy than the loops themselves, as would be expected from this model. Occasionally HXR sources can be seen in the high corona (e.g. Masuda et al. 1994, Krucker et al. 2010); because of low densities at these heights this emission is likely produced by thin-target interactions.

2.2.3 Emission Lines

There are a wide variety of absorption, emission, excitation, ionization, and recombination processes that contribute to the continuum and line fluxes in the corona (see e.g. Aschwanden 2004 Chapter 2). Detailed atomic physics calculations have been performed in order to determine the equilibrium ratios for various elemental ions at different temperatures, e.g. Arnaud & Raymond (1992). The *CHIANTI*[1] package is the most widely-used atomic database for solar physics (Dere et al. 1997; Del Zanna et al. 2015). This database contains atomic energy levels, wavelengths, radiative and excitation data for wavelengths between ∼1 and 1700 Å. *CHIANTI* also contains several elemental abundance tables (e.g. Feldman 1992), although it is known that coronal abundances can vary with location and with time. To compute the intensity of a particular spectral line of wavelength λ the following formula can be used:

$$I(\lambda) = \int G(T, \lambda, A_X, n_e) n_e n_H dz \tag{2.19}$$

Here n_e and n_H are the electron and hydrogen densities, T is temperature, $A_X = N(X)/N(H)$ is the abundance relative to hydrogen of element X, z is the line-of-sight through the emitting plasma, and G(T, λ, A_X, n_e) is a "contribution function" that includes all important collisional and radiative excitation and de-excitation mechanisms for the line of interest. Typically electron and ion densities are about equal ($n_e = n_i = n$), and the intensity formula is re-written using a convenient quantity called the differential emission measure (DEM):

$$I(\lambda) = \int G(T, \lambda, A_X, n_e) \frac{DEM(T)}{dT} dT \tag{2.20}$$

where the DEM is defined as

$$DEM(T)/dT = n^2 dV/dT \qquad \text{Volumetric} \tag{2.21}$$

$$DEM(T)/dT = n^2 dz/dT \qquad \text{Line-of-sight} \tag{2.22}$$

The units of a DEM are cm^{-3} K^{-1} or cm^{-5} K^{-1} for volume and line-of-sight integration, respectively. It is a measure of the amount of plasma that contributes to

---

[1] `http://www.chiantidatabase.org/`

the temperature range between T and T+dT. An emission measure (EM, Eqn. 2.11) may be appropriate for a limited energy range, but the DEM is more useful for multi-wavelength or multi-instrument observations where a wide range of temperatures can be detected. As an example, Figure 2.5 shows a DEM generated from sixteen spectral lines seen by the *Hinode* EUV Imaging Spectrometer (EIS). While useful, DEM distributions are also subject to non-uniqueness and large uncertainties due to the "ill-posed" nature of their calculation (Craig & Brown 1986). Temperature-integrated spectral line intensities are the observed quantity, and DEMs must be derived from them. A general principle is that the more data points (e.g. spectral lines) available to calculate a DEM, the better.

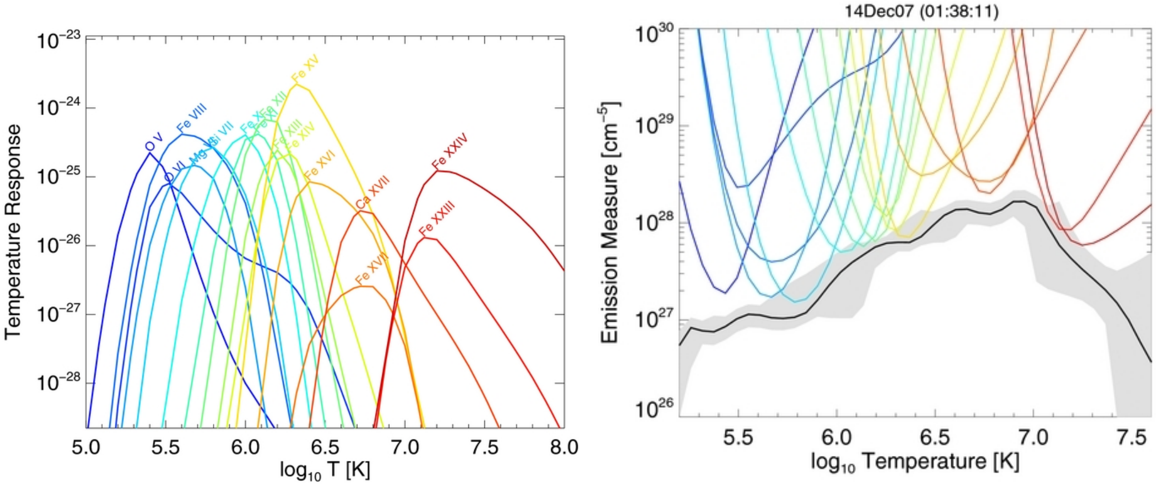

Figure 2.5: Example emission measure distribution from *Hinode*/EIS observations of flare footpoints. (Left) Temperature response functions for each spectral line that was used in this analysis, calculated using coronal abundances, the CHIANTI 7.0 ionization equilibrium, and a constant density of 10^{11}cm^3. (Right) Emission measure distribution generated from the spectral lines in the left panel. The colored curves are known as EM loci and indicate the maximum possible emission for each line. Figure from (Graham et al. 2013).

2.3 Observing the Corona

2.3.1 Instruments

Hard X-rays

The first HXR observation of a solar flare was made by a balloon flight over Cuba (Peterson & Winckler 1958). The first instrument to regularly image hard X-ray flares was the *Hard X-Ray Imaging Spectrometer (HXIS)* (van Beek et al. 1980; Hoyng et al. 1981) onboard the *Solar Maximum Mission (SMM)*. HXIS used a multi-component collimator to image 3.5–30 keV photons with a resolution of $32''$. A similar instrument was flown on the Japanese *Hinotori* satellite (see e.g. Takakura et al. 1983). In 1991 the *Hard X-Ray Telescope (HXT)* onboard the *Yohkoh* spacecraft became the first instrument to image X-rays at energies >30 keV with spatial resolution of ~ 5–$8''$ (Kosugi et al. 1991). In order to achieve this, *HXT* used an indirect imaging system with 64 collimators. These collimators provided measurements of 32 independent spatial Fourier components for an imaged source such that imaging could be accomplished using inversion algorithms. The primary limitation of HXT was energy resolution; it could only generate images in 4 wide energy bins (15–24 keV, 24–35 keV, 35–57 keV, and 57–100 keV).

RHESSI (Lin et al. 2002) just reached its 15th year in orbit on 2017 February 5. *RHESSI* uses a rotating Fourier imaging system with 9 collimators to achieve angular resolution as fine as $\sim 2.3''$ (Hurford et al. 2002). In addition, *RHESSI* uses 9 cooled Ge detectors (one per collimator) to achieve energy resolution 1 keV at its lower energy bound of 3 keV (Smith et al. 2002). These detectors are divided into front and rear segments; the front segments stop $\sim$3–150 keV photons, and the rear segments stop photons up to $\sim$17 MeV (including nuclear gamma ray lines). In addition, *RHESSI* has two movable shutters (thin and thick) that automatically move in front of the detectors when flux levels are high, thereby increasing the dynamic range. *RHESSI* flare observations have provided a wealth of imaging and spectroscopic information of events with fluxes ranging over 7 orders of magnitude; see Figure 2.6 for examples.

RHESSI is the only active, solar-dedicated observatory that can perform HXR imaging spectroscopy. While *RHESSI* continues to operate well, decreasing cryocooler efficiency has resulted in a slowly rising detector temperature. In order to keep the instrument cool, only two of the nine detectors are now turned on during quiet solar periods. This highlights the need for a new solar-dedicated HXR observatory, which I discuss in Chapter 6.

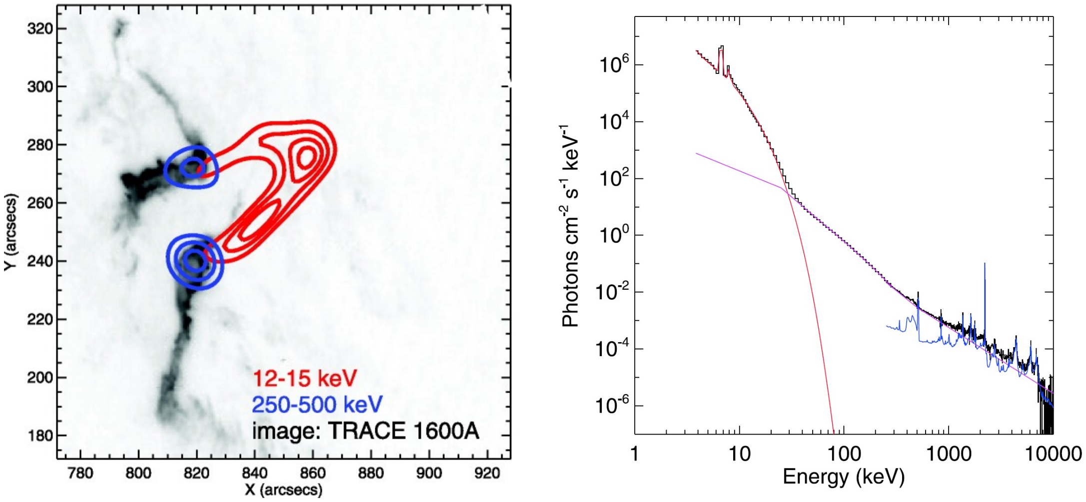

Figure 2.6: (Left) A solar flare imaged by *RHESSI* with a standard loop plus footpoints geometry. Footpoint emission is generally higher in energy. Figure from Krucker et al. (2008) (Right) *RHESSI* spectrum of a large flare including a thermal component (red), a non-thermal power law (violet) and an ensemble of gamma-ray spectral lines (blue). The majority of flares observed by *RHESSI* do not have detectable emission above 100 keV. Figure from Lin (2011).

Soft X-rays

The workhorses of soft X-ray observations for the last $\gtrsim$30 years have been the *Geostationary Operational Environmental Satellites* (GOES, e.g. Mallette 1982). Each of the *GOES* satellites (three are currently operational) records spatially and spectrally integrated flux in two channels with wavelength ranges 1–8 Å and 0.5–4 Å (corresponding to energies of 1.5–12.4 keV and 3.1–24.8 keV). All *GOES* satellites since the twelfth in the series (launched in 2001) have carried a full Sun SXR imaging telescope called the Solar X-Ray Imager (Hill et al. 2005). This instrument used a set of metallic filters in combination with Wolter-I focusing optics (see Chapter 3) to choose different temperatures in the 6–60 Å bandpass. Full-Sun SXR imaging was first done with the Soft X-ray Telescope (SXT) aboard the *Yohkoh* satellite. SXT imaged the disk at 0.25–4.0 keV with spatial resolution of ∼3 arcsec. The *Hinode* satellite, launched in 2006, carries an X-Ray Telescope (XRT) with unprecedented spatial (2 arcsec) and temporal (2 s) resolution (Golub et al. 2007). Similar to SXI, XRT uses a range of metallic filters and focusing optics. *Hinode* also carries the EUV Imaging Spectrometer (EIS), a limited field of view (FoV) spectrograph that observes coronal and transition region emission lines from 170 to 210 Å and 250 to 290 Å and effective temperature coverage at T=0.04 MK,0.25 MK,1.0–20 MK (Culhane et al. 2007).

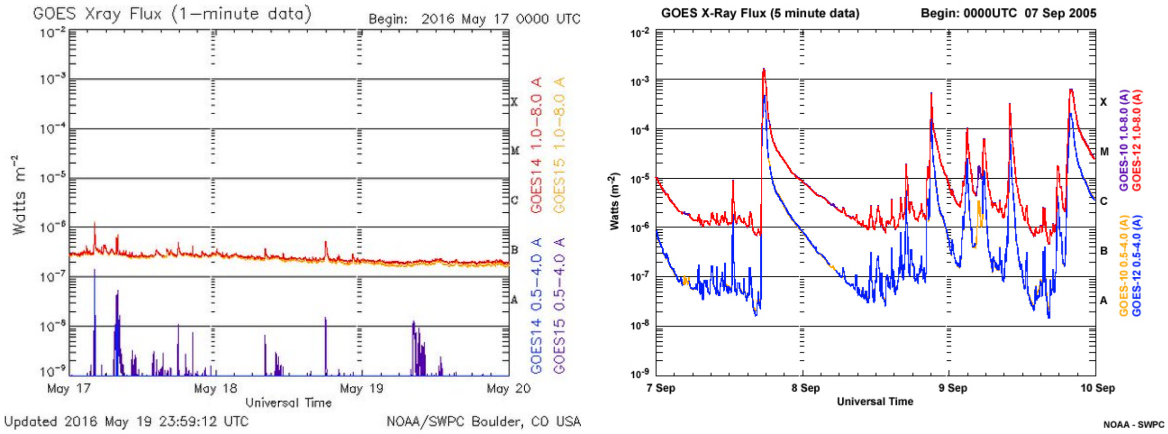

Figure 2.7: Two *GOES* time series from different parts of the solar cycle. (Left) *GOES* flux approaching the current solar minimum. (Right) *GOES* flux towards the end of solar maximum in solar cycle 23. Images courtesy of NOAA/SWPC.

Extreme Ultraviolet

The first normal incidence EUV telescope to image the full disk of the Sun was flown in 1987 aboard a sounding rocket (Walker et al. 1988). In 1995 the Extreme ultraviolet Imaging Telescope (EIT) was launched aboard the *SOHO* satellite (Delaboudinière et al. 1995). EIT made high-resolution (∼5 arcsec) images of the corona and transition region several times an hour in four spectral emission lines: Fe IX

(171 Å), Fe XII (195 Å), Fe XV (284 Å), and He II (304 Å). He II has a peak temperature of ∼8×10^4 K (transition region), while the three iron lines all have peak temperatures between 1 and 3 MK (corona). The *Transition Region and Coronal Explorer (TRACE)* was launched in 1998 and imaged the same iron lines as EIT in addition to five longer-wavelength UV channels (Handy et al. 1999). *TRACE* had higher spatial (∼1 arcsec) and temporal resolution (∼1 minute) but a smaller FoV (8.5×8.5 arcmin) which necessitated frequent re-pointing at different targets of interest.

The *Solar Dynamics Observatory* was launched in 2010 and is providing a wealth of information about the solar atmosphere and dynamics (Lemen et al. 2012). The EUV imaging instrument aboard *SDO* is the Atmospheric Imaging Assembly (AIA) (Lemen et al. 2012). AIA images the corona in six EUV channels (94, 131, 171, 193, 211, and 335 Å) and lower layers of the atmosphere in several additional wavelengths. Spatial resolution is ∼1 arcsec for a full-Sun (41×41 arcminute) FoV. All of the EUV channels are centered on iron spectral lines to ensure that temperature and density diagnostics with various channels won't be affected by varying abundances. However, weaker lines also contribute to each channel and can make precise temperature inversion difficult. *SDO*/AIA observes plasma over a fairly large temperature range ∼0.5–10 MK.

2.3.2 Non-Flaring Active Regions

The "steady-state" corona during most of the solar cycle contains a mixture of active regions and quiet Sun regions (Section 1.2.3). The physical properties (e.g. temperature, density) of quiescent active regions have been studied primarily using EUV and SXR instruments; only recently have HXR imaging and spectroscopy been feasible. DEM distributions from instruments on *SDO* and *Hinode* have been recently used to map the temperature structure of ARs between $10^{5.5}$ and $10^{7.0}$ K. Warren et al. (2012) used multiple filters on *SDO*/AIA and multiple spectral lines observed by *Hinode*/EIS observations to construct DEMs for fifteen active regions, and found that their temperatures peaked at ∼4 MK with sharper peaks for regions with stronger magnetic fields. The temperature distributions of active regions are a direct result of coronal heating mechanisms. The properties of these distributions such as the peak temperature, slopes on either side of the peak, and ratio of high to low temperatures can therefore be used to distinguish between different coronal heating theories (Section 2.4). I discuss hard X-ray spectroscopy of active regions with *NuSTAR* and *FOXSI* and derive constraints on coronal heating mechanisms in Chapters 3 and 5, respectively.

2.3.3 Flares

Flares occur across a large range of energy scales, from $\leq 10^{24}$ to 10^{33} ergs. The historic classifications of flares with energy is as follows: "large flares" release $\sim 10^{30}$–10^{33} ergs, "microflares" release $\sim 10^{27}$–10^{30} ergs, and "nanoflares" release $\sim 10^{24}$–10^{27} ergs. The term "nanoflare" is now used to describe non-resolvable impulsive heating events (see Section 2.4.2). Most flares have an impulsive rise followed by a gradual decay and higher energy bands that peak earlier.

Flares are categorized by intensity based on SXR measurements from *GOES*. Flare classifications are A, B, C, M, X from small to large. These correspond to logarithmically spaced fluxes (starting at A1.0) of 10^{-8} up to 10^{-4} in W m^{-2}. Following the discussion above, large flares are typically C, M or X class, microflares are A or B class, and nanoflares are sub-A class. The Sun typically emits enough SXRs to be seen by *GOES* even during quiescent periods, although in 2009 (the last solar minimum) flux levels frequently dropped below the instrument detection limit. Figure 2.7 shows *GOES* light-curves over a period of several days at solar maximum and near solar minimum. *GOES* emission is dominated by the lower energies in each channel due to the steeply-falling nature of typical X-ray spectra (see Section 2.2.1).

Large flares occur only in active regions (Figure 2.8). This also seems to be true of lower-energy microflares, surveys of which have been done with e.g. *Yohkoh*/SXT (Shimizu 1995) and *RHESSI* (Christe et al. 2008; Hannah et al. 2008). These studies have shown that microflares are very similar to larger flares: they have thermal (and sometimes non-thermal) spectral components, occur only in active regions, exhibit a quicker rise in higher-temperature light-curves, and have loop-like structures. As shown in Figure 2.1, many flares share a common geometry in HXRs. Three compact sources (two footpoints and a loop) is the configuration most commonly imaged by *RHESSI*; some flares have additional high coronal sources and/or elongated ribbon-like footpoints. Very rarely flares will be seen with no footpoints; this can occur when coronal densities are so high that thick-target emission is seen close to the acceleration site (Veronig & Brown 2004).

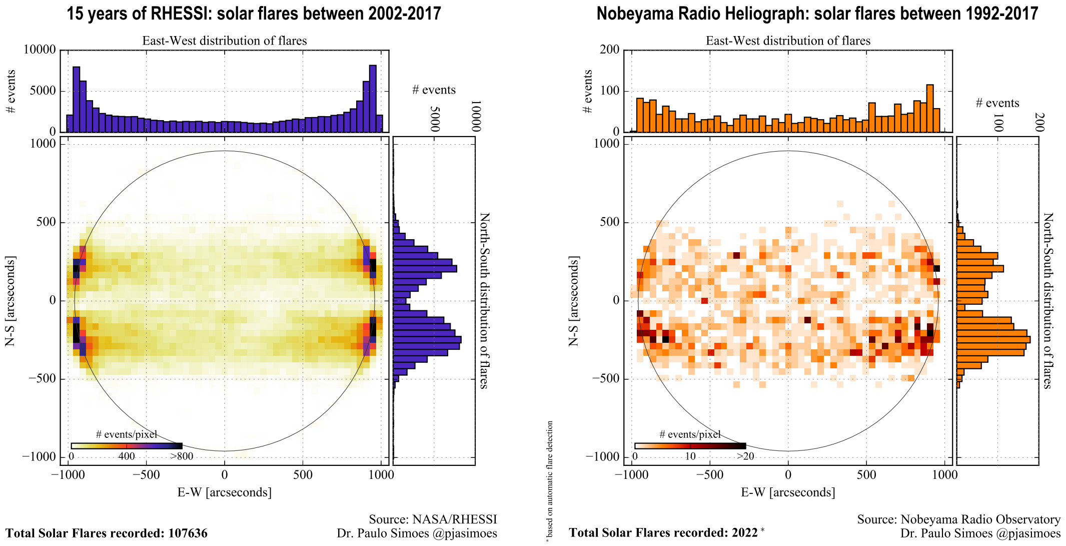

15 years of RHESSI: solar flares between 2002-2017

Nobeyama Radio Heliograph: solar flares between 1992-2017

Total Solar Flares recorded: 107636

Source: NASA/RHESSI
Dr. Paulo Simoes @pjasimoes

Total Solar Flares recorded: 2022 *

Source: Nobeyama Radio Observatory
Dr. Paulo Simoes @pjasimoes

Figure 2.8: Flare locations from the *RHESSI* HXR satellite and the *Nobeyama* radio telescope over a fifteen year period beginning in 2002. Notably all flares occur at fairly low latitudes, corresponding to the locations of active regions. A greater number of flares is seen on the limb due to projection effects. All events and positions were taken from the *RHESSI* and *Nobeyama* flare catalogs. The former may contain duplicates if satellite night or SAA passage occurred during a long flare, and the latter is less sensitive to small flares. Figure courtesy of P. J.A. Simões (private communication)

2.3.4 The Quiet Sun

While large flares and coronal hard X-ray emission have only been seen in active regions, there are several interesting transient phenomena that have been observed in the quiet Sun. “X-ray Bright Points” are small, bright features seen in SXRs that can occur everywhere on the Sun. They have lifetimes ∼1–20 hours, over the course of which they release 10^{26}-10^{28} ergs of energy (Golub et al. 1974). These features can also increase several orders of magnitude in brightness on minute time scales, a phenomenon similar to active region flares (Sheeley & Golub 1979; Shimojo & Shibata 1999).

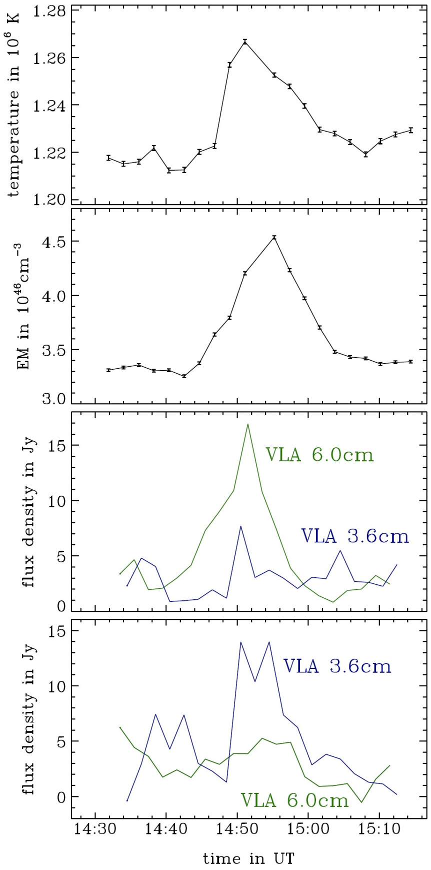

Figure 2.9: Time profiles of a quiet Sun transient event observed in Fe XI/X and Fe XII lines at 171 Å and 195 Å by EIT/SOHO. (Top) Temperature averaged over the area of the event (Top middle) Emission measure averaged over the area of the event. (Bottom middle) VLA radio fluxes at 6 and 3.6 cm at the location of the 6 cm peak. (Bottom) VLA radio fluxes at 6 and 3.6 cm at the location of the 3.6 cm peak. Figure from Benz (2017), adapted from Krucker & Benz (2000).

Small flare-like events occur in the quiet Sun outside of active regions and X-ray bright points, and have been observed in EUV and SXR (Krucker et al. 1997; Krucker & Benz 1998; Aschwanden et al. 2000; Parnell & Jupp 2000). They have temperatures T ≈ 1–2 MK, significantly cooler than active region flares. These events have been given names such as “network flares”, “network heating events”, “EUV brightenings”, etc. They are also referred to as “nanoflares”, though I follow the example of many authors and use nanoflares to refer to non-resolvable events that might heat the corona (Section 2.4.2). For consistency I refer to flare-like brightenings in the quiet Sun with the generic moniker of “quiet Sun transient events”. A helpful overview of such events can be found in Harrison et al. (2003). In general they appear to share many properties with larger flares: they occur in small-scale loops, exhibit an impulsive rise and decay, and exhibit a time delay between high and low temperature bands (Krucker & Benz 2000). Figure 2.9 shows an example of a quiet Sun transient event observed with EUV and radio instruments.

Because they are so faint and emit at low temperatures, these events have not been detected by HXR instruments. Most recently, *RHESSI* has been an incredibly successful flare science mission but lacks the sensitivity and dynamic range necessary for imaging spectroscopy of non-flaring active regions and the quiet Sun. Hannah et al. (2007, 2010) used a novel off-pointing technique to determine *RHESSI* upper limits on quiet Sun emission; no detection was found in either study. I present the results of a search for quiet Sun transient events with the *NuSTAR* focusing HXR telescope in Chapter 4.

2.4 The Coronal Heating Problem

The high temperature of the solar corona has puzzled scientists ever since its discovery. Grotrian (1939) and Edlén (1943) first identified highly ionized lines of Fe IX and Ca XIV in the coronal spectrum, implying a temperature >1 MK. This was an unexpected contrast to the photospheric temperature of ∼6000 K (see Figure 1.3). In order for the corona to be as hot as it is, there must be physical mechanisms in addition to thermal conduction that transfer energy and heat from the photosphere. The net energy flux into the corona must, at the very least, balance its energy losses. Withbroe & Noyes (1977) used empirical models to calculate energy loss from several layers of the solar atmosphere; for the corona they found values between 10^5 and 10^7 erg cm^{-2} s^{-1} (see Table 2.1). The heating requirements are different in active regions and quiet Sun regions, as would be expected.

Parameter	Quiet Sun	Active Region
Transition layer pressure (dyn cm^{-2})	2×10^{-1}	2
Coronal temperature (K, at $r \approx 1.1 R_{Sun}$)	1.1 to 1.6×10^6	2.5×10^6
Coronal energy losses (erg cm^{-2} s^{-1})		
Conduction flux F_c	2×10^5	10^5 to 10^7
Radiative flux F_r	10^5	5×10^6
Solar wind flux F_w	$\lesssim 5 \times 10^4$	$< 10^5$
Total corona loss $F_c + F_r + F_w$	3×10^5	10^7
Chromospheric radiative losses (erg cm^{-2} s^{-1})		
Low chromosphere	2×10^6	$\gtrsim 10^7$
Middle chromosphere	2×10^6	10^7
Upper chromosphere	3×10^5	2×10^6
Total chromospheric loss	4×10^6	2×10^7
Solar wind mass loss (g cm^{-2} s^{-1})	$\lesssim 2 \times 10^{-11}$	$< 4 \times 10^{-11}$

Table 2.1: Temperatures and energy losses for the corona and chromosphere, from Withbroe & Noyes (1977). Losses are tabulated separately for active regions and the quiet Sun.

For detailed overviews of the coronal heating problem I refer the reader to Aschwanden (2004), Klimchuk (2006), and Parnell & De Moortel (2012). What follows is a summary of possible heating mechanisms and the observational evidence associated with each.

It is generally accepted that mechanical motions in and below the photosphere are the ultimate drivers of coronal heating (Klimchuk 2006). Magnetic footpoints are displaced and tangled as a result of these motions, and energy is injected into the fields (Figure 2.10). The Poynting flux associated with flows stressing the magnetic fields is given by

$$F = \frac{1}{4\pi} B_V^2 V_h \tan(\theta) \tag{2.23}$$

where B_V is the vertical component of the field, V_h is the horizontal velocity and θ is the tilt angle of the field. Observations suggest that θ typically ranges from 10 to 20

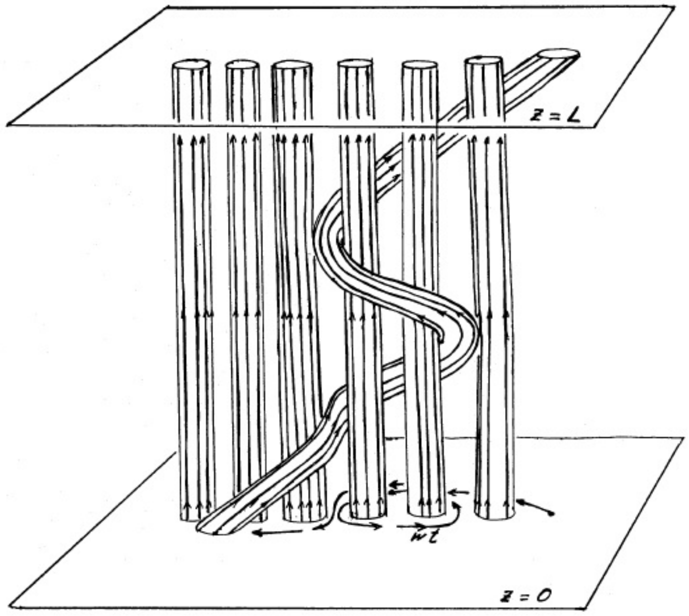

Figure 2.10: Magnetic field lines can become braided and tangled due to the random walk of their photospheric footpoints. Figure from Parker (1983).

degrees, while B_V and V_h have typical values 10–100 G and 1 km s^{-1}.

Coronal heating mechanisms are generally divided into two categories based on two results of photospheric driving: waves (AC heating) and magnetic energy dissipation (DC heating). DC heating is a result of magnetic footpoint motion that twists and stresses field lines until they reconnect and release energy. The Poynting flux from these motions (Equation 2.23) is sufficiently large that the corona may be heated entirely by dissipation. Those same photospheric motions can generate different types of waves that propagate up through the solar atmosphere, but most waves will be strongly reflected and/or refracted at the steep density and temperature gradients in the transition region. Srivastava et al. (2017); McIntosh et al. (2011) and others have claimed the detection of Alfvén waves with sufficient energy to balance coronal losses, although wave dissipation sites could not be accurately determined in those studies. If these waves don't dissipate their energy in the corona then their heating contribution will be negligible. Much work remains to be done to determine if wave heating makes a significant contribution to the coronal energy budget.

Small chromospheric jets known as "spicules" have been considered as a source of coronal heating, based on the recent discovery of a previously unknown variety (De Pontieu et al. 2011, 2009). The tips of these "type II spicules" were seen to reach coronal temperatures, in contrast to previous low-temperature observations. While some authors claimed that spicules could transfer enough matter to replace the coronal energy loss, others (e.g. Klimchuk 2012; Klimchuk & Bradshaw 2014) have shown that a corona primarily heated by spicules is incompatible with observations. In particular, spicule heating models predict red-blue asymmetries of EUV spectral lines and lower transition region to coronal emission measure ratios that are ∼2 orders of magnitude larger than observed. Spicules most likely contribute a small fraction (<10%) of the hot plasma in the corona.

2.4.1 Flare Heating

Flares release energy into the corona and chromosphere, and could provide a significant part of the heat flux needed to maintain the corona's high temperature. The coronal heating contribution of solar flares can be dominated by either large or small events, depending on the power-law index of their frequency distribution (Hudson 1991):

$$\frac{dN}{dU} = AU^{-\alpha} \tag{2.24}$$

Here U is the energy in a flare, $\alpha > 0$ is the power-law index, and A is a scaling constant. The total power contained in the flare distribution can be computed from this distribution as follows:

$$P = \int_{U_{min}}^{U_{max}} \frac{dN}{dU}\, U\, dU = \frac{A}{2-\alpha}\, U^{2-\alpha} \Bigg|_{U_{min}}^{U_{max}} \tag{2.25}$$

Since $U_{max} >> U_{min}$ the smallest flares will contain the most energy if $\alpha > 2$ (and vice versa). Since the integrated energy release from large flares is over 2 orders of magnitude below even the quiet Sun coronal heating requirements (Hudson 1991), small flares must dominate energetically in order for flares to be a viable coronal heating mechanism. The observed power-law index is close to the critical value but is difficult to determine precisely due to large uncertainties and the variety of instruments used to generate the distribution (Hannah et al. 2011; see Figure 2.11). Therefore it is still unclear whether large or small flares provide more heat and energy to the solar corona. Another open question is whether tiny nanoflares on individual magnetic strands (Section 2.4.2) stem from similar physical processes as larger flares and microflares (e.g. Hannah et al. 2008).

2.4.2 Nanoflare Heating

Gold (1964) first introduced the idea that photospheric motions can lead to tangling of magnetic flux tubes and subsequent energy release via magnetic reconnection. Parker (1988) took this idea further and postulated that the entire Sun is covered with "nanoflares," which he defined as any individual energy release (heating event) below the level of conventional microflares ($\leq 10^{27}$ ergs). Cargill (1994) studied the coronal response to a collection (many hundreds) of elemental flux tubes randomly subjected to nanoflare heating events, and found that widespread nanoflare heating produces small amounts of high-temperature ($\geq$5 MK) plasma. This is now referred to as the "smoking gun" of nanoflare heating. In addition, he found that the distribution of plasma at different coronal temperatures (the emission measure distribution, Section 2.2.3) has a double-sloped shape, with a shallow (positive) slope below $\sim$5 MK and a steeper (negative) slope above $\sim$5 MK. Because his analysis focused on the coronal response to nanoflare heating, Cargill (1994) did not need to specify the physical mechanism behind the nanoflares. Nanoflares in this sense can be a result of AC (e.g. waves) or DC (e.g. reconnection) processes. This approach has been followed subsequently by many others, and the term "nanoflare" is now used as a general term for (unresolveable) impulsive heating events in individual magnetic flux strands. A strand is an extremely thin magnetic loop for which the heating and plasma properties are approximately uniform on a cross section.

There are two main reasons why the hot plasma from nanoflares is expected to be so faint (discussion adapted from Bradshaw & Klimchuk 2011). First, impulsive heating should take place in the corona under relatively low-density conditions. This produces a strong downward heat flux that results in chromospheric evaporation. The combination of short heating time scales and the relatively long time scale for

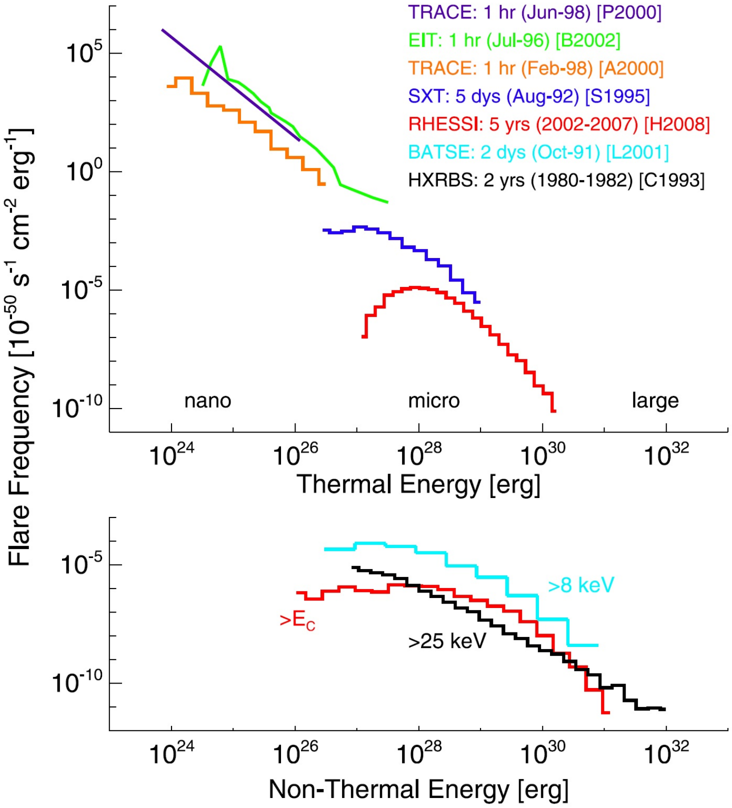

Figure 2.11: Flare frequency distributions from multiple instruments with different energy ranges. (Top) Thermal events are shown both from active regions (microflares seen by*RHESSI* Hannah et al. 2008 and *Yohkoh*/SXT Shimizu 1995) and the quiet Sun (*TRACE*, Parnell & Jupp 2000; Aschwanden et al. 2000; *SOHO*/EIT, Benz & Krucker 2002). (Bottom) Non-thermal energy distributions shown are *RHESSI* microflares above the low-energy cutoff (E_C) (Hannah et al. 2008), *CGRO*/BATSE microflares >8 keV (Lin et al. 2001), and large flares >25 keV observed with *SMM*/HXRBS (Crosby et al. 1993). Note that the methodology and flare locations used to derive different distributions can vary greatly. Figure from Hannah et al. (2011).

chromospheric evaporation means that significant conductive cooling of the coronal plasma can occur after the highest temperature has been reached, but before the coronal density can increase enough for high-temperature emission to be seen. The second reason is related to the standard assumption of ionization equilibrium. Short heating time scales lead to rapid temperature increases with which the change in ionization state is unable to keep pace; when the peak temperature is reached the plasma generally contains many more ions in lower charge states (and fewer ions in highly charged states) than would be the case at the same temperature under equilibrium conditions. Therefore, emission from the highly charged ions that would be a signature of hot plasma can be much weaker than expected.

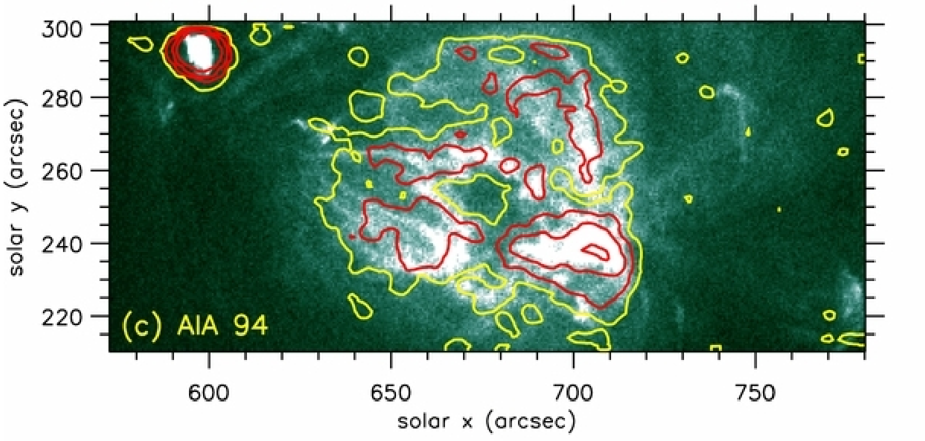

Figure 2.12: Integrated intensity map of the Fe XIX spectral line (peak T $\approx$ 8.9 MK) from the EUNIS sounding rocket. Contour levels are 4 (yellow), 8, 16, and 32 erg cm^{-2} s^{-1} sr^{-1} (red) overlaid on a 94 Å image from *SDO*/AIA. Figure from Brosius et al. (2014).

It is now commonly accepted that the corona is heated impulsively, i.e. by nanoflares, from the perspective of individual magnetic strands (Klimchuk 2015). There are several lines of observational evidence that support this. Several features of warm (T$\sim$1 MK) loops (their long lifetime, high density, and narrow DEM) are well-explained by ensembles of impulsive heating events (Warren et al. 2003). Viall & Klimchuk (2012) discovered a time-lag signal in *SDO*/AIA images consistent with cooling plasma throughout a particular active region, a signal at odds with steady heating. These results have been replicated for other active regions and the quiet Sun by e.g. Viall & Klimchuk (2015b,a). Possibly the most compelling piece of evidence is the direct detection of hot ($\sim$8.9 MK) plasma (the "smoking gun" of nanoflare heating) by the EUNIS sounding rocket (Brosius et al. 2014). EUNIS observed relatively faint emission of Fe XIX in a significant fraction (>60%) of an active region (Figure 2.12). The hottest plasma produced by nanoflares may be detectable by hard X-ray (HXR) instruments with enough sensitivity; studies with *Hinode*/XRT and *RHESSI* were able to constrain but not definitively detect emission above $\sim$5 MK (Reale et al. 2009; Schmelz et al. 2009). McTiernan (2009) integrated over many *RHESSI* orbits during quiescent times to detect a hot ($\sim$5–10 MK) spectral component in "non-flaring" active regions. A similar result was found with full-Sun observations by SphinX (Miceli et al. 2012), and more recently with the X123 spectrometer (Caspi et al. 2015). It is possible that these observations contained small, resolvable flares ($\lesssim$A1.0 *GOES*-class) to which neither *RHESSI* nor *GOES* are sensitive. Therefore, the HXR evidence for nanoflare heating is ambiguous at best. In order to see hot, faint HXR sources new imaging technology is required: in particular, the use of focusing optics which are discussed in the next chapter.

Chapter 3

Imaging Hard X-rays with Focusing Optics

Abstract

The *NuSTAR* satellite and *FOXSI* sounding rocket use focusing optics to directly image hard X-rays above 2 keV. In comparison to collimators or masked imagers, this technology provides vastly improved sensitivity and dynamic range. Later chapters describe how *NuSTAR* was used to set new limits on HXR transient brightenings in the quiet Sun (Chapter 4), and *NuSTAR* and *FOXSI* were used to constrain the physical properties of small-scale coronal heating events in active regions (Chapter 5). However, focusing HXR photons >10 keV is difficult and has only become technologically feasible in the last ∼10 years. In this chapter a brief history of focusing optics and the relevant physics will be presented, followed by descriptions of the *NuSTAR* and *FOXSI* instruments and initial scientific results.

3.1 Focusing Optics

Mirrors have been used to focus visible and other low-energy wavelengths of light (UV, infrared) for hundreds of years. However, X-rays are so energetic that they will either pass through a glass mirror at normal incidence or get photoelectrically absorbed and scatter in a random direction. The index of refraction of X-rays in solids is slightly less than one, which means X-rays can undergo total external reflection if they are incident at an angle below the critical angle (measured with respect to the surface, not the normal). This critical angle is typically very small (0.14 degrees or 2.5 milliradians at 15 keV), so X-ray optics must be designed so that incoming rays arrive at grazing incidence. X-ray reflectivity is roughly proportional to the mass density of the reflector (Als-Nielsen et al. 2011); therefore denser (higher-Z) materials are generally better for making optics.

In 1951 Wolter (1951a,b) proposed three possible designs for a grazing-incidence X-ray telescope (see Figure 3.1). These concepts used parabolic, hyperbolic, and elliptical mirrors with two sequential reflections to focus X-rays. The Wolter-I system, in which incoming photons reflect sequentially off a parabolic and a hyperbolic mirror, is the most commonly used for astronomical observations because of its compactness, ease of mounting, and because it provides space to add further mirrors inside and outside (Aschenbach 2009). The addition of nested shells of mirrors results in a substantially larger collecting area and is standard practice.

HXR observations of astrophysical sources can benefit greatly from the use of focusing optics. This technology enables instruments with simultaneously large collecting areas and small detectors. Since instrumental background scales with detector area, this results in significant sensitivity increases. In addition, narrow point spread functions (PSF) can be achieved that increase dynamic range relative to indirect imaging instruments.

Giacconi & Rossi (1960) were the first scientists to note the potential value of Wolter optics for astronomical observations. The first focused X-ray images of the Sun were taken in 1965 with Wolter optics on a sounding rocket imaging 8–12 Å (1.0–1.5 keV)(Giacconi et al. 1965). In 1978 the HEAO-2 (Einstein) astronomical observatory became the first satellite to use focusing optics, and was able to image X-ray 0.15–3 keV (Giacconi et al. 1979). Modern SXR astronomy is heavily reliant on the use of focusing optics in astrophysics instruments such as Chandra (Weisskopf et al. 2000), XMM-Newton (Jansen et al. 2001), and Suzaku (Mitsuda et al. 2007)

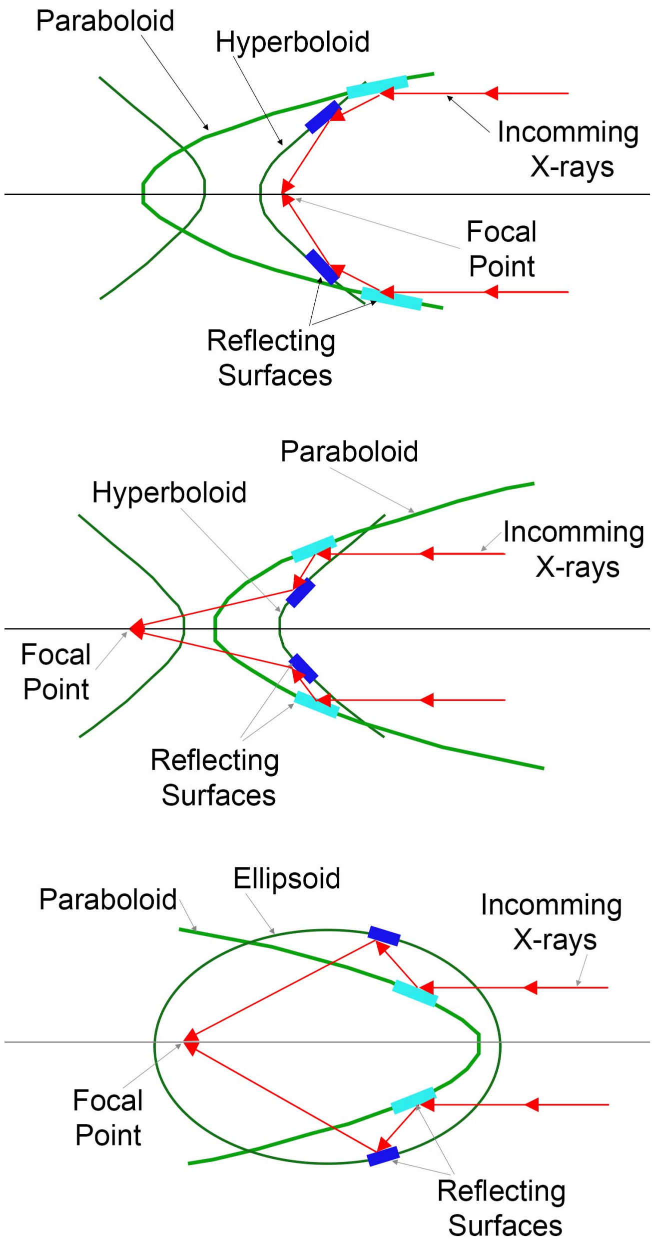

Figure 3.1: (Top) Wolter Type-I focusing telescope design. This is the most commonly used design for X-ray focusing telescopes, both at SXR and HXR energies. (Middle) Wolter Type-II focusing telescope design. (Bottom) Wolter Type-III focusing telescope design. Images courtesy of NASA.

as well as solar instruments such as *Hinode*/XRT and *GOES*/SXI. Until recently, focusing optics have not been used for HXR observations. Because the critical angle for total external reflection scales approximately with wavelength, smaller angles are necessary to focus higher energy X-rays. Precise manufacturing of mirror optics with smooth surfaces (surface roughness on the order of a few angstroms) is required to enable reflectivity at HXR energies.

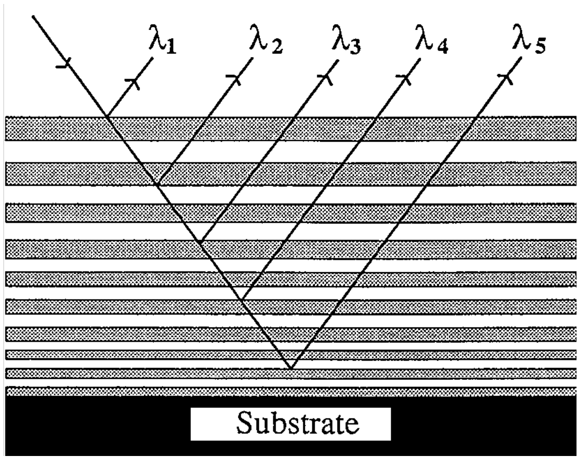

Figure 3.2: Schematic of a depth-graded multilayer coating with alternating layers of a heavy element (dark gray) and light material. The light material acts as a spacer so that the heavy layers can coherently reflect wavelengths that satisfy the Bragg condition (Eqn 3.1). Different wavelengths (energies) are reflected at different depths in the multilayer. Image from Gorenstein (2012).

Another key technology for HXR focusing instruments is multilayer coated optics. A multilayer coating is a stack of two different materials in thin, alternating layers. These coatings extend the range of possible reflection angles using Bragg reflection. The Bragg condition is given by

$$2d\sin(\theta) = m\lambda \tag{3.1}$$

where d is the bilayer thickness, m is an integer (the order of reflection), θ is the angle of incidence, and λ is the wavelength of the incident photon. Constructive interference occurs when this condition is satisfied, and for multilayer coatings this means enhanced reflectivity at particular energies. Reflectivity can be enhanced across a range of energies by using depth-graded multilayers where the thickness is varied throughout the stack (Christensen et al. 1992).

Focusing instruments require position-sensitive X-ray detectors. Semiconductor detectors are the most popular choice for X-ray imagers because of fast collecting times and high energy resolution; common materials include silicon (Si), cadmium telluride (CdTe), and cadmium zinc telluride (CdZnTe). The *FOXSI* and *NuSTAR* detectors are discussed separately below.

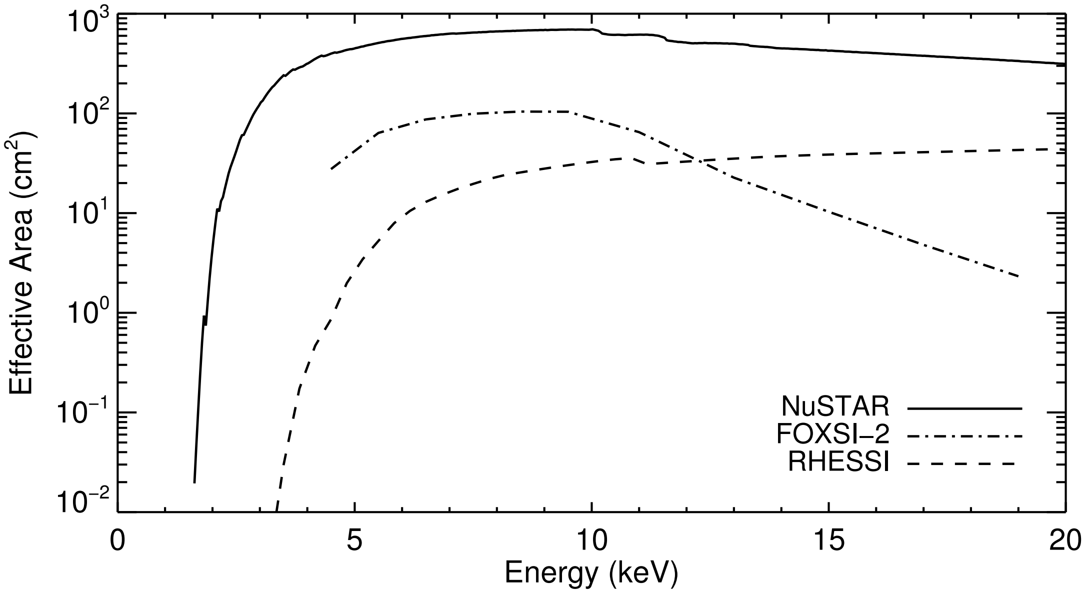

Figure 3.3: Effective area curves for *NuSTAR*, *FOXSI-2*, and *RHESSI*. The *NuSTAR* area includes both telescopes (FPMA & FPMB). The *FOXSI-2* area includes all seven detectors, and the *RHESSI* area includes all nine detectors (front segments).

The increased sensitivity of focusing HXR telescopes is a function of increased effective area and reduced background. Figure 3.3 shows the maximum effective area curves for *NuSTAR*, *FOXSI-2*, and *RHESSI* up to 20 keV. The *NuSTAR* effective area is about an order of magnitude greater than *RHESSI*'s in this energy range. The *FOXSI-2* area is smaller than *RHESSI*'s above ~12 keV due to the constraints of a sounding rocket payload and a lack of multilayer coatings. However, both *FOXSI* and *NuSTAR* have much lower background than *RHESSI* due to the small detector size enabled by focusing optics.

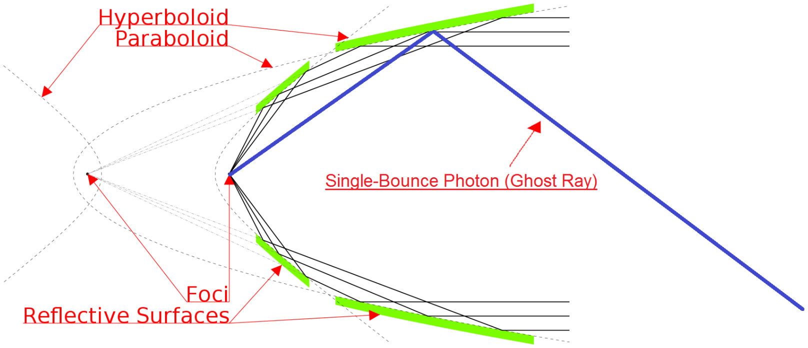

Figure 3.4: Ray-trace drawing of a Wolter-I telescope with properly focused double-bounce photons and one unfocused single-bounce photon (ghost ray) from a source outside the telescope FoV. Image adapted from Wikipedia (`https://en.wikipedia.org/wiki/File:Wolter-I_01.svg`).

Ghost Rays

Imaging X-rays with Wolter-type optics requires that each photon reflect twice before reaching the focal point. However, for sources far enough off axis, photons can reach the focus with only a single reflection (Figure 3.4). These single-bounce photons are known as "ghost rays" and can be a significant source of background for focusing instruments if there are bright sources outside the instrument FoV. Ghost rays form a very distinct spatial pattern (Figure 3.5) and can usually be identified in images. Ray-trace codes can be used to simulate ghost-ray flux from off-axis sources with known intensities, leading to the possible removal of the image artifacts.

3.2 FOXSI

(*FOXSI*) is a sounding rocket payload funded by NASA's Low Cost Access to Space (LCAS) program. *FOXSI* uses focusing optics to image solar HXRs with high sensitivity and dynamic range. It has a FoV of ∼16×16 arcmin and an imaging resolution of ∼9 arcsec (FWHM). *FOXSI* successfully flew for ∼6 minutes on 2012 November 2 (*FOXSI-1*, Krucker et al. 2013) and 2014 December 11 (*FOXSI-2*, Gle-

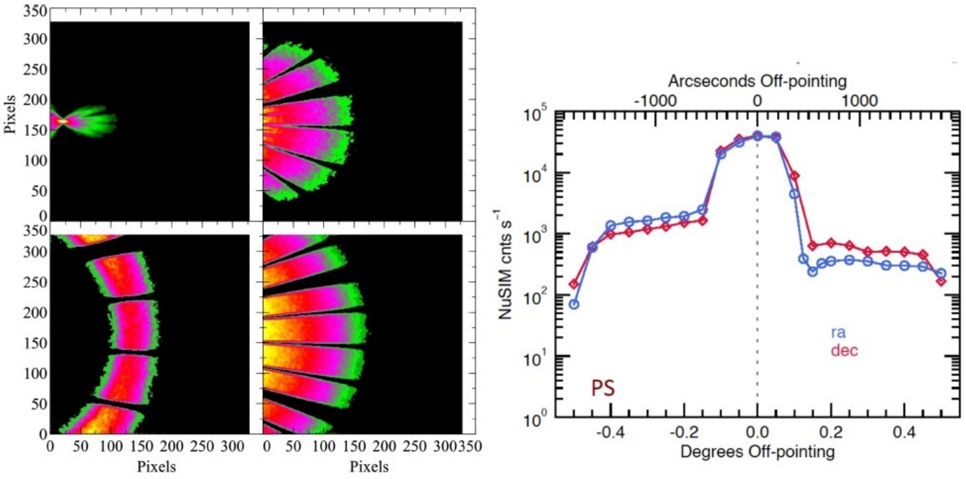

Figure 3.5: (Left) Simulated off-axis point source images that show the spatial patterns created by single-bounce ghost rays in the *NuSTAR* FoV. The panels show the flux from a source located 6, 12, 20, and 30' off-axis (clockwise from the top left). (Right) Simulated *NuSTAR* count flux integrated over the instrument FoV for a large number of off-axis angles, shifted in both RA and DEC (left-right and top-bottom across the focal plane). The central peak with rates $>10^4$ counts sec^{-1} occurs when the source is still in the FoV and is imaged with double-bounced (properly focused) photons. A sharp drop-off occurs as soon as it leaves the FoV, with ghost-ray fluxes 1–2 orders of magnitude lower than the focused flux. Figure from Grefenstette et al. (2016).

sener et al. 2016); an updated version of the instrument (*FOXSI-3*) is scheduled to fly in 2018. The first rocket payload had an energy range of ∼4–15 keV, which was extended to 20 keV for the second flight. A schematic of the *FOXSI* instrument is shown in Figure 3.6.

3.2.1 Optics

FOXSI uses nickel-alloy mirrors made with an electroforming procedure that eliminates the need for individual polishing. Each mirror is one piece with parabolic and hyperbolic segments that form a Wolter-I geometry. *FOXSI* has seven separate optics modules with nested mirrors; the number of shells in each optic was 7 for *FOXSI-1* and 10 for *FOXSI-2*. Due to the space constraints of a sounding rocket payload *FOXSI* has a focal length of only 2m; this and a lack of multilayer coatings restricts

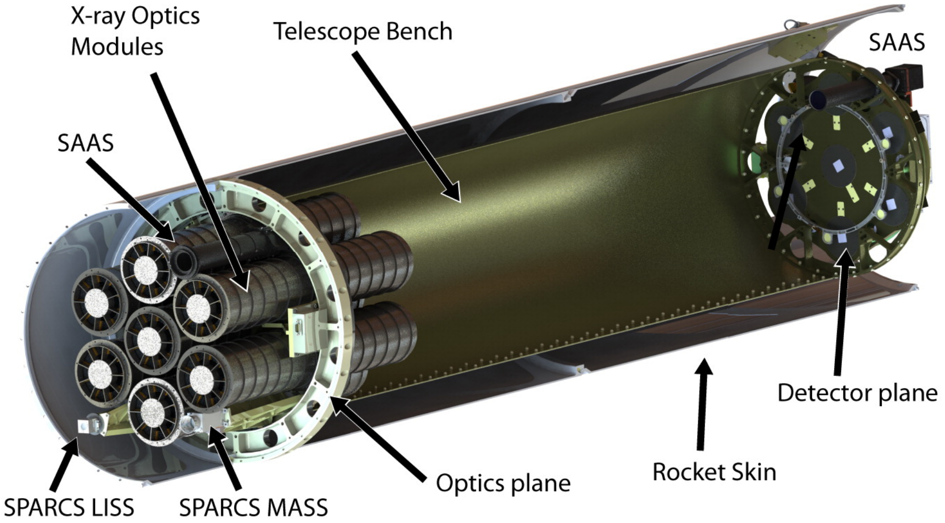

Figure 3.6: The *FOXSI* sounding rocket payload. The seven optics modules focus X-rays onto seven solid-state detectors. The primary solar aspect system for sounding rocket payloads is the SPARCS (Solar Pointing Attitude Rocket Control System), which consists of two small sensors (LISS & MASS). An additional aspect and alignment system (SASS) was added for the *FOXSI-2* flight in order to determine the precise alignment between the SPARCS and the X-ray optics. Figure from Christe et al. (2016).

observations to energies $\lesssim$20 keV. The optics fabrication technique used to build the *FOXSI* mirrors was originally developed for the *High Energy Replicated Optics (HERO)* astrophysics balloon program (Ramsey et al. 2002). *HERO* completed several flights and was followed by an integrated solar/astrophysics balloon re-named *HEROES* (Christe et al. 2013). The technology development in the *HERO* program was an important source of heritage for *FOXSI*.

3.2.2 Detectors

In order to meet its energy and position resolution goals, *FOXSI-1* used seven position-sensitive silicon strip detectors (one for each optics module). These detectors were designed by the Institute of Space and Astronautical Science (ISAS), and featured orthogonal n- and p-doped strips on either side of a monolithic silicon wafer (Ishikawa et al. 2011). Each detector had a total active area of $9.6{\times}9.6\text{mm}^2$ corresponding to an instrument FoV of 16.5×16.5 arcmin^2. For the *FOXSI-2* flight two of the silicon detectors were replaced by CdTe detectors with improved efficiency (almost 100% vs. 66% for the *FOXSI* energy range) and strip pitch (6.2 arcsec vs. 7.7 arcsec), resulting in a slightly smaller FoV (13.2×13.2 arcmin^2). *FOXSI-3* will fly upgraded versions of the CdTe detectors.

3.2.3 Science Goals

The primary science goals of *FOXSI* are 1) imaging acceleration sites in solar flares (in conjunction with loop and footpoint sources) and 2) searching for hot (>5 MK) plasma and non-thermal emission in non-flaring active regions and the quiet Sun. The current solar-dedicated HXR satellite, *RHESSI*, is well-suited for imaging and spectroscopy of flares above GOES A-class. However, it has limited sensitivity and dynamic range due to its indirect (Fourier) imaging system. These are very important instrument parameters for exploring the fundamental physics of particle acceleration and coronal heating.

It is generally accepted that solar flares accelerate particles in the corona; non-thermal HXR signatures have been observed above flare loops on several occasions (Masuda et al. 1994; Krucker et al. 2010; Oka et al. 2015). However, due to limited dynamic range *RHESSI* can't usually see these faint sources unless the flare footpoints (typically 10–100 times brighter) are occulted by the solar limb. An instrument with the ability to detect bright and dim sources in the same FoV would be able to see both particle acceleration sites in the high corona and loop footpoints where those particles deposit their energy.

RHESSI does not have enough sensitivity to detect emission from the quiet Sun (for upper limits see Hannah et al. 2010). In addition, it is generally unable to make images or spectra of individual active regions in a non-flaring state (for full-Sun non-flaring spectra, see McTiernan 2009). As mentioned in Section 2.4.2, nanoflare heating will result in widespread traces of hot ($> 5\ MK$) plasma in the corona. Spatially resolved, high-sensitivity observations of the non-flaring Sun (e.g. Brosius et al. 2014) can detect this plasma if it is present. Hard X-rays will be emitted by that hot plasma, or by non-thermal particles accelerated in flares below the sensitivity of *RHESSI* and *GOES*.

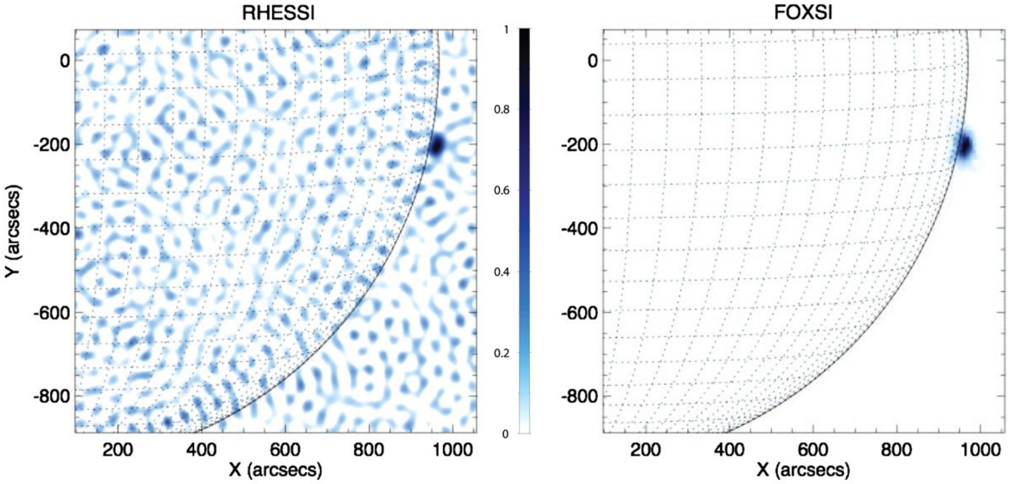

Figure 3.7: Hard X-ray images of a B2.7 flare during the first *FOXSI* flight on 2012 November 2. (Left) *RHESSI* image made using the CLEAN algorithm. Due to the indirect imaging there are significant sidelobes in the PSF which contribute noise throughout the reconstructed image FoV. (Right) *FOXSI* image with much better signal-to-noise ratio resulting from the use of focusing optics. Both images are shown for the *FOXSI* FoV, which is smaller than *RHESSI*'s. The same color scale is used in both panels. Figure from Krucker et al. (2013).

3.2.4 Science Results

During the *FOXSI-1* flight a B2.7 class microflare occurred on the west limb of the Sun. Figure 3.7 shows a comparison between the *FOXSI* and *RHESSI* images of this flare. This image makes the advantage of focusing optics immediately apparent. A full analysis of this flare is in progress (Glesener et al. 2017, in prep).

FOXSI-1 also pointed at a non-flaring active region, in coordination with *Hinode*/XRT and *Hinode*/EIS. Multiple XRT channels and EIS spectral lines were used to calculate a DEM distribution that hinted at the presence of hot plasma >8 MK. However, the predicted number of counts from this hot component was much higher than the number of counts seen by *FOXSI*, so it could be ruled out (Figure 3.8). This work (Ishikawa et al. 2014) shows how valuable HXR observations are for constraining the high-temperature tails of DEM distributions.

FOXSI-2 pointed at several active regions and the quiet Sun. Two microflares were detected in two different active regions (Glesener et al. 2016). While there were a handful of photons detected in the quiet Sun, they were consistent with ghost rays from sources outside the instrument FoV. These quiet Sun pointings were used to place limits on temperature and emission measure from a thermal plasma (Buitrago-Casas et al. 2015), similar to the *NuSTAR* analysis I describe in Chapter 4. One of the active regions seen by *FOXSI-2* shows evidence for plasma at T≈10 MK. I present a spectrum of this region and an analysis of the nanoflare properties that can produce this emission in Chapter 5; a full DEM analysis of this region with *FOXSI* and *Hinode* has been done by Ishikawa et al. (2017, in prep). *FOXSI* has shown the potential value of a solar-dedicated HXR observatory that uses focusing optics instead of indirect imaging. The *NuSTAR* satellite has also shown the value of using focusing optics for solar HXR observations.

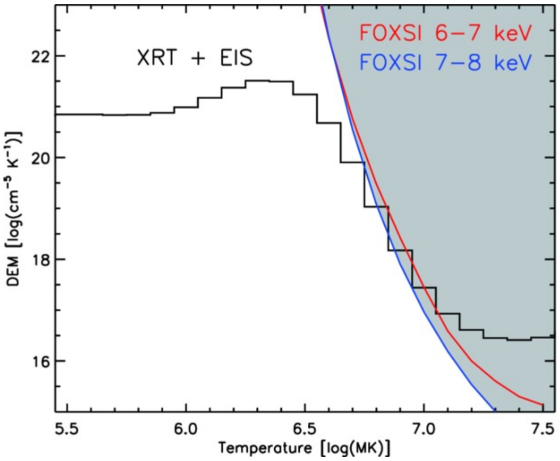

Figure 3.8: Differential emission measure of a nonflaring active region observed during the first *FOXSI* flight. The combination *Hinode*/XRT, *Hinode*/EIS, and *FOXSI* was used to calculate the DEM for $5.5 < \log(T) < 7.5$. *FOXSI* is able to set strong constraints on plasma at $T > 10$ MK that aren't possible with the EUV and SXR data alone. Figure from Ishikawa et al. (2014); note that the x-axis units should be Temperature [log(K)].

3.3 NuSTAR

(*NuSTAR*) is a NASA Small Explorer (SMEX) mission launched in June of 2012 (Harrison et al. 2013). *NuSTAR* is the first satellite mission with HXR focusing optics, which it uses to image ∼2–79 keV photons with a spatial resolution of 18" (FWHM) and a FoV of 12'×12'. The *NuSTAR* detectors are position-sensitive and can achieve an energy resolution of 0.4 keV (FWHM) at 10 keV and 0.6 keV at 60 keV. Two optics telescopes (FPMA and FPMB) are separated by a composite carbon mast of length ∼10 m from two detector arrays onto which they focus incident X-rays.(Figure 3.9). *NuSTAR* is in an equatorial orbit that results in alternating periods of day and night, with daylight observing periods between 40–60 minutes (depending on the SAA).

Satellite day and night cause expansion and contraction, respectively, of the *NuSTAR* mast. Therefore, *NuSTAR* utilizes a star tracker on the optics bench in conjunction with two laser metrology units. When combined, the tracker and lasers measure the relative translations and tilts between the two ends of the telescope. These data are applied on the ground to reconstruct the instrument alignment and pointing direction at any given time.

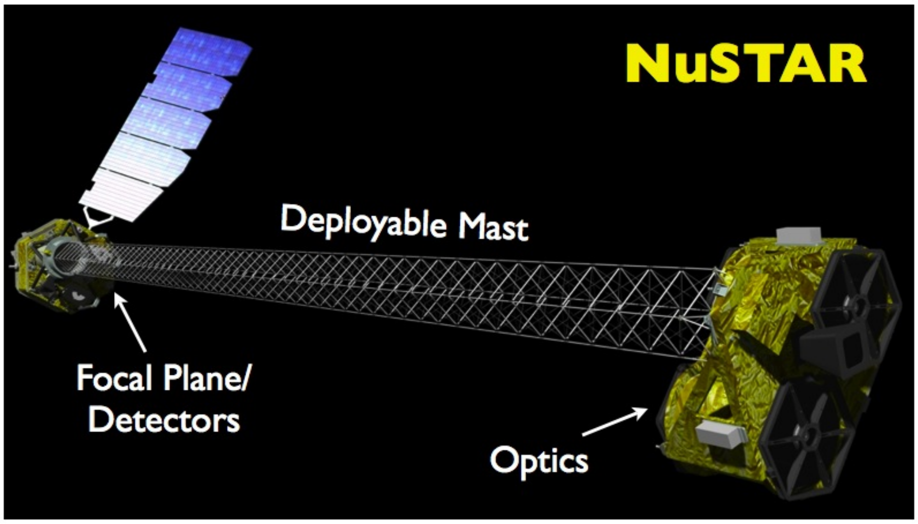

Figure 3.9: The *NuSTAR* HXR astrophysics satellite. The gray rectangular objects on the optics module are part of the laser metrology system. Image courtesy of NASA.

The *NuSTAR* satellite optics and detectors benefited greatly from technology development on the *High Energy Focusing Telescope (HEFT)*, a balloon experiment led by Caltech (Harrison et al. 2005). Detailed information on the *NuSTAR* satellite can be found in Bhalerao (2012), Harrison et al. (2013) and Madsen et al. (2015).

3.3.1 Optics

The *NuSTAR* optics (Figure 3.10) consist of two sets of depth-graded multilayer coated mirrors that form a conical approximation to Wolter-I optics. This approximation slightly degrades the on-axis PSF, but results in fewer artifacts from off-axis sources. Each module contains 133 nested shells with coatings specifically designed to maximize the instrument FoV and energy range. The individual shells are made of either 12 or 24 thin glass segments, depending on their radius. The outer 44 shells are coated with alternating layers of W/Si, and the inner 89 are coated with Pt/C. The inner shells, with smaller grazing angles, are optimized for higher energy photons.

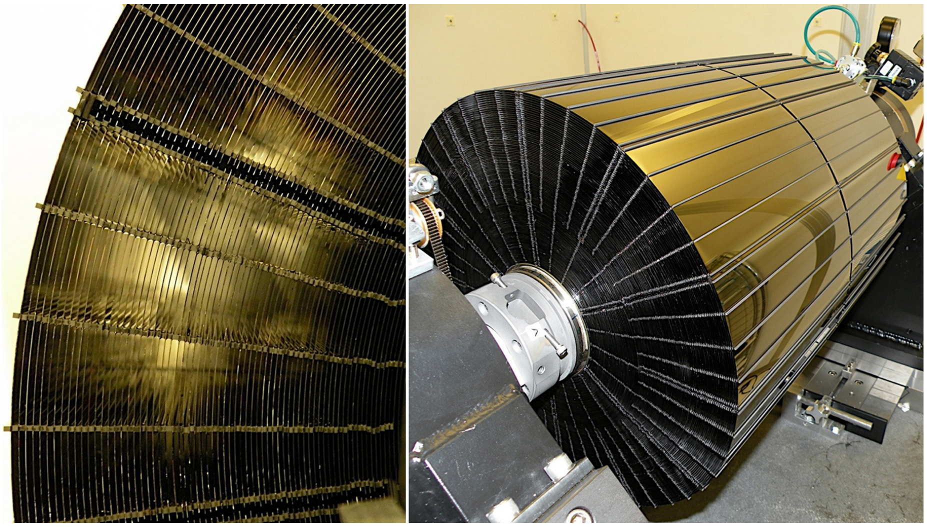

Figure 3.10: (Right) One of two *NuSTAR* optics on the assembly machine at Columbia University. (Left) Zoomed-in image of individual layers separated by graphite spacers. Image from the *NuSTAR* website (`http://www.nustar.caltech.edu/page/optics`.)

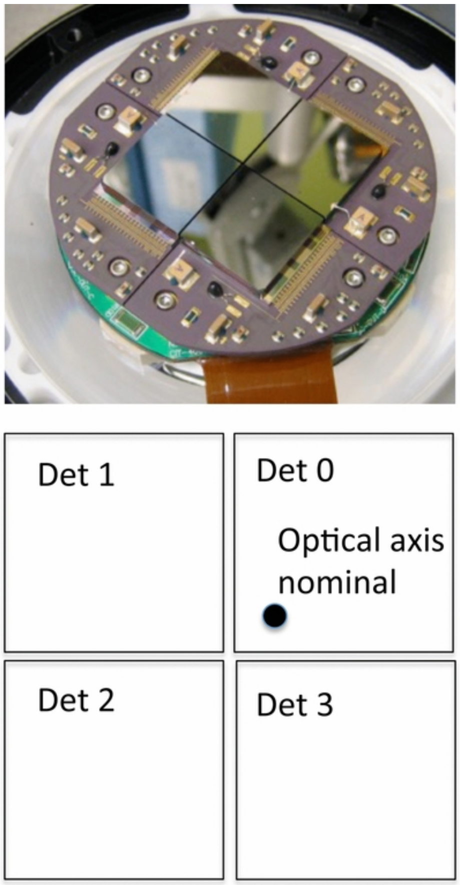

Figure 3.11: (Top) One of the *NuSTAR* detector plane modules comprising 4 pixellated CdZnTe detectors. (Bottom) Detector names and focal point for an on-axis source. Image from Harrison et al. (2013).

3.3.2 Detectors

NuSTAR has two detector planes, each containing a 2x2 array of pixellated CdZnTe detectors (Figure 3.11). CdZnTe absorbs nearly 100% of photons below 80 keV, the upper limit of *NuSTAR*'s energy range. In addition, these detectors have energy resolution on the order of a few percent and high quantum efficiency. A detailed description of the *NuSTAR* detector properties and calibration can be found in Bhalerao (2012).

Solar Observing and Limitations

Since *NuSTAR* was designed for astrophysical observation, high throughput was not a significant concern. Each *NuSTAR* telescope has a maximum count rate of 400 counts s^{-1} due to a non-paralyzable deadtime of 2.5ms. This deadtime occurs at the digital stage of event processing, so *NuSTAR* is actually able to observe at much higher incident count rates. Pileup can occur on ∼microsecond timescales, so incident rates above 10^5 counts s^{-1} can be problematic. In addition, *NuSTAR* will reject events if photons hit two different detectors within a coincidence window of 2–3 μs. Therefore, bright enough flares within the FoV can cause the instrument to shut down for extended periods (see Figure 3.13).

There was a significant amount of work done leading up to the *NuSTAR* launch and during its first two years in orbit to determine what it might see from the Sun and what the best observing conditions would be. Figure 3.12 shows one example of this, a simulated *NuSTAR* image of an active region generated by the *NuSIM* full-instrument simulator. The active region spectrum was derived from the *DEM* distribution in Warren et al. (2011), who observed one particular active region with multiple *Hinode*/EIS spectral lines across a wide range of temperatures. The predicted count rate from this region was found to be 4×10^4 counts s^{-1}, a hundred times higher than the maximum *NuSTAR* throughput. This rate is of the same order of magnitude as *NuSTAR*-observed active region fluxes (e.g. Hannah et al. 2016).

Ghost rays can be problematic for solar observations if there are bright sources on the disk (e.g. active regions). The *NuSTAR* FoV is ∼12'×12', or about a third of a solar diameter. Therefore, ghost rays can contribute a lot of background flux to quiet Sun regions, particularly if there are several active regions or a flare outside the FoV. An extreme example of this was encountered during the first *NuSTAR* solar pointing (Figure 3.13). This *NuSTAR* observation took place during the decay phase of an X-class flare that occurred near disk center, and the emission from that flare created bright ghost ray patterns in all the *NuSTAR* pointings used to make a mosaic image of the Sun. Even at higher livetimes, *NuSTAR* has not yet made a definitive detection of quiet Sun emission due to ghost ray background from active regions (see

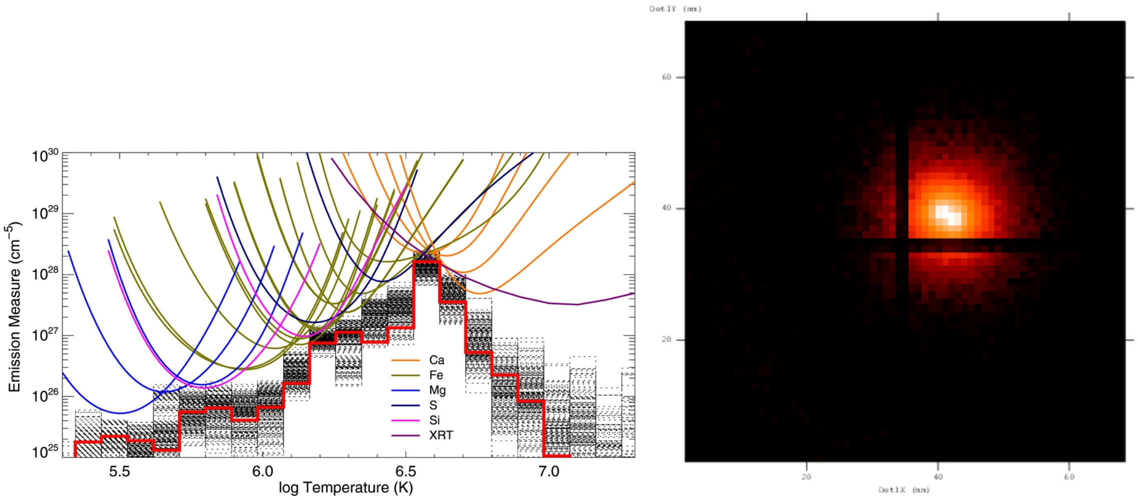

Figure 3.12: (Left) Active region *DEM* distribution from Warren et al. (2011). (Right) Simulated *NuSTAR* image of the Warren et al. (2011) active region in detector coordinates (mm). The gaps between the four detectors are clearly visible.

Chapter 4).

3.3.3 Science Goals and Results

The advantages of a focusing optics instrument like *NuSTAR* are high sensitivity and dynamic range. The science goals for *NuSTAR* solar pointings are similar to those of *FOXSI*, though *NuSTAR* has the advantages of higher effective area and longer pointing durations. The two main solar science topics that can be addressed with *NuSTAR* are particle acceleration and coronal heating.

NuSTAR has observed the Sun a total of 9 times, with the most recent observation on 2017 March 21. An overview of *NuSTAR* solar pointings through April 2015 is given in Grefenstette et al. (2016). There is also a web page with overview plots of every *NuSTAR* solar pointing to date[1]. Two additional papers have been published on the first set of observations. Kuhar et al. (2017) used *NuSTAR* to perform imaging and spectroscopy of an occulted active region on 2014 December 11, the day after a flare occurred in that same region. *NuSTAR* saw post-flare loops that could not be imaged by *RHESSI*. This paper concluded that multiple sets of post-flare loops

---

[1] `https://ianan.github.io/nsigh_all/`

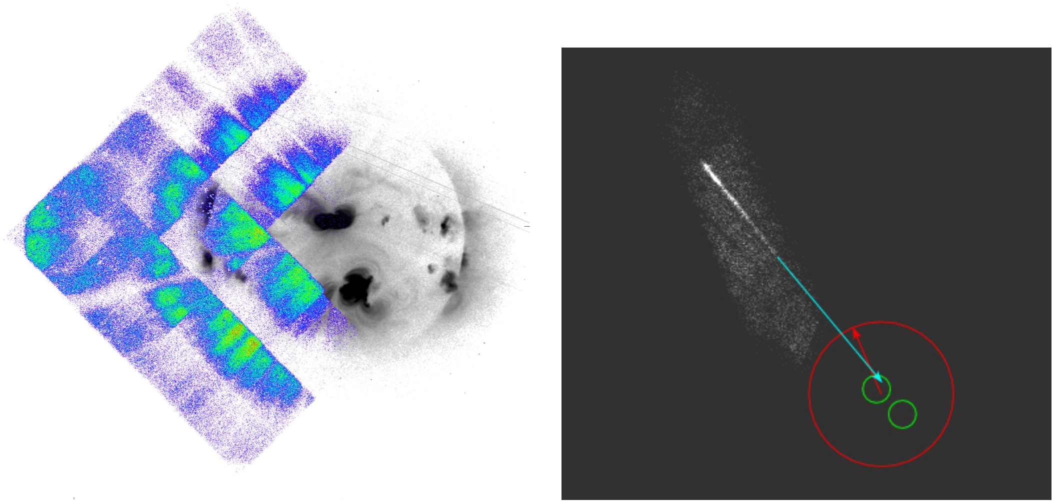

Figure 3.13: (Left) *NuSTAR* tiled images of the full Sun during its first solar pointing on 10 September 2014. An X-class flare had occurred near disk center before this observation began, resuling in high levels of X-ray flux. The center-right images are missing because the instrument FoV included the flaring region; this resulted in count rates so high that every *NuSTAR* event was rejected by on-board software. Image from Grefenstette et al. (2016). (Right) Integrated *NuSTAR* image from a slew away from the Sun during the same observation. The solar limb is marked by a red circle, and two bright active regions near disk center with green circles. The bright streak is a result of stray X-ray light (zero-bounce, not to be confused with single-bounce ghost rays) from the flaring active region hitting the detectors through an unbaffled part of the optics.

had formed and then cooled since the flare, giving a net energy release an order of magnitude higher than the energy at the flare peak. At least one other *NuSTAR* observation has shown the presence of a high coronal source that might be related to particle acceleration.

Hannah et al. (2016) performed imaging spectroscopy of five active regions seen on 2014 November 1. A separate analysis of these regions is presented in Chapter 5, and an analysis of a quiet region observed on this day is presented in Chapter 4. These regions were quiescent during the two *NuSTAR* orbits they were observed. *NuSTAR* images and co-spatial images from *SDO*/AIA can be seen in Figure 3.14. All of the active region spectra were well-fit by an isothermal spectrum, with no need for a second thermal or a non-thermal component (Figure 3.15). Hannah et al. (2016)

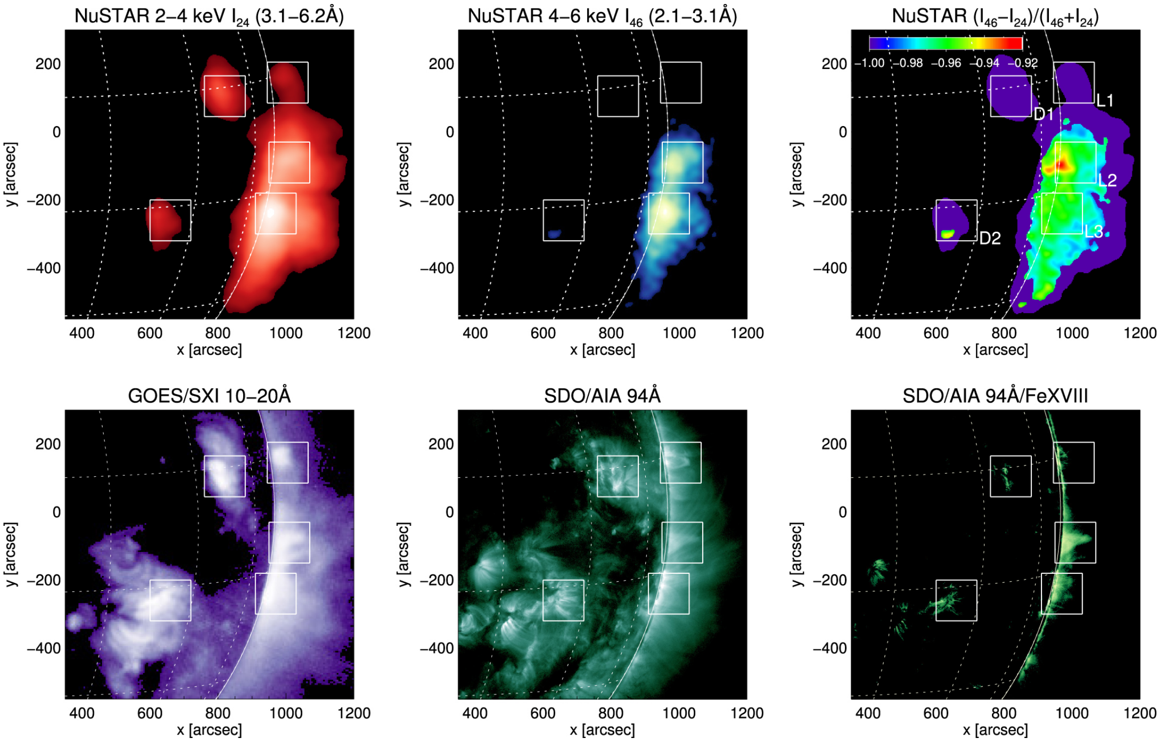

Figure 3.14: (Top) *NuSTAR* 2–4 and 4–6 keV HXR images of active regions near the limb on 2014 November 1, along with the differential hardness ratio. (Bottom) SXR and EUV images of the same regions from *GOES*/SXI, *SDO*/AIA 9 Å, and the Fe XVIII component of the 94 Å channel which isolates hotter plasma. White boxes indicate the regions used for subsequent spectral analysis. Figure from Hannah et al. (2016).

also placed upper limits on the emission measure of a second, higher-temperature component (possibly related to nanoflare heating) between 5 and 12 MK. These limits were broadly consistent with measurements by EUV and SXR instruments. Although the T and EM limits were lower than the detection by Brosius et al. (2014), it is possible that this was due to intrinsic differences between the observed regions. In fact, the five active regions in this study had high-temperature EM limits that varied by about an order of magnitude. It is worth noting that *NuSTAR* had very limited exposure times during this observation; approximately 3 s per orbit due to the low livetime (∼0.3%). Future observations of isolated active regions for extended periods are possible, and would allow deeper constraints on plasma at T>5 MK.

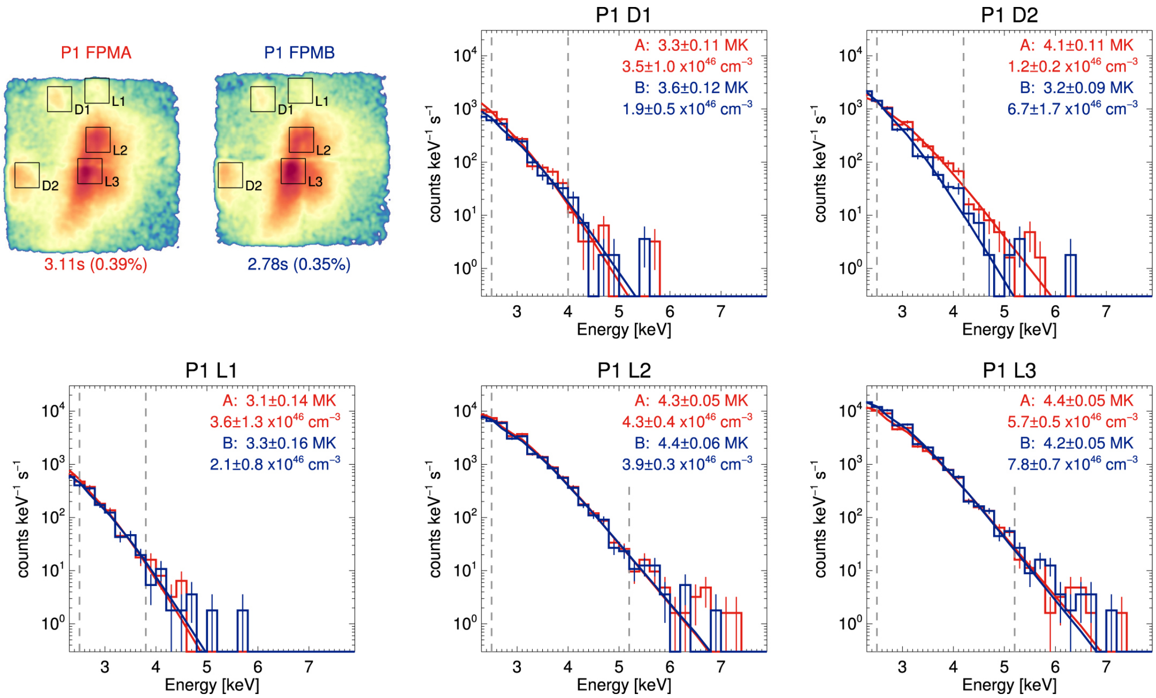

Figure 3.15: *NuSTAR* spectra and isothermal fits for active regions near the limb on 2014 November 1. Fits are done separately for the two telescope modules (FPMA & FPMB), which can disagree due to slightly different exposure times and pointing alignment. Integrated images from both modules are shown at top left, along with the exposure time and livetime for each. Figure from Hannah et al. (2016).

Additional papers on *NuSTAR* solar observations are in preparation. These include an imaging and spectroscopic analysis of a very small flare (Glesener et al. 2017, submitted) and a DEM analysis of another small flare with *NuSTAR*, *SDO*/AIA, and *Hinode*/XRT (Wright et al. 2017, submitted). Furthermore, *NuSTAR* quiet Sun pointings are being used to place upper limits on solar axion fluxes from the core of the Sun (Hudson et al. 2012). The most interesting science from *NuSTAR* may be still to come, as every observation to date has taken place with one or more active regions on the disk. It is still unclear if the quiet Sun emits HXRs from hot plasma or non-thermal particles (Hannah et al. 2010 and Chapter 4). As the Sun moves into solar minimum *NuSTAR* will observe a disk free of active regions, and possibly achieve the first detection of the quiet Sun in HXRs.

Chapter 4

First *NuSTAR* Limits on Quiet Sun Hard X-Ray Transient Events

Abstract

We present the first results of a search for transient hard X-ray (HXR) emission in the quiet solar corona with the *Nuclear Spectroscopic Telescope Array* (*NuSTAR*) satellite.[1] While *NuSTAR* was designed as an astrophysics mission, it can observe the Sun above 2 keV with unprecedented sensitivity due to its pioneering use of focusing optics. *NuSTAR* first observed quiet Sun regions on 2014 November 1, although out-of-view active regions contributed a notable amount of background in the form of single-bounce (unfocused) X-rays. We conducted a search for quiet Sun transient brightenings on time scales of 30, 60, and 100 s and set upper limits on emission in two energy bands. We express 2.5–4 keV limits as the temperature T and emission measure EM of a thermal plasma, and 10–20 keV limits as model-independent photon fluxes. The limits in both bands are well below previous HXR microflare detections, though not low enough to detect events of equivalent T and EM

---

[1] This chapter is the text of a paper that has been submitted to the Astrophysical Journal with the following authors: Andrew J. Marsh, David M. Smith, Lindsay Glesener, Iain G. Hannah, Brian W. Grefenstette, Amir Caspi, Säm Krucker, Hugh S. Hudson, Kristin K. Madsen, Stephen M. White, Matej Kuhar, Steven E. Boggs, Finn E. Christensen, William W. Craig, Charles J. Hailey, Fiona A. Harrison, Daniel Stern, and William W. Zhang.

as quiet Sun brightenings seen in previous soft X-ray observations. We expect future observations during solar minimum to increase the *NuSTAR* sensitivity by over two orders of magnitude due to higher instrument livetime and reduced background.

4.1 Introduction

Hard X-rays (HXRs) are an important probe of particle acceleration and heating in solar flares. High-temperature plasma emission (>1 MK) can be seen directly via thermal processes (bremsstrahlung, free-bound continua, and emission lines). Many flare observations also show non-thermal distributions above ∼10 keV; these spectra can be inverted to give information about the underlying electron spectra. In many flares the energy in accelerated electrons and ions is comparable to the total radiated energy at all wavelengths (Lin & Hudson 1976; Ramaty et al. 1995; Emslie et al. 2012). Therefore in order to fully understand the physical processes underlying solar flares, HXR measurements are necessary.

The *Reuven Ramaty High Energy Solar Spectroscopic Imager* (*RHESSI*) is the current dedicated solar HXR satellite (Lin et al. 2002). *RHESSI* can observe flares ranging in size from *GOES* A-class microflares to the largest X-class events, due to moveable shutters that reduce the measured flux above a certain count threshold. Hannah et al. (2008) and Christe et al. (2008) showed that even the smallest detectable *RHESSI* events have characteristics similar to larger flares: they occur in active regions, show thermal emission from loops, and show impulsive, non-thermal emission from footpoints. It is an open question whether HXR-emitting flares exist outside of active regions, as *RHESSI* is unable to measure flux from the quiet Sun due to limited sensitivity and dynamic range (Hannah et al. 2010).

Flares, or flare-like brightenings, contribute to the heating of the solar corona. Hudson (1991) showed that for a distribution of flare frequency versus energy, the smallest events dominate energetically if the power-law index >2. Observations show a power-law index close to 2, but an exact value is difficult to determine due to selection bias and the use of different instruments at different energies. While large flares do not provide enough energy to heat the corona (Hannah et al. 2011), it is possible that many small events might.

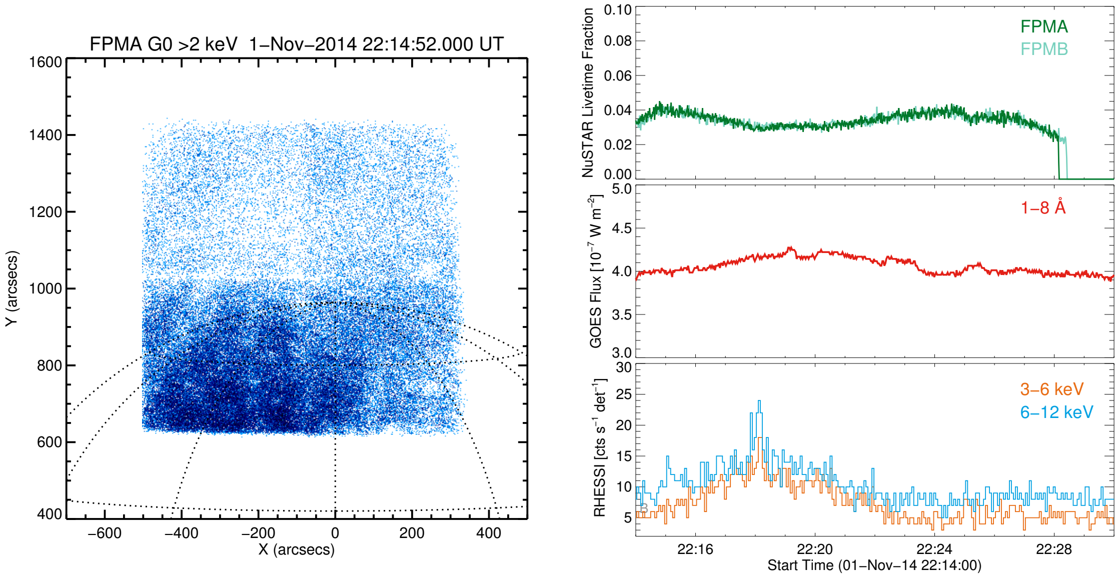

Figure 4.1: (Left) *NuSTAR* image >2 keV in the FPMA telescope integrated over the 2014 November 1 north pole pointing. The detected emission is consistent with ghost rays produced by active regions outside the instrument FoV. (Right) Time profiles of the *NuSTAR* livetime (top panel), the *GOES* 1–8 Å flux (middle panel), and the *RHESSI* 3–6 and 6–12 keV fluxes (bottom panel). The slow rise detected by *RHESSI* at 22:18 UT is solar in origin, but outside *NuSTAR*'s field of view.

Quiet-Sun transient brightenings (also referred to in the literature as heating events, network flares, or nanoflares) have been observed in multiple wavelengths including EUV and soft X-rays (Krucker et al. 1997; Parnell & Jupp 2000; Aschwanden et al. 2000). These brightenings have characteristic measured temperatures of 1–2 MK and derived energies of 10^{24}–10^{27} ergs. They release less energy, are shorter in duration, and occur much more frequently than X-ray bright points observed in the quiet Sun (Golub et al. 1974; Kariyappa et al. 2011). Krucker & Benz (2000) observed this type of event using spectral line data from the Extreme Ultraviolet Imaging Telescope (EIT, Delaboudinière et al. 1995) and the Coronal Diagnostic Spectrometer (CDS, Harrison et al. 1995) in addition to radio data from the Very Large Array (VLA). They concluded that quiet Sun heating events can be viewed as small flares, with similar temporal and spectral characteristics as larger events observed in active regions. The thermal components of such events may be difficult to detect with HXR instruments, due to the low temperatures. If enough non-thermal particles are present, these quiet Sun events could potentially be visible to HXR instruments more sensitive than *RHESSI*.

The *Nuclear Spectroscopic Telescope Array* (*NuSTAR*) uses focusing optics to directly image HXRs from ∼2 to 79 keV (Harrison et al. 2013). Though *NuSTAR* was designed as an astrophysics observatory, it can point at the Sun without any harm to the telescope optics and only a slight degradation in angular resolution (Grefenstette et al. 2016, hereafter G16). Here we perform the first search for transient, resolvable brightenings in quiet Sun regions observed by *NuSTAR*. We emphasize that these events are not the "nanoflares" referred to by modern theories of coronal heating (Klimchuk 2015), although *NuSTAR* can constrain the hot plasma they are predicted to produce (Hannah et al. 2016). We discuss the *NuSTAR* instrument and solar observing procedures in §4.2. Our analysis methods and results are described in §4.3, and additional discussion of these results is found in §4.4.

4.2 Solar Observing with *NuSTAR*

NuSTAR is a NASA Astrophysics Small Explorer (SMEX) satellite launched on June 13, 2012 (Harrison et al. 2013). It has two co-aligned X-ray optics focused onto two focal plane detectors (FPMA and FPMB) and observes the sky in the energy range ∼2 to 79 keV. The instrument field-of-view (FoV) is approximately $12' \times 12'$ and the half-power diameter is $\sim 60''$ (Madsen et al. 2015). *NuSTAR* is well calibrated over the 3–79 keV bandpass and the lower energy bound can be extended to as low as 2.5 keV if there is sufficient flux present (G16).

NuSTAR has been used to perform imaging spectroscopy on active regions (Hannah et al. 2016), to observe high-temperature loops after an occulted solar flare (Kuhar et al. 2017), and to characterize sub A-class flares (Glesener et al. 2017, Wright et al. 2017, both recently submitted). The combination of a large effective area and low background rate makes it orders of magnitude more sensitive than *RHESSI*. This increase in sensitivity allows it to probe previously inaccessible regimes in flare parameter space, both in active regions and in the quiet Sun. However, because it was not designed to look at the Sun there are several limitations to *NuSTAR*'s solar observing that must be considered during observation planning and data analysis.

1) *NuSTAR* has a relatively low throughput of 400 counts s^{-1} $\mathrm{telescope}^{-1}$, which is reasonable for cosmic sources but very small for the Sun. Fortunately, this throughput limit is related only to digital data handling, and we can obtain data with minimal pileup at incident count rates as high as $\sim 10^5$ counts s^{-1} (G16).

2) Single-bounce photons from outside the FoV, known as ghost rays, can contribute significant emission inside the FoV (Madsen et al. 2015). We have seen ghost ray patterns in several observations to date, and there is no easy way to remove this background.

3) The *NuSTAR* line-of-sight star tracker, or camera head unit (CHU), does not work during solar observing. There are three backup star trackers, all of which are oriented perpendicular to the instrument line of sight. As a result, offsets between the *NuSTAR* nominal and actual pointing can be ~1–2 arcminutes (G16). We must rely on direct comparisons with solar-dedicated imaging instruments such as *SDO*/AIA to accurately calibrate our pointing. This is only possible when bright sources (e.g. active regions) appear in the *NuSTAR* FoV, and offsets are generally different for different CHU combinations.

A full discussion of instrumental limitations and a summary of *NuSTAR* solar observations through April 2015 can be found in G16.

4.3 Analysis and Results

4.3.1 Data reduction

The data presented in this paper are from the fourth orbit of the second *NuSTAR* solar campaign, which took place on 2014 November 1. This orbit included two quiet Sun pointings and the lowest solar flux levels of this campaign (full Sun *GOES* class ~B4). We analyzed data from the second quiet Sun pointing (aimed at the north pole) due to a reduced ghost ray background. The active regions observed during the

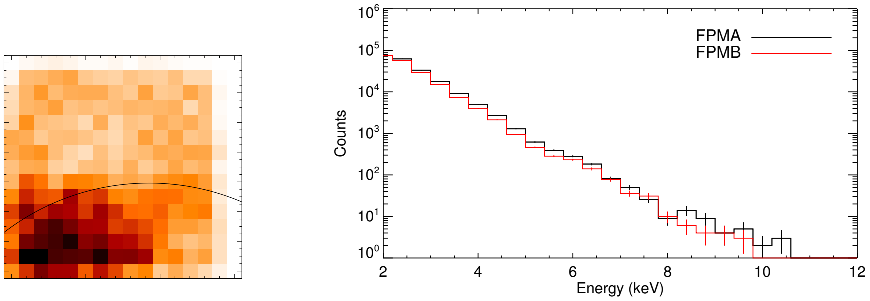

Figure 4.2: (Left) Single frame of a $NuSTAR$ FPMA image cube, with the solar limb overlaid in black. Spatial binning is $60'' \times 60''$ and temporal binning is 100 seconds. (Right) $NuSTAR$ count spectra from both telescopes, integrated over the full north pole pointing and the full FoV. Error bars shown are the square root of the number of counts in each bin. Most or all of the photons in both panels are due to ghost rays from active regions outside the FoV.

first two pointings in this orbit are analyzed in Hannah et al. (2016).

Event files were generated and processed using the $NuSTAR$ Data Analysis software v1.4.1 and $NuSTAR$ calibration database 20150414. We utilized a modified analysis pipeline for solar data, as the standard pipeline throws out a large fraction of real events (G16). The $NuSTAR$ event files were translated into heliocentric coordinates using the JPL Horizons[1] database of solar RA/DEC positions. Non-physical events (e.g. events with zero energy, uncalibrated position, or in hot pixels) were thrown out.

Figure 4.1 shows $NuSTAR$ counts >2 keV in the FPMA telescope integrated over the full north pole pointing. There are more counts on disk than off disk, but we were unable to unambiguously distinguish the solar limb. Simulations with the full-instrument simulator $NuSIM$ (Madsen et al. 2011) showed that the observed emission is consistent with ghost rays produced by active regions near Sun center, outside the instrument FoV. We therefore cannot claim a definitive detection of HXR emission from the quiet Sun. There are ∼14 minutes of data between the times $NuSTAR$ entered sunlight and entered the South Atlantic Anomaly (seen as a livetime dropout at ∼22:28 UT in Fig. 4.1). Though the Sun was mostly quiet during this pointing, a

---

[1] http://ssd.jpl.nasa.gov/horizons.cgi

small microflare occurred near disk center at ~22:18 UT and is visible in the *RHESSI* light-curve. Ghost rays from this event are correlated with a decrease in livetime, but the effect is no larger than variations during non-flaring periods.

We used *SDO*/AIA data to calibrate the *NuSTAR* pointing alignment. All of the data for the north pole pointing were taken in CHU combination 1+3. Fortunately, the same CHU combination was used in a previous orbit during active region observations. We used active region pointings in consecutive orbits to verify that the offsets of different CHU states stayed approximately the same from orbit to orbit. A shift of (x-105″, y+65″) applied to the *NuSTAR* images gave the best match to active region positions measured in CHU-state 1+3.

We generated 3-D image cubes by binning the *NuSTAR* event files in space and time. Figure 4.2 shows a single frame of the FPMA image cube, with the solar limb overlaid in black and binning of 100s and 60″×60″. This image includes the pointing correction derived from *SDO*/AIA data. This figure also shows the integrated count spectrum in both telescopes for the north pole pointing. *NuSTAR* does not see any counts >11 keV, though we can set flux limits at lower and higher energies. Our particular choices of spatial and temporal bins are discussed later.

4.3.2 Adding the telescopes

NuSTAR has two focal planes (FPMA & FPMB) with a throughput limit of 400 counts s^{-1} in each. Although the telescopes are read out separately, the data for both can be combined with care. This is desirable because if there is a real signal anywhere in our time series, doubling the signal and background by adding the telescopes will gain us a factor of $\sqrt{2}$ in the signal-to-noise ratio. However, we can only add the telescopes if their spatial differences are negligible. Because of the spacecraft geometry, the ghost ray patterns can be different in each telescope for the same FoV. In extreme cases the sensitivity in a particular region can be much better in one telescope than in the other, as the result of a reduced ghost ray background.

For a given spatial pixel at a given time, if the ratio of the higher number of counts to the lower number of counts in each telescope is >3 the gain in signal-to-noise ratio

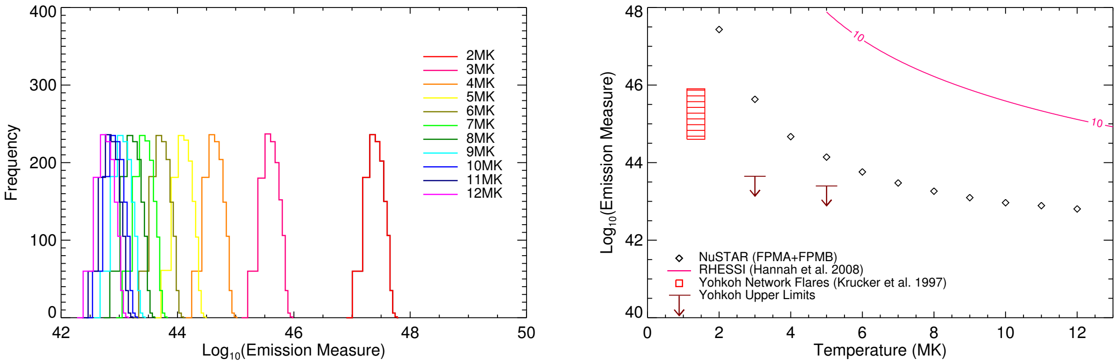

Figure 4.3: (Left) The "just detectable" emission measure distributions for temperatures 2–12 MK, calculated for summed (FPMA+FPMB) north pole image cubes. These distributions include every macropixel from two image cubes: one with no time shift and one with a half-bin time shift. The "just detectable" limit corresponds to the intensity that gives a count excess above background at the 95% confidence level. (Right) The *NuSTAR* sensitivity for this observation with t_{bin} = 100s and $s_{bin} = 60'' \times 60''$. The black diamonds correspond to the peaks of the EM distributions in the left plot. The pink contour is the level at which *RHESSI* would detect 10 cts s^{-1} detector^{-1}, approximately the instrument limit for imaging and spectroscopy. The soft X-ray transient brightenings observed by *Yohkoh*/SXT in Krucker et al. (1997) are shown as a red striped box; these events are below the sensitivity limit for this observation. *Yohkoh*/SXT upper limits on higher-temperature network flares are shown as brown arrows.

is negated by adding a quiet pixel to a noisy one. However, if there are fewer than 10 combined counts in a given spatial pixel, there is a large uncertainty in the counts ratio. Therefore, we used the sum of both telescopes for every pixel *unless* both of these conditions were met: the number of summed counts >10 and the ratio of the higher number of counts to the lower number of counts is >3. For summed pixels we use the average of the two telescope livetimes.

4.3.3 Transient Search

We used Poisson statistics to determine the probability of getting S or more counts in a particular macropixel given a background B. This tests the null hypothesis that S is from background alone in the absence of any signal. We calculated the background by averaging counts in the same spatial macropixel in adjacent temporal frames, accounting for changes in livetime. If a frame was the first or last of the image cube, then we used the single temporally adjacent macropixel as the background. The one and two frame background equations, respectively, are as follows:

$$B = L_t \frac{N_{t\pm1}}{L_{t\pm1}} \tag{4.1}$$

$$B = \frac{1}{2} L_t \left(\frac{N_{t-1}}{L_{t-1}} + \frac{N_{t+1}}{L_{t+1}} \right) \tag{4.2}$$

where N_t and L_t are the number of counts and the livetime, respectively, in the t^{th} frame. Since we do not know λ (the true background rate of which B is a sample) a priori, we generated databases of cumulative Poisson probabilities for a wide range of "source" and "background" counts and for 1 and 2 background frames. Given S source counts in the pixel of interest and an average background B, we computed the cumulative Poisson probability $P_{\geq}(S)|_B$ as follows.

First we generated a large number of trials for source (S) and background (B) counts using a Poisson distribution with average value λ. For the low energy (2.5 to 4 keV) image cube we used a range of 0.5 to 1200 for λ, with a spacing of 0.5. This range was chosen to include values of λ up to 2.5 times the maximum value in a single image cube pixel. We then created a 3-D array with each pixel equal to the number of occurrences of $[B,S,\lambda]$. Then we summed over the third dimension of this array to marginalize λ. The rows of the resulting 2-D array were normalized so that each had unit sum. This set the probability of getting any value of S for a particular value of B to 1 (as it should be). The last step was to integrate all probabilities $\geq S$ for each location $[B,S]$ in the databases, setting them equal to the probability of getting S or more counts for a given B.

After we generated the Poisson databases, we calculated the cumulative probability $P_{\geq}(S)|_B$ for every pixel in every time frame of the binned, combined image cube. We chose to set the detection threshold at the 95% confidence level, taking into account the number of trials. For example, for an image cube with 1,000 spatiotemporal pixels the probability threshold would be set at $0.05/1000 = 5\times10^{-5}$. We analyzed only pixels with their center on the solar disk, and performed the calculations on two image cubes with different time bins: the default bins and the default bins shifted half a bin forward in time. The purpose of the temporal shift was to increase the sensitivity to events that occurred on or near the default bin edges. Time bins with only partial data coverage were thrown out.

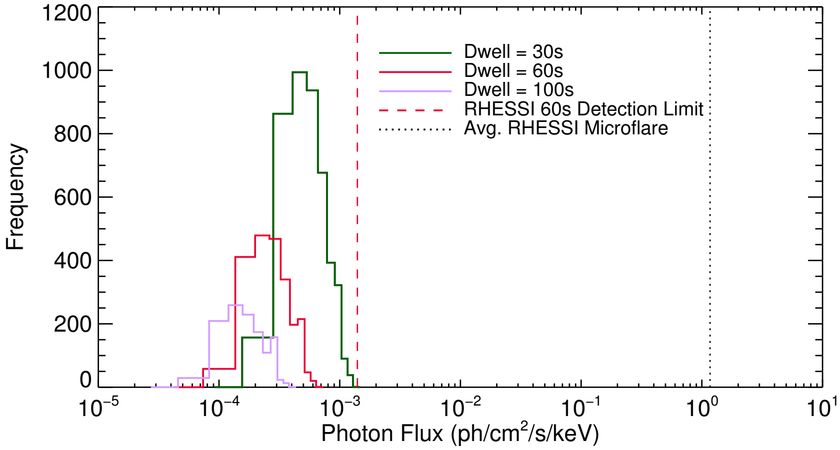

Figure 4.4: *NuSTAR* limits on 10–20 keV photon flux for this observation, calculated for the sum of FPMA & FPMB and three different temporal binnings (dwells). Each distribution includes every macropixel from two image cubes: one with no time shift and one with a half-bin time shift. The dashed line is the *RHESSI* detection limit at 10 keV. The dotted line is the average *RHESSI* microflare flux at 10 keV from Hannah et al. (2008).

We conducted a transient search over the full *NuSTAR* energy range and over a low energy band of 2.5–4 keV. With a 100 second integration time (dwell) and $60'' \times 60''$ macropixels there were 210 spatial pixels and 7 time bins, for a total of 1470 spatiotemporal pixels. Therefore the probability threshold was $0.05/1470/2 = 1.7 \times 10^{-5}$. The extra factor of 2 is a conservative way to account for the half-bin temporal shift (conservative because the shifted pixels are not totally independent of the un-shifted pixels, so the exact correction factor for the number of trials would be <2). The lowest probability event in any pixel is $P_{\geq}(S)|_B \sim 10^{-4}$, an order of magnitude above the threshold. Therefore we have no evidence of transient brightenings in the quiet Sun on time scales of 100 s. Fortunately, we can use the *NuSTAR* data to place upper limits on transient events in different energy ranges.

4.3.4 Low Energy (Thermal) Limits

We chose an energy range 2.5–4 keV to set limits on thermal emission. In this range the *NuSTAR* instrument response is well understood and there were a relatively large number of counts. We chose initial spatial and temporal binnings for the transient search of $60'' \times 60''$ and 100 seconds. The spatial binning is approximately the instrument half-power diameter (within which half the flux of a point source is expected to fall). The temporal binning is a duration that should be longer than an appreciable fraction of faint, transient HXR events. The average duration of a sample of microflares seen by *RHESSI* is ∼6 minutes, and the shortest events in that sample are ∼1 minute long (Christe et al. 2008). We expect *NuSTAR* to be sensitive to events at least an order of magnitude fainter than those seen by *RHESSI*, with correspondingly shorter durations; see e.g. Veronig et al. (2002) for the correlation of flare duration with X-ray flux.

We generated thermal bremsstrahlung spectra with temperatures 2–12 MK using the `f_vth.pro` function in Solarsoft (Freeland & Handy 1998). Next we converted the spectra from photons to counts using the *NuSTAR* instrument response and correcting for livetime. We calculated the number of counts required to meet the probability threshold for each temperature, based on the background level of each macropixel. We again performed the half-bin forward time shift, and accumulated statistics over the two separate image cubes. Each image cube was a combination of FPMA and FPMB determined by the critera in §4.3.2.

The *NuSTAR* detectors are subject to vignetting as a function of off-axis angle (Madsen et al. 2015). We used instrument vignetting curves from the *NuSTAR* calibration database to adjust the count thresholds. For each $60'' \times 60''$ macropixel, the average off-axis angle of every event was calculated and the vignetting curve function for the closest tabulated angle (averaged over the energy range 2.5–4 keV) was used as a correction factor.

After we applied the vignetting corrections to the count detection thresholds in each macropixel, we divided the counts by the temperature response for several isothermal temperatures. In this way we obtained the emission measures of isother-

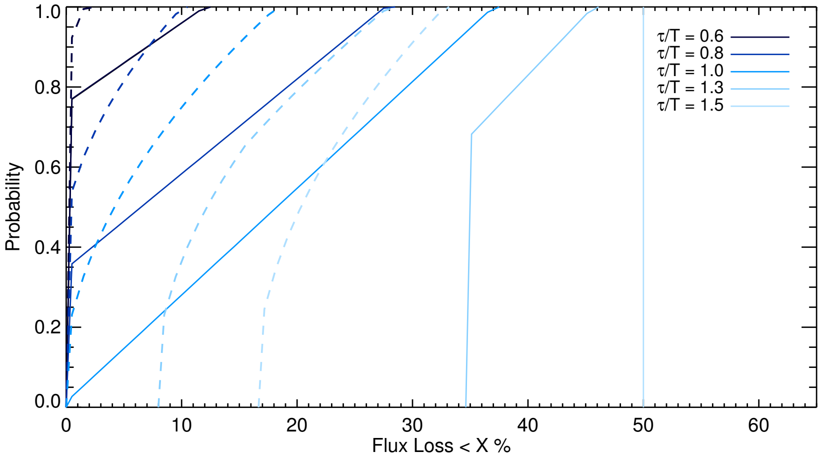

Figure 4.5: Cumulative probability distributions of flux loss for several different values of flare duration divided by bin width. For values of $\tau/T < 0.5$ there is no flux loss in the best time bin, which we select for every trial. For $\tau/T = 1.5$ the probability curve is a delta function; the flux loss is exactly 50% for every start time and every bin. Results are shown for a top-hat profile (solid lines) and a triangular profile (dashed lines).

mal spectra for every detection threshold. The left panel of Figure 4.3 shows the distribution of emission measures at the detection threshold for isothermal temperatures between 2 and 12 MK. The right panel of Figure 4.3 shows the *NuSTAR* T and EM sensitivity curve from 2 to 12 MK. Each black diamond corresponds to the peak of the distribution of EM upper limits for a particular temperature. Plotted in pink is the *RHESSI* 10 counts s^{-1} detector^{-1} contour; this is approximately the lowest count rate at which *RHESSI* can perform imaging and spectroscopy. *NuSTAR* is sensitive to events 2–4 orders of magnitude smaller than the smallest microflares seen by *RHESSI*. The T and EM range of quiet Sun network flares seen by *Yohkoh*/SXT is shown by a red box (Krucker et al. 1997). We also calculated *Yohkoh*/SXT upper limits on hotter network flares with temperatures of 3 and 5 MK (maroon arrows). While *NuSTAR* was not sensitive enough during this observation to detect quiet Sun brightenings similar to those observed by *Yohkoh*/SXT, future observations with higher livetime will bring us closer to that part of parameter space.

4.3.5 High Energy Limits

Important physical mechanisms such as impulsive heating and particle acceleration can be constrained by the presence (or absence) of nonthermal emission at energies >10 keV. Therefore, we calculated 10 to 20 keV photon flux limits based on the *NuSTAR* quiet Sun observations. We used a procedure similar to the one used to calculate the low energy limits, modified to account for the low statistics present in this energy range. *NuSTAR* saw a total of 15 counts between 10 and 20 keV in 801 seconds of north pole observing time, but no more than one count in any $60'' \times 60''$, 100 s macro-pixel (i.e. no clear transient signal). We combined the image cubes from both telescopes using the criteria in §3.2. Because the number of counts is so small, we could strongly constrain the true background count rate λ. We set a conservative upper limit on λ of two times the average number of counts per macropixel in the on-disk portion of the image cube. We consider this conservative because in this energy range the background is dominated not by ghost rays, which have a lot of spatial structure, but by the relatively uniform instrumental background. The results are, in fact, very sensitive to the range of λ since the values of λ near the cutoff dominate the marginalized probability when $B = 0$ (as it usually was for this analysis). We calculated cumulative probabilities, summed over this limited range of λ, to determine the number of counts required to reach the 95% confidence level. We then converted from counts to photons using the *NuSTAR* effective area, livetime correction, and vignetting coefficients. We used the effective area at 10 keV for two reasons. First, while these limits are model-independent most microflare nonthermal spectra are steeply falling. In addition, *NuSTAR*'s effective area varies little between 10 keV and 20 keV.

Figure 4.4 shows the *NuSTAR* flux limits from 10 to 20 keV for time scales of 30, 60, and 100 s. On the same graph are the average *RHESSI* microflare flux (Hannah et al. 2008) at 10 keV and the *RHESSI* 60 second detection limit in this energy range. For the latter we assume a 10–20 keV background of 1 count s^{-1} detector^{-1} and 9 live detectors, then calculate the incident flux necessary for a 95% confidence detection. While this is a useful comparison, lower-energy bands are better for source detection with both instruments due to higher flux. In this energy range *NuSTAR* is sensitive to transient events several times smaller than the *RHESSI* detection threshold.

4.4 Discussion

4.4.1 Event Duration and Flux Loss

For the transient search (§4.3.3), we searched consecutive time intervals and also the same set of intervals shifted ahead by half the interval duration, to ensure that we captured as much signal as possible for a random brightening. However, for event durations τ that are an appreciable fraction of a time bin width T, there will be flux loss even in the bin that contains most of the event. Flux loss means that some fraction of counts from a transient event falls outside the time bin of interest. This results not only in flux being lost, but also subtracted from the remaining flux as well, since it spills over into a time interval being used for background subtraction. The amount of flux lost depends on the event duration, which can be conveniently expressed as a fraction of the bin length (τ/T), and on the (arbitrary) start time of the transient relative to the time bin edges.

To quantify the average flux loss for a particular value of τ/T, we performed Monte Carlo simulations with a series of time bins and randomly injected transient events. For each event we examined both unshifted and shifted time bins and selected the bin with the least amount of flux lost. Then we generate a flux loss probability distribution based on a large number of simulations. Figure 4.5 shows the cumulative distribution of the amount of flux loss for two flare shapes (top hat and triangle) for a range of flare durations (expressed as a fraction of the bin duration).

A triangular profile results in lower flux losses than a top hat profile of the same duration, as expected. At τ/T=1.5, exactly half the flux is lost for a top hat flare at any start time and the loss curve is a delta function. For a more realistic triangular flare, the maximum flux loss is about 33 percent for the longest duration flares (τ/T=1.5). We did not analyze values of $\tau/T>1.5$, as events that long would have to be extremely bright to be detected by the search algorithm. For events shorter than a time bin, the more realistic triangular flares exhibit <15 percent flux losses. We do not expect this amount of loss to have a significant affect on our results; detailed simulations of the effects on transient sensitivity will be discussed in a future paper.

4.4.2 Coronal Heating

The nanoflare heating model invokes the occurrence of many independent heating events in the magnetic field all over the Sun's surface (Parker 1988; Cargill 1994; Klimchuk 2006). Although the energy release mechanism in most nanoflare models is indeterminate, they are generally predicted to heat coronal plasma to temperatures >5 MK. This emission has been called the "smoking gun" of the nanoflare heating theory; unfortunately it is difficult to observe (Klimchuk 2015). Brosius et al. (2014) recently claimed the detection of plasma at T≈9 MK in over 60% of an active region observed with the Extreme Ultraviolet Normal Incidence Spectrograph (EUNIS). Indirect evidence for nanoflare heating in active regions and the quiet Sun has been seen by the *Solar Dynamic Observatory's* Atmospheric Imaging Assembly *SDO*/AIA using a time-lag analysis of different channels(Viall & Klimchuk 2012, 2015a). Work is currently underway to determine what time-lags between simulated nanoflares give the best fits to *NuSTAR* active region data (Marsh et al. 2017, in prep). Unfortunately the 2014 November 1 data only show evidence of plasma <5 MK during quiescent times (Hannah et al. 2016), but it's possible that longer *NuSTAR* observations of quiescent active regions or the quiet Sun may be sensitive enough to detect hotter, fainter plasmas.

4.4.3 Future Observations

Due to low livetime (an average of 3.4% during this observation) and higher energy coverage, *NuSTAR* was not sensitive enough at low temperatures to detect brightenings in the range of emission measures seen by *Yohkoh*/SXT. However, the gain in sensitivity at higher energies was significant compared to previous HXR observations. In addition, we expect the sensitivity to increase by over two orders of magnitude in future observations due to decreasing solar activity. This increase will result from two factors: higher livetime due to lower incident count rates, and a decrease in the background count rate from the maximum throughput level to as low as the level of the quiet corona. For this observation the average incident 2.5–4 keV background rate is $\sim$16 counts s^{-1} arcmin^{-2} telescope^{-1}. In comparison, the estimated incident rate for the quiet corona (spectrum from Peres et al. 2000) is $\sim$0.15 counts s^{-1} arcmin^{-2} telescope^{-1} in this energy range. The advantage is even larger above 4 keV; the Peres et al. spectrum gives an expected count rate nearly $\sim$4 orders of magnitude smaller than seen in this observation. It is clear that when the Sun is at minimum activity levels, *NuSTAR* will give us an unprecedented view of the disk in HXRs.

Chapter 5

Hard X-Ray Constraints on Small-Scale Coronal Heating Events

Abstract

A large body of evidence suggests that the solar corona is heated impulsively.[1] Small-scale heating events known as "nanoflares" may be ubiquitous in quiet and active regions (ARs) of the Sun. Hard X-ray (HXR) observations with unprecedented sensitivity >3 keV have recently been enabled by focusing optics. We analyzed active region spectra from the *FOXSI-2* sounding rocket and the *NuSTAR* satellite to constrain the physical properties of nanoflares simulated with the EBTEL field-line-averaged hydrodynamics code. We modeled X-ray spectra by computing differential emission measures (DEMs) for various nanoflare heating amplitudes, durations, delay times, and filling factors. Additional constraints on the nanoflare parameter space were determined from physical arguments and from EUV/SXR data. For trains of

---

[1] This chapter is the text of a paper that will be submitted to the Astrophysical Journal with the following authors: Andrew J. Marsh, David M. Smith, Lindsay Glesener, James A. Klimchuk, Stephen J. Bradshaw, Juliana Vievering, Iain G. Hannah, Shin-nosuke Ishikawa, Säm Krucker, and Steven Christe.

homogeneous nanoflares, the *FOXSI*-observed region is well fit by nanoflares with heating amplitudes >0.02 erg cm^{-3} s^{-1} and a wide range of delay times and durations. The best fits for this region occur when the delay time is longer than ∼1700 s. The *NuSTAR*-observed regions are not fit as well by the homogeneous nanoflare model, and the good-fit regions of parameter space are fairly different. Three of the *NuSTAR*-observed regions are fit by smaller heating amplitudes <0.02-0.04 erg cm^{-3} s^{-1} and shorter delay times, and the other two regions are not well-fit at all. Additional studies of active regions observed by HXR instruments are needed to determine if similar nanoflare distributions can provide good fits to a range of ARs.

5.1 Introduction

It has been known for about 70 years that the solar corona is significantly hotter than the solar photosphere. However, a complete explanation of this temperature difference has been difficult to achieve. While much progress has been made in recent years, it is still unclear what the energetic contributions of different physical mechanisms (e.g. waves, reconnection, spicules) are. For recent reviews of the coronal heating problem see Klimchuk (2015) and Parnell & De Moortel (2012).

A large amount of evidence suggests that the corona is heated impulsively via small-scale heating events. Parker (1988) first envisioned "nanoflares" as magnetic reconnection between individual flux tubes that led to subsequent heating and particle acceleration. The term is now used to describe impulsive heating events on individual flux tubes without any preference for physical mechanism. For example, waves can produce nanoflares (Klimchuk 2006). The unifying prediction of nanoflare (impulsive heating) theories is the production of hot (≥5 MK) plasma throughout the solar corona. However, emission at these temperatures is difficult to detect. This is because only small amounts of this plasma are present and because ionization non-equilibrium effects may prevent the formation of spectral lines that would form at those high temperatures under equilibrium conditions (Golub et al. 1989; Bradshaw & Cargill 2006; Reale & Orlando 2008; Bradshaw & Klimchuk 2011).

The physical properties of nanoflares include their volumetric heating amplitude

H_0, duration τ, and delay time between events t_N. Field-aligned and field-averaged hydrodynamic simulations have been used to predict emission measure distributions $EM(T) = \int n^2 dh$ produced by nanoflares with a wide range of physical properties (Cargill 2014; Barnes et al. 2016a,b). A significant amount of discussion in the literature revolves around the frequency of heating and how it compares to the characteristic cooling time t_{cool} of a particular loop strand (length-dependent, but generally on the order of 1000 s). The regime of "high-frequency" heating is $t_N << t_{cool}$, while low-frequency heating occurs for $t_N >> t_{cool}$. Steady heating is simply the limit as t_N approaches 0. Cargill (2014) and Cargill et al. (2015) reported that nanoflare trains with delay times of hundreds to ~2000 s ($t_N \sim t_{cool}$) give results that are most consistent with observations. In addition, they found that delay times proportional to the total nanoflare energy are required to match the broad range of EM slopes found in active region observations. Time-lag plots of active regions observed at multiple wavelengths (e.g. Viall & Klimchuk 2012, Viall & Klimchuk 2017, ApJ, in press) can also constrain t_N. Bradshaw & Viall (2016) created model active regions heated by nanoflares and showed that the best agreement with observations occurs for delay times on the order of a cooling time.

Active region cores have been analyzed (e.g. Tripathi et al. 2011; Warren et al. 2012; Schmelz & Pathak 2012) with extreme ultraviolet (EUV) and soft X-ray (SXR) instruments including the *Solar Dynamics Observatory's* Atmospheric Imaging Assembly (*SDO*/AIA, Lemen et al. 2012), the *Hinode* X-Ray Telescope (XRT, Golub et al. 2007) and the *Hinode* EUV Imaging Spectrometer (EIS, Culhane et al. 2007). Observations generally show these instruments can strongly constrain emission below several MK, but lack sensitivity at higher temperatures. The most definitive detection of hot plasma to date came from the EUNIS sounding rocket, which observed the Fe XIX 592 Å line (peak formation temperature T $\approx$ 8.9 MK) in more than 60% of an active region (Brosius et al. 2014).

Hard X-ray (HXR) instruments can be used to detect or constrain plasma at temperatures $\gtrsim$5 MK. HXR emission is not sensitive to ionization equilibrium effects, which could make it easier to observe high-temperature plasma. However, this plasma can still be difficult to detect due to a temperature that peaks well before the luminosity (emission measure). Long duration, spatially-integrated observations from the *Reuven Ramaty High Energy Solar Spectroscopic Imager* (*RHESSI*, Lin et al. 2002) and *Solar PHotometer IN X-rays* (*SphinX*, Sylwester et al. 2008) both showed evidence of plasma at T>5 MK (McTiernan 2009; Miceli et al. 2012). Sounding rocket observations from an X-ray spectrometer also showed evidence for high-temperature plasma (Caspi et al. 2015). The combination of the *Hinode* X-Ray Telescope (XRT, Golub et al. 2007) and *RHESSI* was used to set constraints on a high-temperature component in active regions by Reale et al. (2009) and Schmelz et al. (2009). Large uncertainties in these analyses prevented a definitive detection: *RHESSI* has a better response to high-temperature plasma than *Hinode*, but lacks the sensitivity to reliably obtain images and spectra from non-flaring active regions.

Improved sensitivity and dynamic range can be obtained at energies above ∼3 keV by the use of focusing optics. This technology has enabled direct imaging of HXR photons in place of indirect images obtained by previous instruments. The *Focusing Optics X-ray Solar Imager (FOXSI)* sounding rocket payload uses focusing optics to image the Sun with much higher sensitivity and dynamic range than *RHESSI* (Glesener et al. 2016). *FOXSI* has flown twice (in 2012 and 2014) and is expected to fly again in 2018. The *Nuclear Spectroscopic Telescope Array (NuSTAR)* is a NASA Astrophysics Small Explorer (SMEX) satellite launched on 2012 June 13 (Harrison et al. 2013). While it was not designed to observe the Sun, *NuSTAR* has successfully done so on nine occasions without any damage to the instrument (for a summary of the first four solar pointings see Grefenstette et al. 2016). Both *FOXSI* and *NuSTAR* have been used to perform imaging and spectroscopy of active regions and to search for hot plasma (Ishikawa et al. 2014; Hannah et al. 2016).

In this chapter we use active region observations from *NuSTAR* and *FOXSI-2* to constrain the physical properties of nanoflares, particularly their heating amplitude, event duration, and characteristic delay time. We describe solar observations with these instruments in §5.2, detail our analysis methods in §5.3, and discuss our results in §5.4. Our conclusions and future work are described in §5.5.

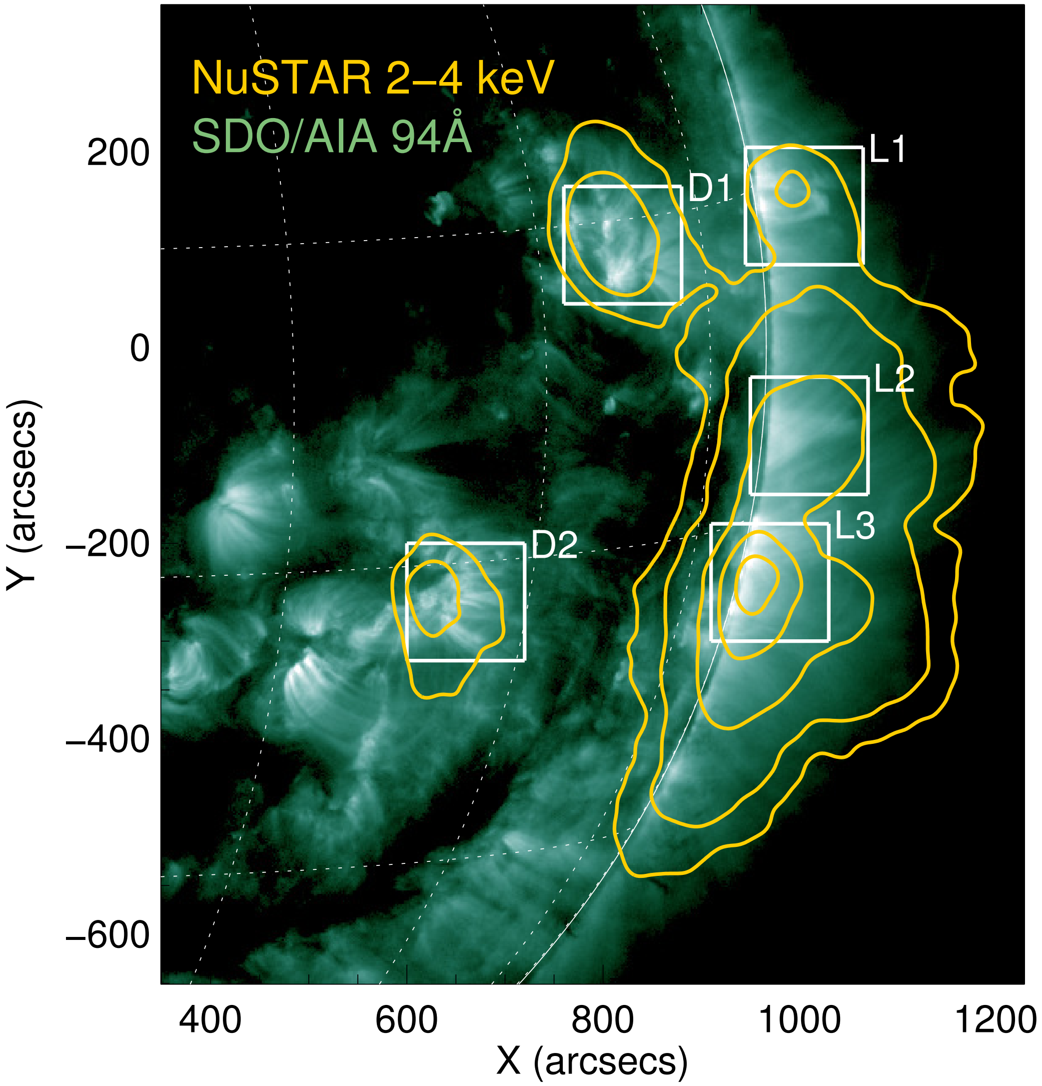

Figure 5.1: Combined EUV and HXR image of five active regions observed by *NuSTAR* on 2014 November 1 with an effective exposure time of 3.11 s. *NuSTAR* 2–4 keV flux contours (5, 10, 25, 50, and 80%) from the FPMA telescope are overlaid in yellow on a *SDO*/AIA 94 Å image showing plasma >1 MK within each region. White boxes are the areas used for analysis.

5.2 Solar Observations with *NuSTAR* and *FOXSI*

NuSTAR has two co-aligned X-ray optics focused onto two focal plane telescopes (FPMA & FPMB), with a field-of-view (FoV) of $\sim 12' \times 12'$ and a half-power diameter of $\sim 60''$ (Madsen et al. 2015). *NuSTAR* is well calibrated over the 3–79 keV bandpass and the lower energy bound can be extended to 2.5 keV if there is sufficient flux present. *NuSTAR* has observed active regions, the quiet Sun, and small solar flares over the course of its 9 solar observations to date(Grefenstette et al. 2016; Hannah et al. 2016; Kuhar et al. 2017). Of particular interest to us are quiescent active region observations on 2014 November 1 (Hannah et al. 2016). *NuSTAR* and *SDO*/AIA images of these regions are shown in Figure 5.1, while count spectra and isothermal fits for region D1 are shown in Figure 5.2. The other ARs from this observation (D2, L1, L2, and L3) also had fit temperatures between 3 and 4.5 MK and emission measures between 10^{46} and 10^{47} cm^{-3}. *NuSTAR* did not find evidence for plasma above $\sim$4 MK during this observation, possibly due to exposure constraints (low livetime led to effective exposure times of $\sim$3s per region). Our analysis currently includes only one of the two telescopes (FPMA), but work is underway to utilize data from FPMB.

The *Focusing Optics X-ray Solar Imager (FOXSI)* experiment is a sounding rocket payload that uses focusing optics to directly image solar photons between $\sim$4 and 20 keV. FOXSI has flown twice from White Sands, New Mexico and has observed small solar flares, active regions, and the quiet Sun. Here we analyze data from the second FOXSI flight on 2014 December 11 (Glesener et al. 2016). *FOXSI-2* targeted several areas of the Sun during the course of its 6.5 minute flight, including an active region near disk center that was quiescent at the time of the observation (Figure 5.3). Figure 5.4 shows the *FOXSI-2* detector 6 count spectrum of AR 12234 with 0.5 keV bins integrated over the 38.5 s observing period. Data from the other detectors is not included due to discrepancies in the response matrices. An isothermal fit of this spectrum gives a temperature T $\sim$ 11.3 MK and emission measure of $\times 10^{43}$ cm^{-3}, with a reduced chi-square of 0.95. While the count fluxes from this active region are fairly low, the presence of plasma $\gtrsim$10 MK is confirmed within the uncertainties

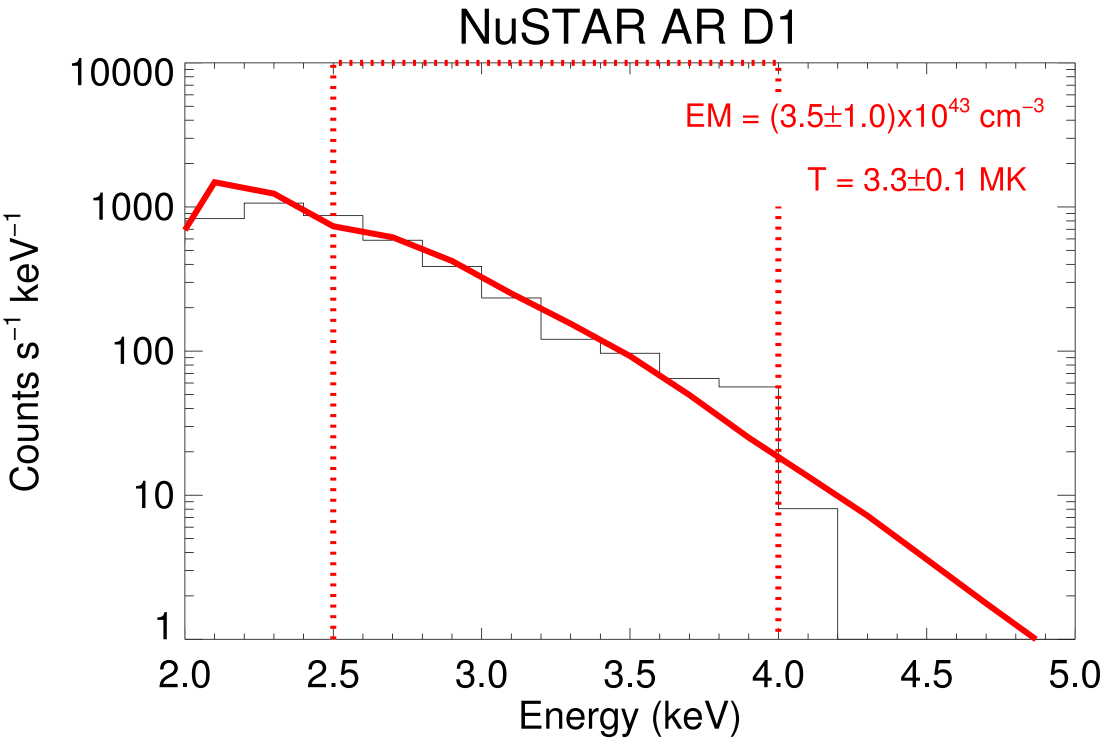

Figure 5.2: *NuSTAR* spectrum from the FPMA module for one of the on-disk active regions observed on 2014 November 1. Isothermal fits and uncertainties are labelled on the plot.

of the spectral fit. The Fe-line feature at 6.7 keV is an indicator of temperatures above 8 MK (Phillips 2004). A full differential emission measure (DEM) analysis of this active region with *FOXSI-2* and *Hinode* is presented in Ishikawa et al. (2017, in prep). This observation is the most direct detection of >10 MK plasma in a non-flaring solar active region.

5.3 Methods

5.3.1 Parameters and Their Selection

We simulated homogeneous nanoflare trains (in which every nanoflare is identical) with the EBTEL field line averaged (0-D) hydrodynamics code (Klimchuk et al. 2008; Cargill et al. 2012a,b). EBTEL is widely used in the solar physics community, and the model ouputs have been benchmarked against field aligned (1-D) numerical codes such as HYDRAD (Bradshaw & Cargill 2013). ebtel++[2] improves upon the original IDL code by incorporating two-fluid MHD equations and modifying heating parameters for better agreement with 1-D simulations (Barnes et al. 2016a). Because it is coded in C++ it also runs much faster than the IDL version. The original EBTEL code and ebtel++ give nearly identical results, and with the right parameter settings in ebtel++ are in fact identical. When we write "EBTEL" hereafter we are referring to ebtel++, though any statements could apply to both versions of the code. EBTEL accepts a user-defined time array, heating function, and loop (half) length as inputs. EBTEL subsequently calculates the strand-averaged pressure, density, and temperature at each time step. It also computes the differential emission measure in both the transition region (TR) and corona.

We used a triangular heating function for all of our simulations. The pulse height is the heating amplitude H_0 in erg cm^{-3} s^{-1} and the width is the event duration τ in seconds. In addition we included a constant, low-level background heating of 3.5×10^{-5} erg cm^{-3} s^{-1}. This term prevents catastrophic cooling of the loop strand at late times. Figure 5.5 shows two example heating functions and the corresponding

---

[2] `https://rice-solar-physics.github.io/ebtelPlusPlus/`

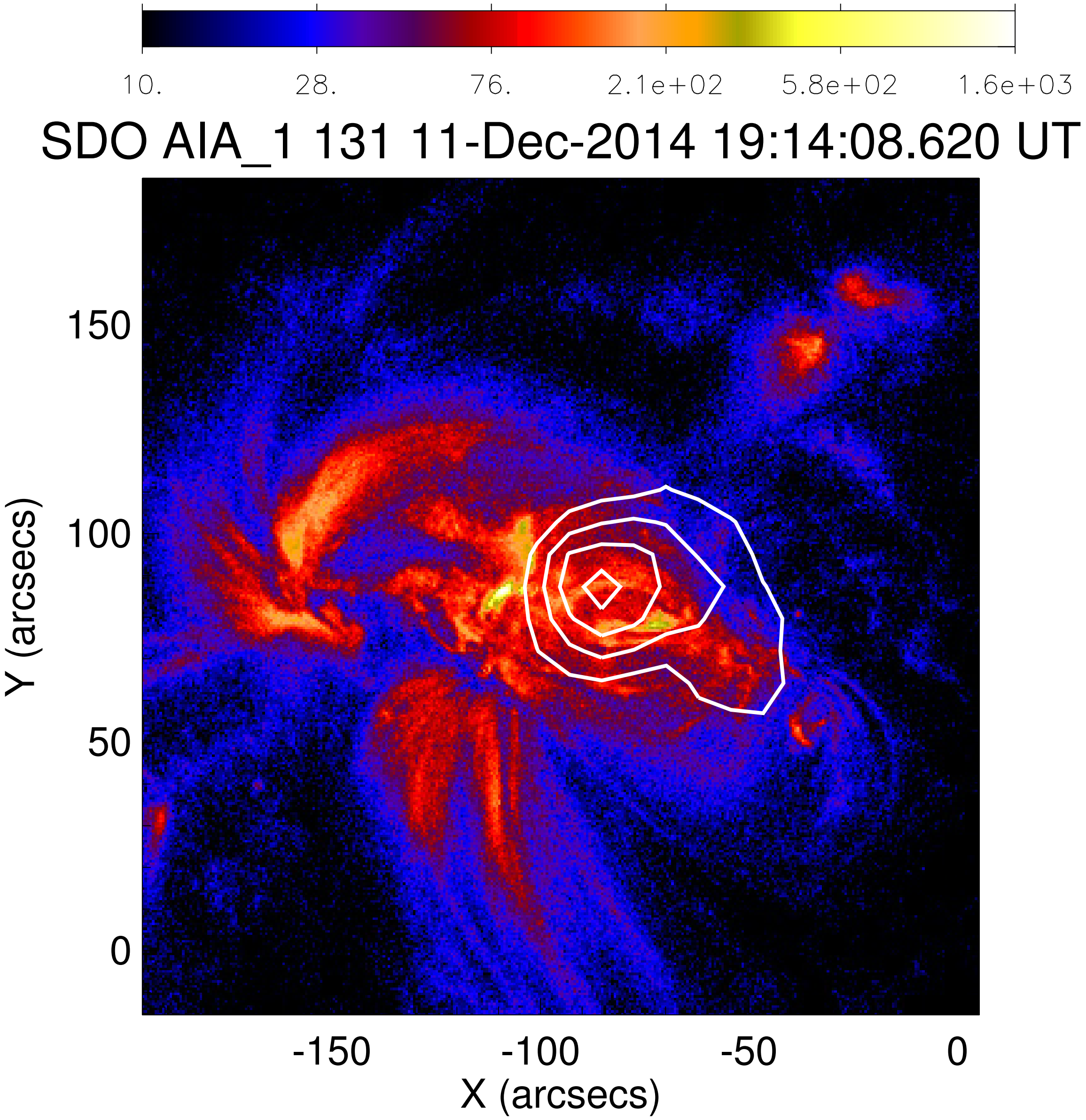

Figure 5.3: *FOXSI-2* 4–15 keV HXR contours from Det. 6 overlaid on a *SDO*/AIA image of AR 12234. The AIA image is shown on a log scale with a colorbar that indicates the brightness in each pixel. The *FOXSI-2* contours have been chosen to show 30, 50, 70, and 90% of the maximum value, and the *FOXSI-2* exposure time is 38.5 s.

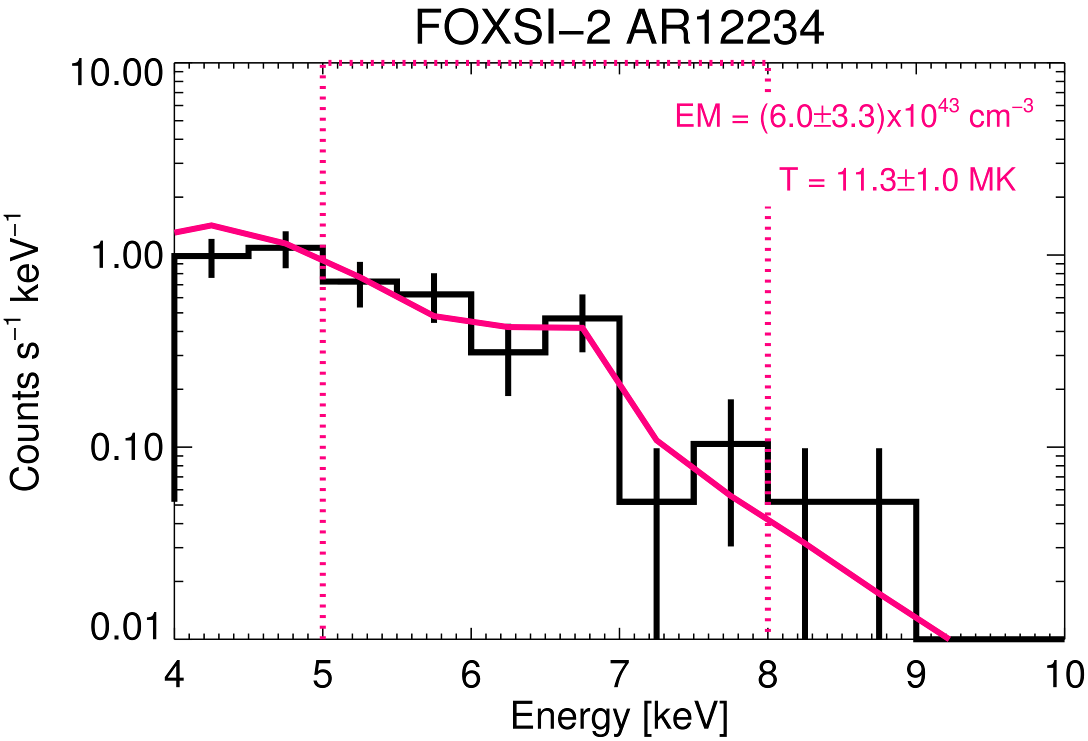

Figure 5.4: *FOXSI-2* count spectrum of AR 12234 from Det. 6. The best-fit isothermal T, EM, and 1-sigma uncertainties are written on the plot, and the fit range is marked by the dashed box.

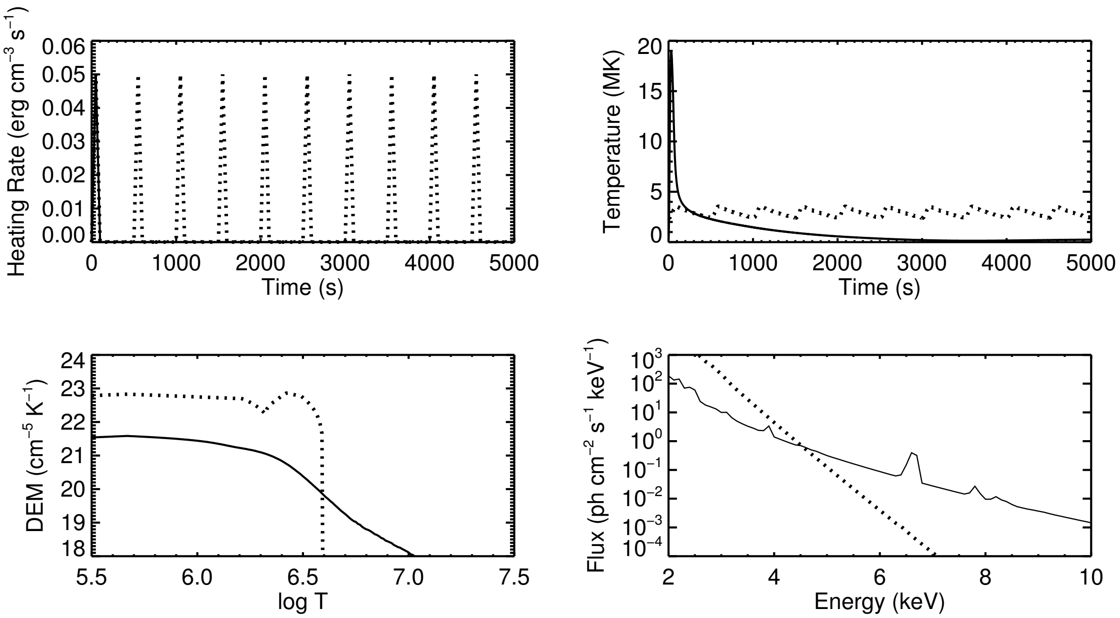

Figure 5.5: Examples of high-frequency ($t_N = 500$ s) and low-frequency ($t_N = 5000$ s) EBTEL simulations of nanoflare heating in a single loop strand with $\mathrm{H}_0 = 0.05$ erg cm^{-3} s^{-1}, $\tau = 100$ s, and L = $2{\times}10^9$ cm. Low-frequency values are indicated with solid lines and high-frequency values with dashed lines. The high-frequency train was started 5000 s before the plotted times to erase the initial plasma conditions. (Top left) Volumetric heating rate as a function of time. (Top right) Average loop temperature as a function of time. (Bottom left) Time-averaged DEM distributions. The discontinuity in the high-frequency curve is the intersection of the coronal and TR DEM curves. (Bottom right) Simulated X-ray spectra integrated over the full DEM and a 60×60 arcsecond area.

temperature evolution, density evolution, time-averaged DEMs, and HXR spectra for a single nanoflare and a nanoflare train with a 500 s delay. Low-frequency heating results in a DEM that extends to higher temperatures and a harder photon spectrum that includes prominent spectral lines. This results from the increased coronal density due to chromospheric evaporation following a given heating event. Higher density strands require more energy to heat to the same temperature, so higher-frequency nanoflares produce cooler plasma than lower-frequency events with the same heating amplitude. The single nanoflare case can be thought of as a component of a nanoflare train with a delay time of 5000 s, which is longer than the cooling time.

Time-averaging the DEM distributions produces a superposition of every stage of heating and cooling in a particular EBTEL run. This is what we might expect to see when looking at an active region through the optically thin corona, as all the loops in various stages of heating and cooling along a line-of-sight will contribute to each spatial pixel. We assumed a fixed coronal scale height of $\sim 5\times10^9$ cm throughout our analysis. With this scale height and an active region area we calculated a model photon spectrum from a given EBTEL DEM. That spectrum was then convolved with the instrument response function of either *NuSTAR* or *FOXSI-2*. This allowed us to make straightforward comparisons to the observed count spectra for a given set of model parameters. Note that EBTEL produces DEMs separately for the transition region and the corona. For on-disk regions such as AR 12234 and *NuSTAR* ARs D1 and D2, we expect a significant contribution from the transition region to the line-of-sight plasma emission. However, for off-limb regions such as *NuSTAR* ARs L1, L2 and L3 we expect to see predominantly coronal emission. Therefore for L1, L2, and L3 we only use the coronal portion of the EBTEL DEM from each nanoflare model.

The physical parameters that alter the X-ray spectra are H_0, τ, the delay t_N, the loop half-length L, and the filling factor f. f is a normalization that reflects the fact that in a given volume of the corona, only a certain fraction of loop strands may be impulsively heated. We varied H_0, τ, t_N, and f across a range of values for each active region to determine which parameter combinations gave good agreement with observations. The shortest value of delay was set to the longest value of duration to avoid overlapping events. The average loop half-length L was estimated separately

Active Region	Loop Half-Length (cm)
AR 12234	6×10^9
NuSTAR D1	7×10^9
NuSTAR D2	7×10^9
NuSTAR L1	7×10^9
NuSTAR L2	1×10^{10}
NuSTAR L3	7×10^9

Table 5.1: Table of estimated loop lengths for the 5 *NuSTAR* and single *FOXSI-2* active regions. Numbers were obtained from manual selection of loop footpoints in *SDO*/AIA 171 Å images.

for each region with images from *SDO*/AIA and the following procedure.

The *FOXSI-2* observation of AR 12234 took place when this region was close to disk center. To estimate the average coronal loop length, we measured the distances between several visible pairs of loop footpoints in the *SDO*/AIA 171 Å channel. The regions observed by *NuSTAR* on 2014 Nov 1 were close to or over the limb, which made it difficult to see clear loop structures. Therefore, we used AIA 171 Å images from 2014 October 28 to calculate footpoint distances for these regions. Next we corrected for projection effects by dividing each measured footpoint separation by cos(longitude). We assumed semi-circular loop geometries for every region and determined the average half-lengths L=$\pi d/4$, where d is the longitude-corrected average footpoint separation for a given region. The loop length estimates for each region are listed in Table 5.1.

Once a characteristic loop length was determined for a particular region, we engaged in a systematic exploration of the nanoflare parameter space (heating, duration, delay, and filling factor). First we created a 4D datacube for each region, with logarithmically spaced values of the nanoflare parameters H_0, τ, and t_N corresponding to the first 3 dimensions. The range of physical parameters that was explored is given in Table 5.2. The 4th dimension contained the model X-ray spectrum from the EBTEL simulation corresponding to the appropriate parameter values. Subsequently we made 3D arrays containing the total chi-square and likelihood for each model spectrum compared to the observation. This was done separately for each active region. The energy ranges over which we calculated these statistics were 2.5 to 5 keV

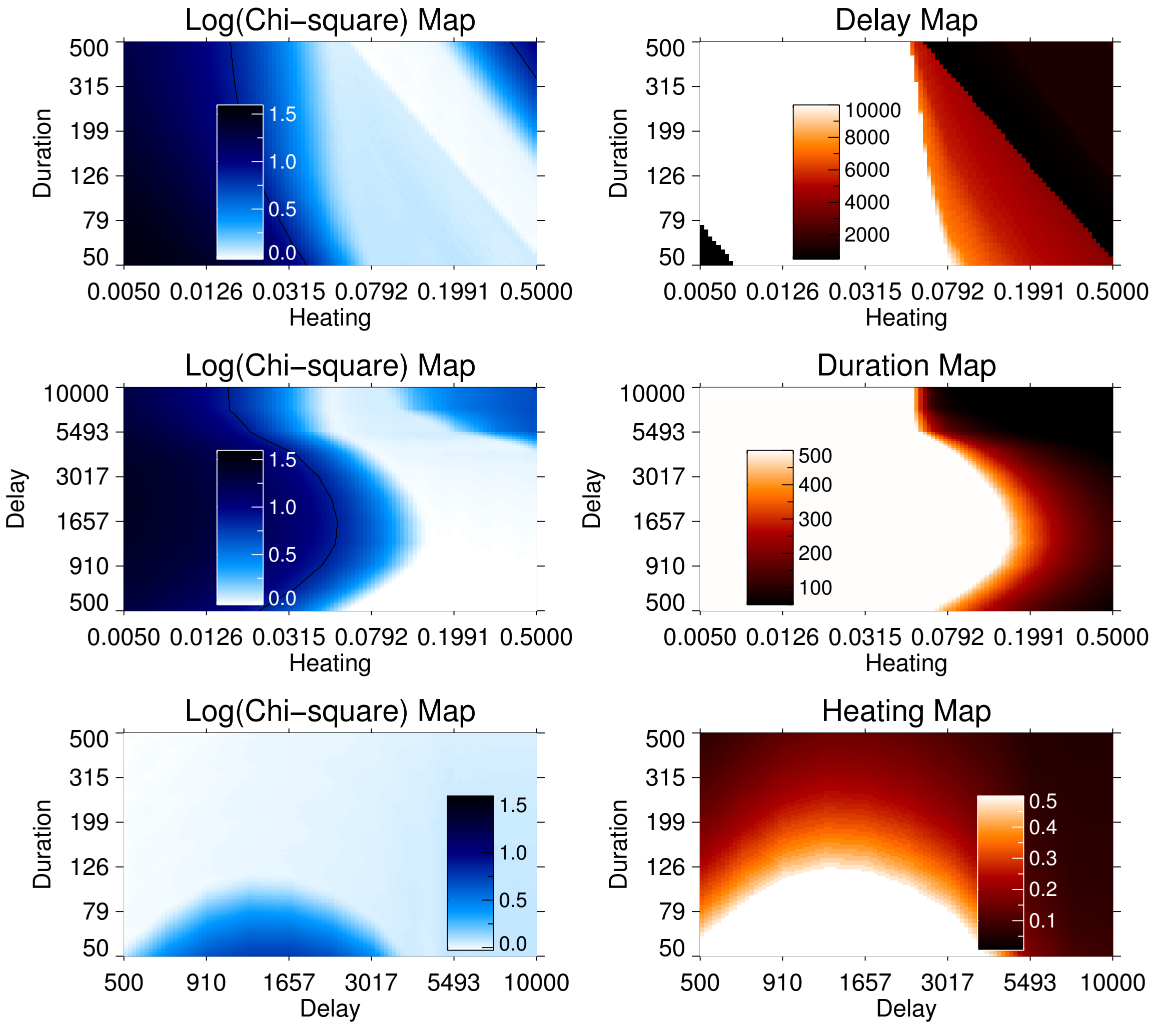

Figure 5.6: (Left) Log chi-square intensity maps for the *FOXSI*-observed AR spectrum. Parameter pairs are H_0 vs. τ, H_0 vs. t_N, and t_N vs. τ with the third (unplotted) parameter optimized at every location. Brighter pixels indicate better fits. (Right) Heat maps showing the optimized values of the unplotted parameter for each intensity map in the same row. No constraints have been applied to the parameter space. Black lines in the left panels show 90% confidence levels for the case of 3 relevant parameters (Avni 1976).

Physical Parameter	Range of Values
H_0	0.005–0.5 erg cm^{-3} s^{-1}
τ	50–500 s
t_N	500–10,000 s

Table 5.2: Range of physical parameters for simulated nanoflare trains.

for *NuSTAR* and 5 to 10 keV for *FOXSI-2*. The likelihood was determined using every energy bin of the observed spectra in the energy range of interest, while the chi-square was determined using only the bins with >0 accumulated counts. During the fitting process we determined the best value of f for each combination of H_0, τ, and t_N. This "re-optimization" of the filling factor made it easier to determine what regions of parameter space fit well for the physical quantities of primary interest (H_0, τ, and t_N). To visualize which regions of parameter space gave good fits, we plotted intensity maps in two dimensions. These maps showed that the qualitative behavior of likelihood (not shown) and chi-square are virtually the same for all the active regions.

The left-hand panels of Figure 5.6 shows chi-square intensity maps in two dimensions for the *FOXSI*-observed active region, with the unplotted parameters optimized to produce the best fit. The right-hand panels of Figure 5.6 show parameter intensity maps indicating the best-fit values of the unplotted parameter in every pixel. The blue lines show the 90% confidence intervals calculated by the method of Avni (1976) for the case of three relevant parameters (heating, duration, and delay in this case). This particular interval corresponds to an increase in the unreduced chi-square of 6.25 relative to the minimum. We acknowledge that due to the presence of bins with few or no counts in them, chi-square is not an entirely appropriate measure of fit quality. We are working on Monte-Carlo simulations of likelihood that can provide more accurate assessments of fit quality; however, we don't expect significant changes in the nature of our results.

In our explorations of this parameter space we found many sets of solutions that gave acceptable fits to the HXR data. This is not surprising given the multidimensional nature of the parameter space and the degeneracy between the various parameters (for example, increasing either the heating amplitude or the event duration will increase the energy in a particular nanoflare and also increase the flux of the simulated X-ray spectrum). However, this does mean that it was important for us to use as many external constraints as possible (such as energy flux limits and observations at other wavelengths).

5.3.2 Constraints on the Nanoflare Parameter Space

It is generally accepted that mechanical motions in and below the photosphere are the ultimate drivers of coronal heating (Klimchuk 2006). The Poynting flux associated with flows stressing the footpoints of magnetic fields is given by

$$F = \frac{1}{4\pi} B_V^2 V_h tan(\theta) \qquad \text{erg cm}^{-2}\ \text{s}^{-1} \tag{5.1}$$

where B_V is the vertical component of the field, V_h is the horizontal velocity and θ is the tilt angle of the field. Typical observed values in active regions are ~100 G, 1 km s^{-1}, and 20 degrees, which equates to a flux of 3×10^7 erg cm^{-2} s^{-1}. Withbroe & Noyes (1977) calculated an average coronal energy flux of 10^7 erg cm^{-2} s^{-1}. For a given loop strand we don't expect the time-averaged energy flux to exceed 10^8 erg cm^{-2} s^{-1}, as this amount of energy flux would imply photospheric motions significantly faster than what is observed. This flux can be re-written in terms of the physical parameters of a nanoflare train:

$$F = \frac{H_0 \tau L}{2 t_N} \qquad \text{erg cm}^{-2}\ \text{s}^{-1} \tag{5.2}$$

Here H_0 is the peak nanoflare heating amplitude, τ is the nanoflare duration, L is the loop half-length, and t_N is the delay between events. We implemented the requirement that F $< 10^8$ erg cm^{-2} s^{-1} for any set of parameters.

We placed additional constraints on the nanoflare parameter space with co-temporal observations from *SDO*/AIA and *Hinode*/XRT. *SDO*/AIA data are available for the *NuSTAR* and *FOXSI-2* observations on 2014 November 1 and 2014 December 11, while *Hinode*/XRT data is only available for the *FOXSI-2* flight. We calculated active region fluxes in DN s^{-1} pixel^{-1} in multiple wavelengths for AIA (94, 131, 171, 193,

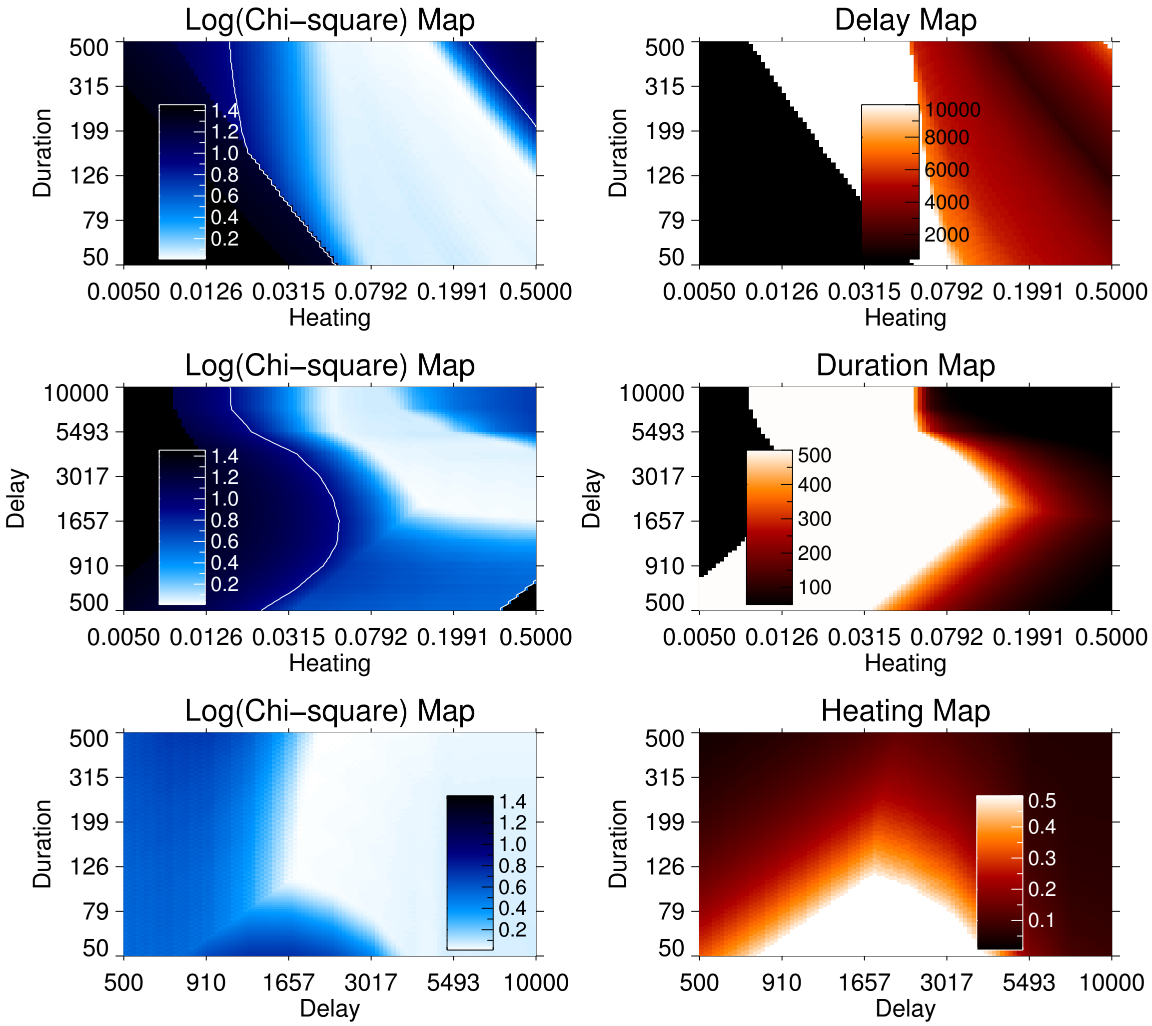

Figure 5.7: (Left) As Figure 5.6, but the energy flux limit (Equation 5.2) and EUV/SXR limits from *SDO*/AIA and *Hinode*/XRT have been applied to the full parameter space. White (instead of black) lines in the left panels show 90% confidence levels for the case of 3 relevant parameters.

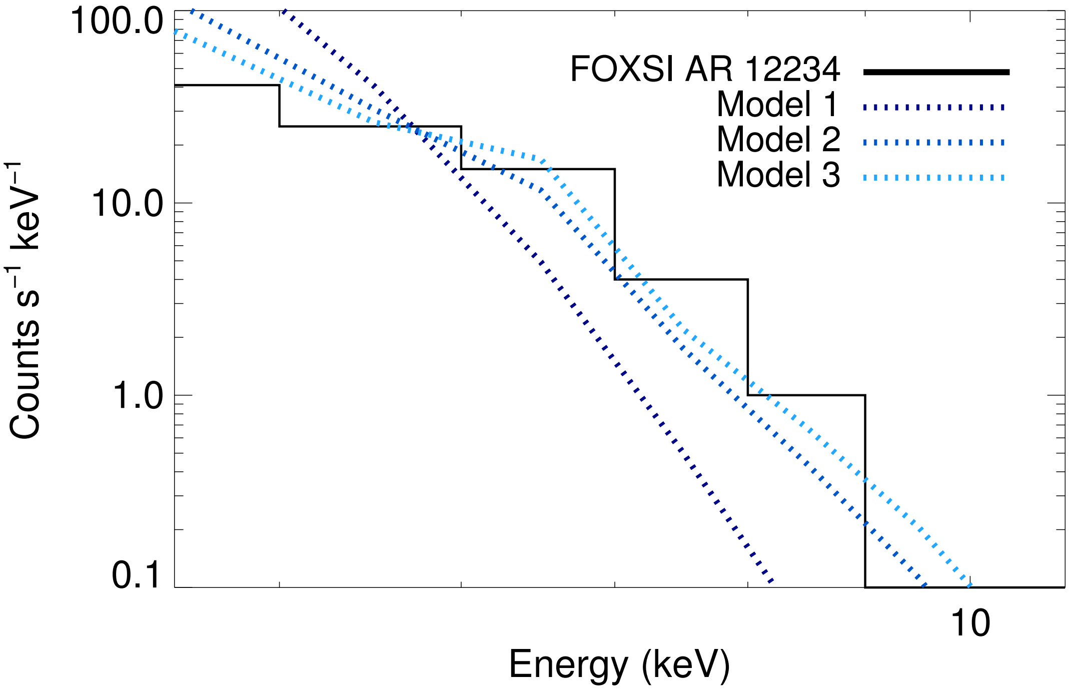

Figure 5.8: *FOXSI-2* spectrum of AR 12234 and three model fits at three different points in the re-optimized heating vs. duration parameter space with no limits (Figure 5.6, top left). The [H_0, τ] coordinates for models 1, 2, and 3 are [0.013, 79], [0.032, 126], and [0.079, 199] respectively.

211, 335 Å) and multiple filters for XRT (Be-thick, Al-thick, Ti-poly, Al-mesh, Al-poly/Ti-poly, C-poly/Ti-poly, Be-thin, Be-med, Al-med, Al-poly). For a particular nanoflare model we calculated predicted fluxes for both instruments in every waveband. We required the predicted AIA and XRT fluxes to be <3 times the average observed fluxes for each region, and if this requirement wasn't met for all wavelengths we excluded that particular model. We did not set a lower limit on the EUV/SXR flux because a different or additional population of nanoflares (at different frequencies, for example) could be present at lower temperatures.

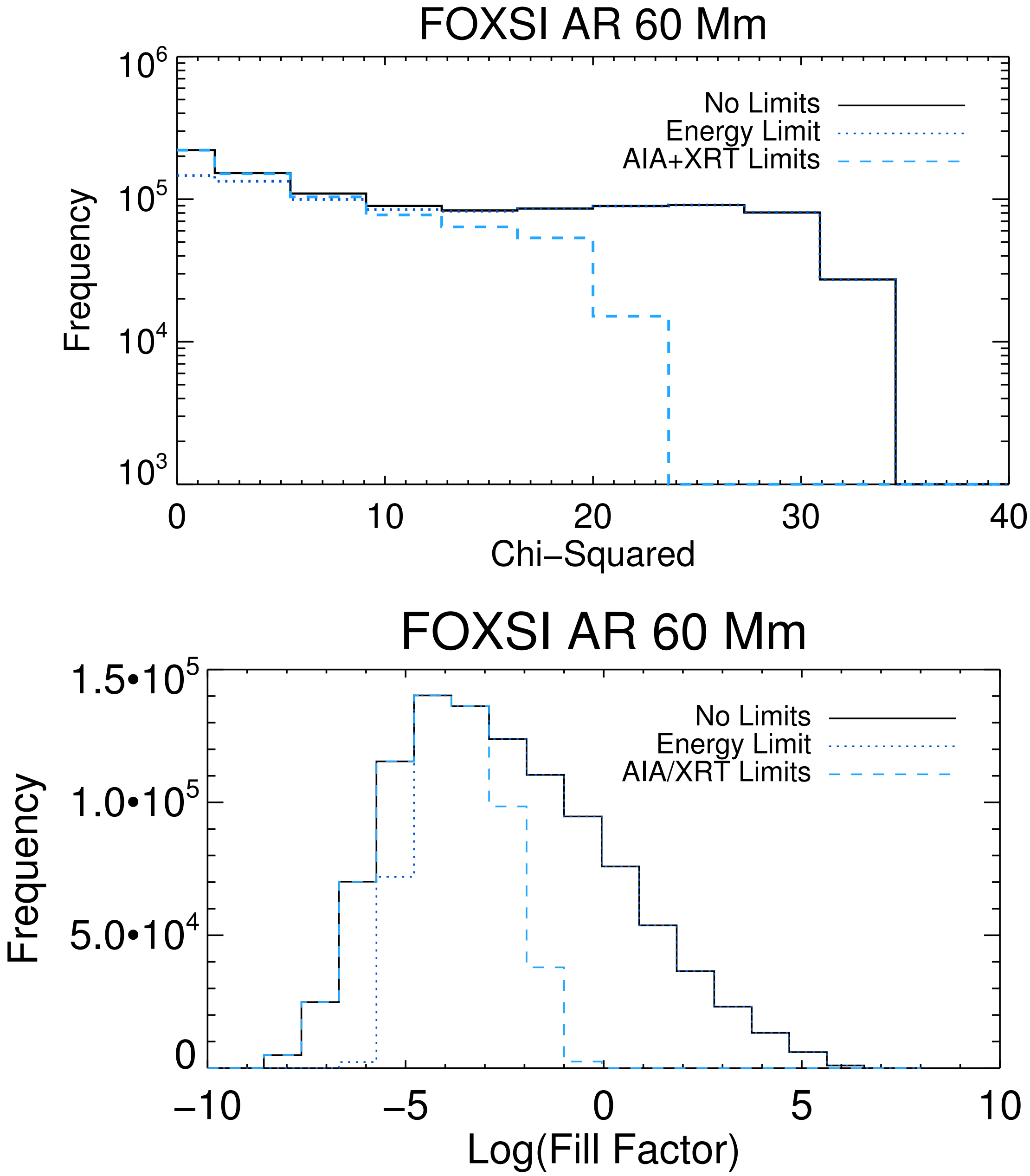

Figure 5.9: Histograms of the chi-square (top) and fill factor (bottom) for the FOXSI AR and three different sets of limits: no limits, energy flux limits, and AIA+XRT limits.

5.4 Results and Discussion

Figure 5.7 shows chi-square intensity maps for the *FOXSI*-observed active region, with the nanoflare models subjected to physical (energy flux) and observational (EUV & SXR) constraints. Adding these constraints excludes a portion of parameter space, as seen from the dimming of the chi-square plots relative to the unconstrained case shown in Figure 5.6. However, the 90% confidence levels for the parameters are less dramatically changed. Heating amplitudes >0.02 erg cm^{-2} s^{-1} is a general requirement of the parameter space. Delay and duration are poorly constrained for this spectrum. The delays for this AR in the best-fit regions ($t_N > 1700$ s) are consistent with previous studies of simulated emission measure distributions (Cargill 2014), observations of transient Fe XVIII brightenings (Ugarte-Urra & Warren 2014), and time-lag studies (Bradshaw & Viall 2016). However, we cannot rule out any value of the delay with confidence. In addition, for some parts of the well fit parameter space the third, unplotted parameter is getting pegged at its maximum value. This means that we may need to consider larger values of heating amplitude and delay in order to better constrain the parameter space. Smaller values of duration may also be investigated; larger values would cause overlapping nanoflare trains for the smallest values of delay and should be avoided.

Figure 5.8 shows three example models drawn from the heating/duration 2-D parameter space, with an optimized delay and fill factor at every location. Better fits occur for models that include an iron line feature (models 2 and 3 in this plot). The parameters of each model are as follows: H_0 = 0.013, 0.031, 0.079 erg cm^{-3} s^{-1}, τ = 79, 126, 199 s, t_N = 10000, 10000, 5330 s, and f = 63, 0.19, 0.0013 for models 1, 2, and 3 respectively. This figure is meant to show the difference in fit quality between various regions of the chi-square parameter space. The unphysical value of $f = 63$ goes away when multi-wavelength and energy limits are applied, but is the best fit normalization for the given model 1 parameter values. Figure 5.9 shows histograms of the chi-square and filling factor for model fits to the *FOXSI*-observed active region with no limits, energy flux limits, and AIA+XRT limits. The chi-square plots show that there are a significant number of parameter combinations that yield

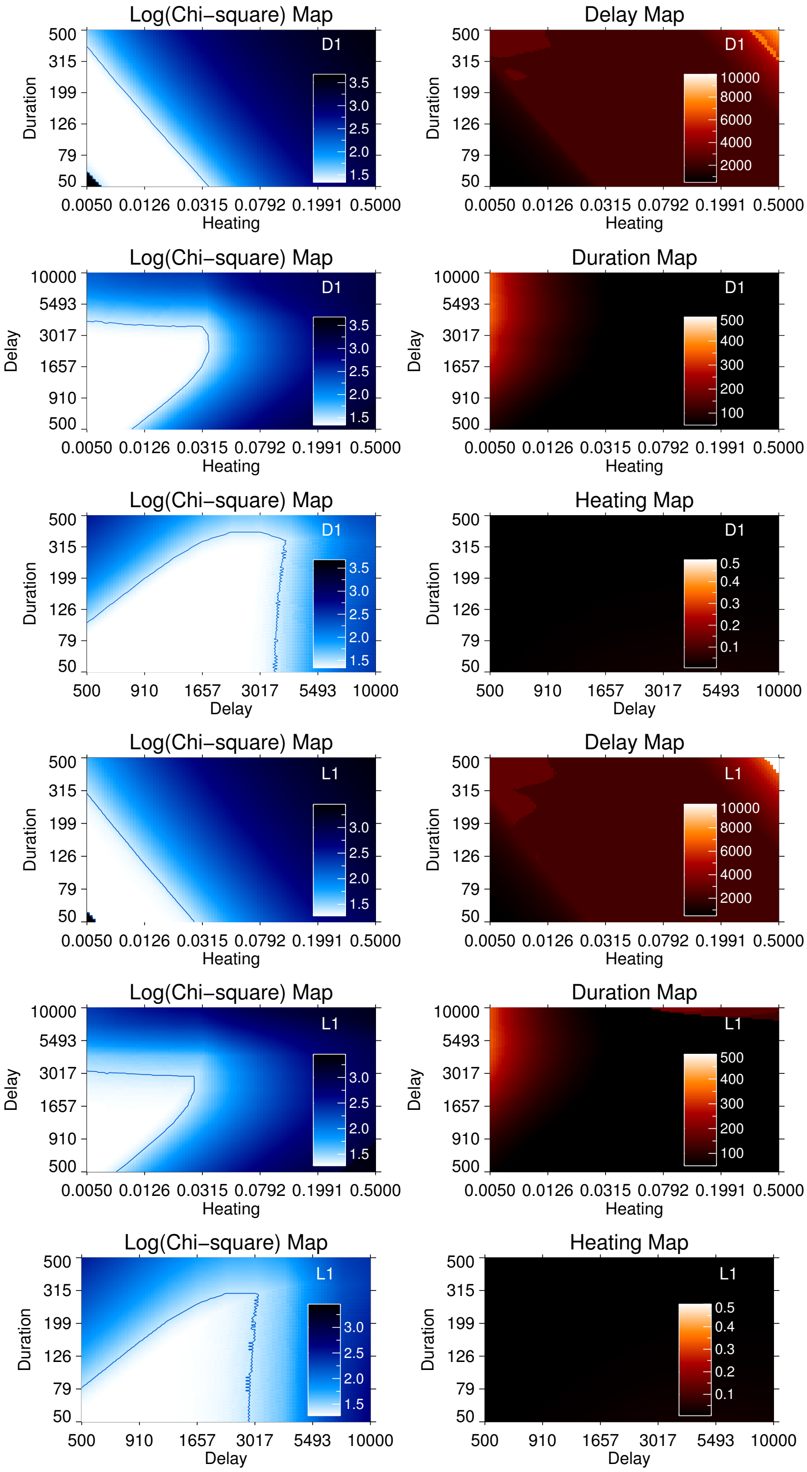

Figure 5.10: (Left column) Log chi-square intensity maps for two *NuSTAR* AR spectra (D1 and L1) with same formatting as Figure 5.7. Blue lines in the left panels show 90% confidence levels for the case of 3 relevant parameters.

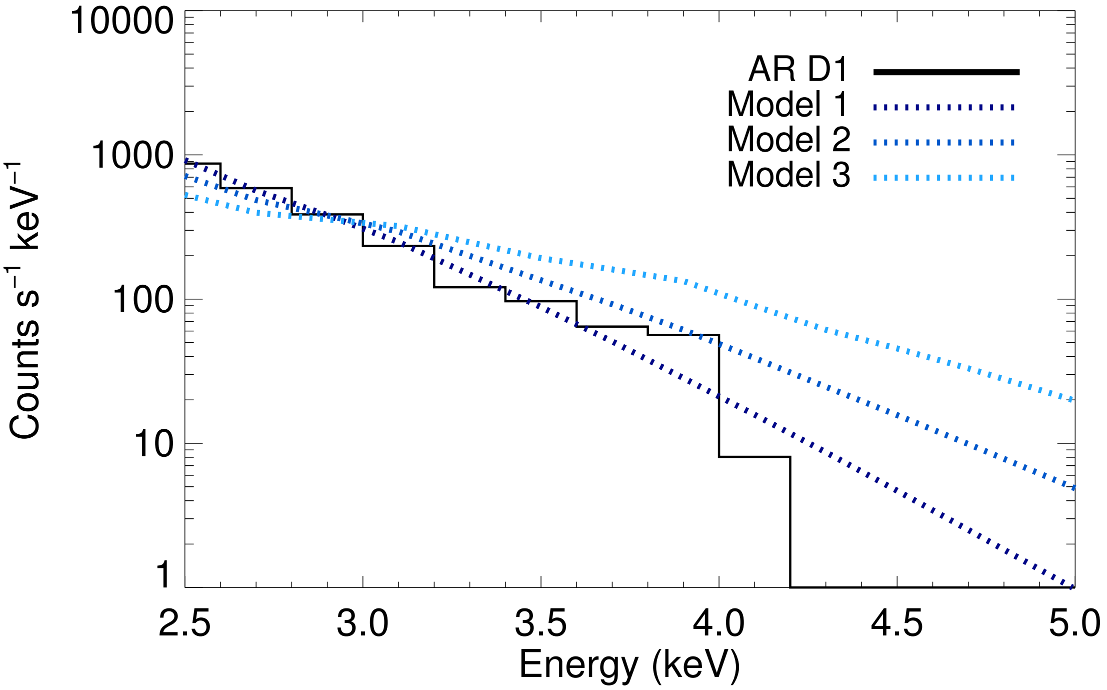

Figure 5.11: *NuSTAR* spectrum of AR D1 and three model fits at three different points in the re-optimized heating vs. duration parameter space with energy and EUV limits included (Figure 5.10, top left). The $[H_0, \tau]$ coordinates for models 1, 2, and 3 are [0.013, 79], [0.032, 126], and [0.079, 199] respectively.

acceptable fits to the AR spectrum, as seen in the likelihood intensity maps. Without any constraints there is a large range of filling factors due to the fitting procedure described in Section 5.3. When the energy and EUV/SXR constraints are applied the range of acceptable filling factors is significantly reduced; most importantly, non-physical values of $f >> 1$ are ruled out. Large (unphysical) filling factors are ruled out by AIA+XRT and small filling factors are ruled out by the energy flux constraint. Importantly, a subset of well fitting models is excluded by the energy limit; these models include predominantly short delays.

Figure 5.10 shows chi-square intensity maps for two of the five *NuSTAR*-observed active regions with energy and observational constraints imposed. The shapes and values of the chi-square maps are similar for the regions that are not shown here. We used data from the FPMA telescope only; the spectral fits for FPMA and FPMB are nearly identical for most of the active regions (Hannah et al. 2016) and we don't expect the use of FPMB to alter our results significantly. The shapes of the allowed parameter space areas are noticeably different for these regions than for the *FOXSI*-observed AR. The required heating amplitudes are smaller, as would be expected from the temperature difference between the active regions. Shorter delays are preferred and delay times above several thousand seconds are excluded. Interestingly, neither L2 nor L3 is fit well by any combination of H_0, τ, t_N, and f. The model fits to the *NuSTAR* observations are generally poorer than fits to AR 12234, which is a natural consequence of the smaller error bars (higher total counts) in these spectra.

Figure 5.11 shows three example models drawn from the heating/duration 2-D parameter space, with an optimized delay and fill factor at every location. Better fits occur for models that include an iron line feature (models 2 and 3 in this plot). The parameters of each model are as follows: H_0 = 0.013, 0.031, 0.079 erg cm^{-3} s^{-1}, τ = 79, 126, 199 s, t_N = 1228, 2236, 2236 s, and f = 0.1, 0.007, 0.0002 for models 1, 2, and 3 respectively. The agreement of the nanoflare models with the *NuSTAR* AR data is shown by the chi-square histograms in Figure 5.12. The fill factor histograms (also in Figure 5.12) verify that large (unphysical) filling factors are again ruled out by AIA, and small filling factors are ruled out by the energy flux constraint.

5.5 Conclusions

For the hot (best-fit isothermal T > 10 MK) *FOXSI*-observed AR we are able to generate good fits using homogeneous nanoflares with a wide range of delay times, subject to energetic and observational EUV/SXR constraints. The best fits occur for t_N >1700 s, which is in agreement with previous studies that did not use HXR data. For the cooler regions (best-fit temperatures 3–4 MK) observed by *NuSTAR*, the homogeneous nanoflare model is not as successful. These results are consistent with previous work by e.g. Reep et al. (2013); Cargill (2014) that showed it is difficult to produce the range of observed AR DEM slopes with equally spaced, constant energy nanoflares. Cargill (2014); Cargill et al. (2015) showed that it is possible to reproduce

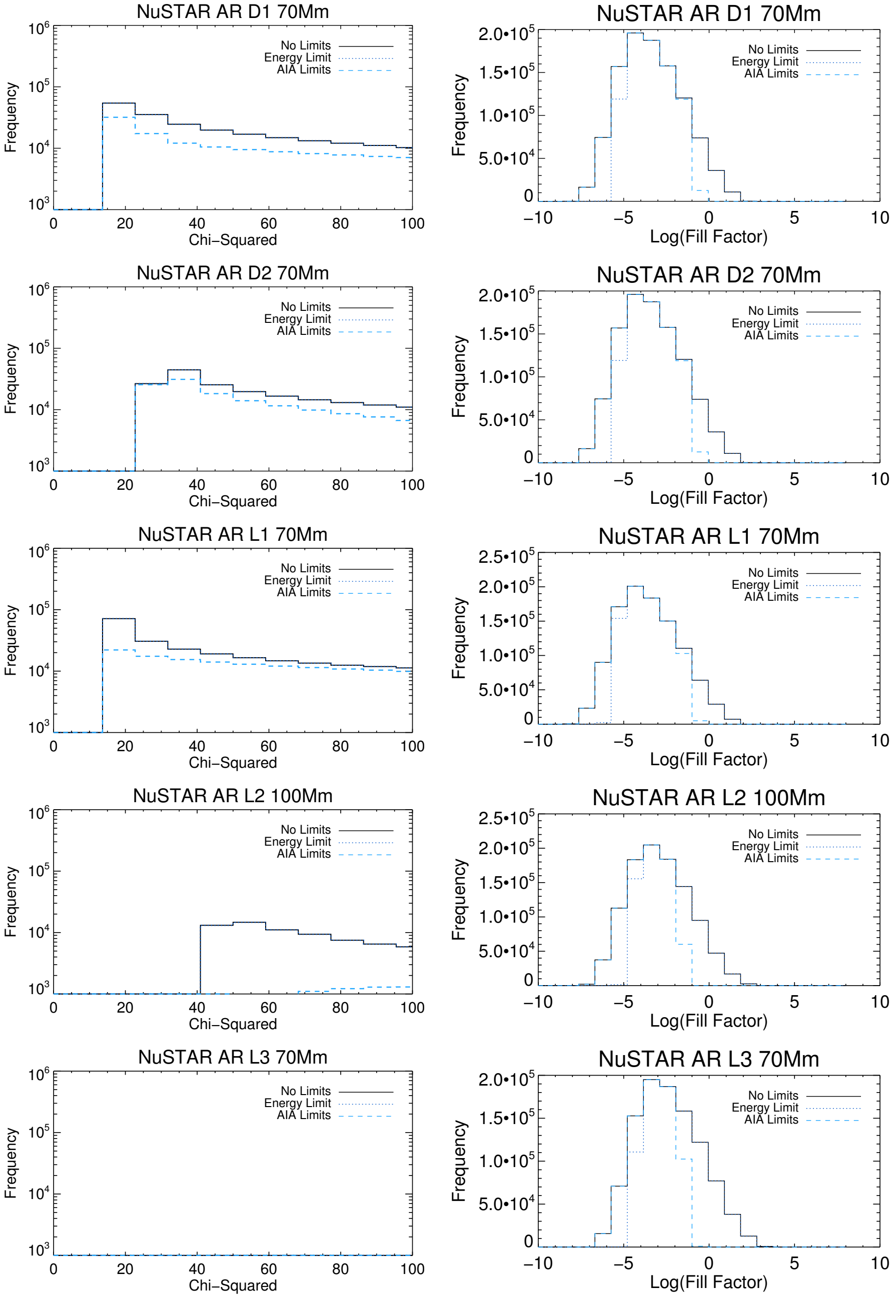

Figure 5.12: Histograms of the chi-square (top) and fill factor (bottom) for the 5 *NuSTAR*-observed ARs and three different sets of limits: no limits, energy flux limits, and AIA limits.

a broad range of slopes with nanoflare trains that incorporate an energy-dependent delay time. This is a more physically motivated model, as the magnetic free energy that is thought to power nanoflares would need more time to regenerate after larger events that release more energy (although fields may not relax to their potential state after each event). Other authors (e.g. Barnes et al. 2016b; Bradshaw & Viall 2016; López Fuentes & Klimchuk 2016) have used heating amplitudes drawn from a power-law distribution instead of equal-energy nanoflares. The analysis of power-law distributions in energy and variable delay times is beyond the scope of this work, but will be explored in future work. In addition, comparisons with 1-D simulations will put additional constraints on which regions of parameter space can model active region HXR fluxes within the constraints of additional low-temperature observations.

NuSTAR has observed many more active regions since 2014 November 1, several of which were non-flaring and would be suitable for nanoflare studies. The combination of *NuSTAR* and *FOXSI-2* observations show how valuable HXR focusing instruments can be, and their particular application to solving the coronal heating problem has only just begun.

Chapter 6

Future Work and Conclusions

6.1 Future Work

As discussed in Chapter 4, *NuSTAR* observations at solar minimum can be over two orders of magnitude more sensitive to transient events than in the 2014 November 1 observation. Indeed, *NuSTAR* observed a quiet Sun transient event of *GOES*-class A0.004 on 2017 March 21, the smallest event seen by the instrument to date. This and other events from the same observation will be the subject of an upcoming paper. With additional observations in the next few years *NuSTAR* may be able to compile a survey of these faint events and greatly enhance our understanding of quiet Sun physics.

FOXSI-3 is scheduled to fly in 2018. Solar conditions will strongly determine the scientific outcomes of this flight, which may yield further insight into the physics of active regions, the quiet Sun, flares, or any combination thereof. A NASA Small Explorer that combines features of *NuSTAR* and the *FOXSI* rockets has recently been proposed (Christe et al. 2017). Although *NuSTAR* and *FOXSI* continue to advance knowledge of solar HXRs, together they observe the Sun less than one time a month. A solar-dedicated HXR focusing satellite would lead to significant improvements in understanding particle acceleration in flares and coronal heating mechanisms (for example, see Figure 6.1).

The analysis described in Chapter 5 used trains of identical nanoflares. However,

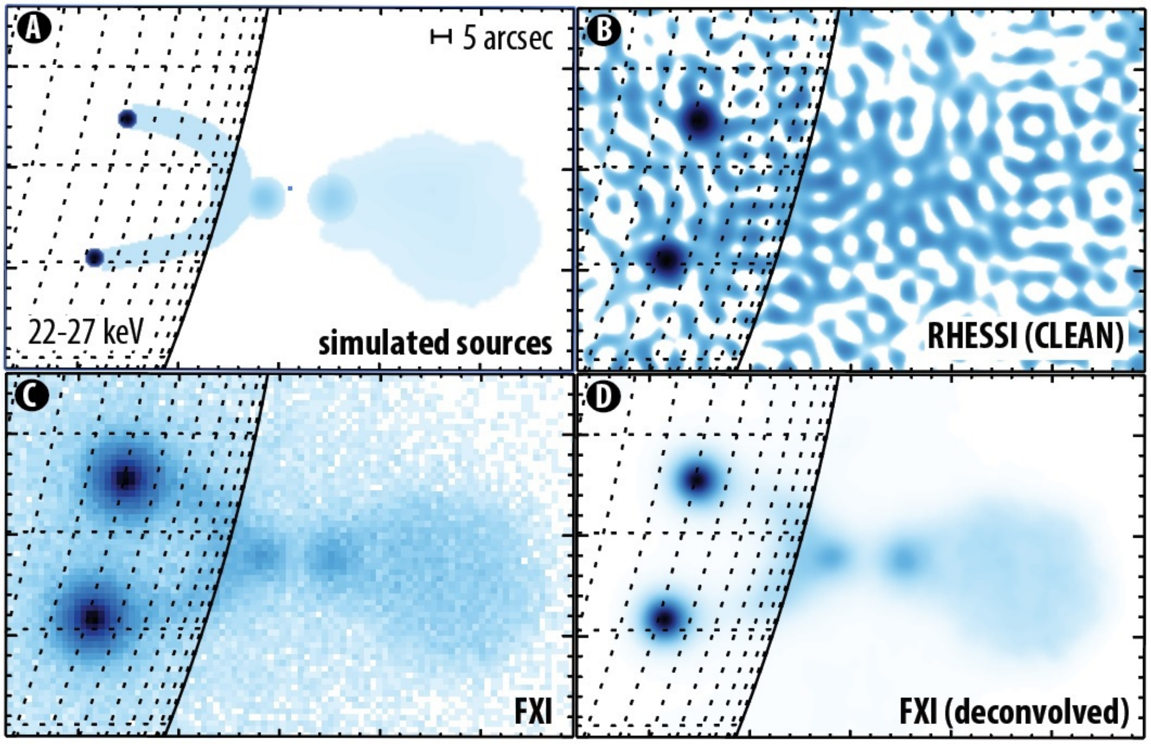

Figure 6.1: (A) Simulated 22–27 keV HXR sources, including footpoints, a heated loop, and accelerated particles above the looptop. (B) Simulated *RHESSI* image of this configuration. The coronal sources are not visible due to limited dynamic range. (C) Simulated image from the proposed *FOXSI/FXI* satellite. Better sensitivity and dynamic range result in reduced sidelobes. (D) *FOXSI/FXI* image including the PSF deconvolution. All of the simulated sources are now clearly visible, showing the advantage of a dedicated solar HXR focusing instrument. Figure from Christe et al. (2017).

several authors have shown that it is difficult to reproduce the observed temperature distributions of active regions using sequences of nanoflares with equal energy and equal spacing (Cargill 2014; Reep et al. 2013). More physically realistic models include nanoflare energies in a power-law distribution and energy-dependent delay times (Figure 6.2). A future paper will incorporate both of these features into EBTEL nanoflare models and put additional constraints on the properties of active region nanoflares. In addition, 1-D loop heating simulations with can be used to validate the results obtained with EBTEL. Another possible addition to the modelling process is a separate treatment of electrons and ions with the ebtel++ code (Barnes et al. 2016b).

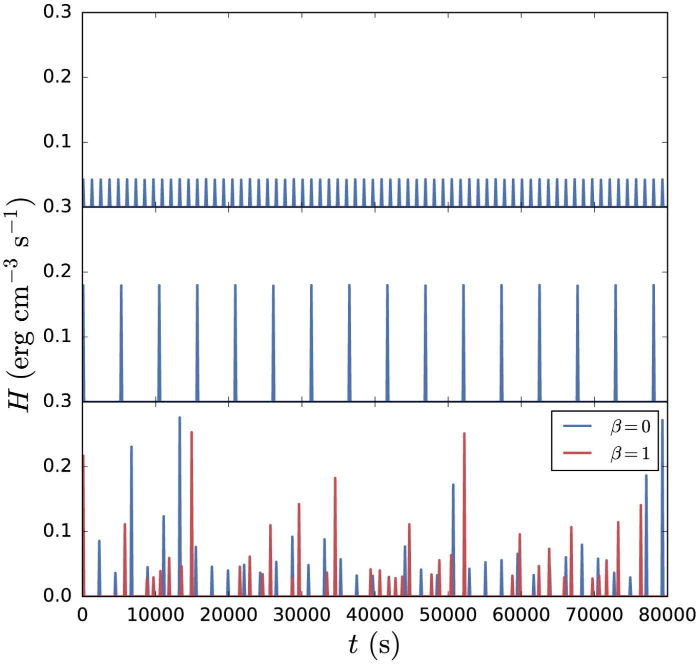

Figure 6.2: Examples of four different nanoflare trains. (Top) Nanoflares with identical heating amplitudes and $t_N = 1000$ s. (Middle) Nanoflares with identical heating amplitudes at $t_N = 5000$ s. (Bottom) Nanoflares with heating amplitudes from a power-law distribution with index -1.5. Events shown in blue have uniform delay times, and events shown in red have delay times that depend on the previous event energy (the average delay for both is 2000 s). Figure from Barnes et al. (2016b).

6.2 Conclusions

Focusing hard X-rays >2 keV has already led to advances in the knowledge of active regions, the quiet Sun, and transient events in the corona. Several publications have resulted from *NuSTAR* and *FOXSI* observations over the last three years, and several more are currently in preparation. It is clear that future observations with HXR focusing instruments will greatly improve the heliophysics community's understanding of particle acceleration and heating in the solar corona.

Bibliography

Als-Nielsen, J., McMorrow, D., & Robinson, I. 2011, Elements of Modern X-Ray Physics, 2nd Edition (Wiley)

Arnaud, M., & Raymond, J. 1992, ApJ, 398, 394

Aschenbach, B. 2009, Experimental Astronomy, 26, 95

Aschwanden, M. J. 2004, Physics of the Solar Corona. An Introduction (Praxis Publishing Ltd)

Aschwanden, M. J., Tarbell, T. D., Nightingale, R. W., et al. 2000, ApJ, 535, 1047

Aschwanden, M. J., Caspi, A., Cohen, C. M. S., et al. 2017, ApJ, 836, 17

Avni, Y. 1976, ApJ, 210, 642

Bahng, J., & Schwarzschild, M. 1961, ApJ, 134, 312

Barnes, W. T., Cargill, P. J., & Bradshaw, S. J. 2016a, ApJ, 829, 31

—. 2016b, ApJ, 833, 217

Beck, J. G. 2000, Sol. Phys., 191, 47

Benz, A. O. 2017, Living Reviews in Solar Physics, 14, 2

Benz, A. O., & Krucker, S. 2002, ApJ, 568, 413

Bhalerao, V. 2012, PhD thesis, Caltech

Birn, J., Drake, J. F., Shay, M. A., et al. 2001, JGR, 106, 3715

Bradshaw, S. J., & Cargill, P. J. 2006, A&A, 458, 987

—. 2013, ApJ, 770, 12

Bradshaw, S. J., & Klimchuk, J. A. 2011, ApJS, 194, 26

Bradshaw, S. J., & Viall, N. M. 2016, ApJ, 821, 63

Brosius, J. W., Daw, A. N., & Rabin, D. M. 2014, ApJ, 790, 112

Brown, J. C. 1971, Sol. Phys., 18, 489

Buitrago-Casas, J. C., Krucker, S., Christe, S., et al. 2015, AGU Fall Meeting Abstracts

Cargill, P. J. 1994, ApJ, 422, 381

—. 2014, ApJ, 784, 49

Cargill, P. J., Bradshaw, S. J., & Klimchuk, J. A. 2012a, ApJ, 752, 161

—. 2012b, ApJ, 758, 5

Cargill, P. J., Warren, H. P., & Bradshaw, S. J. 2015, Philosophical Transactions of the Royal Society of London Series A, 373, 20140260

Carmichael, H. 1964, NASA Special Publication, 50, 451

Carrington, R. C. 1859, MNRAS, 20, 13

Caspi, A., Woods, T. N., & Warren, H. P. 2015, ApJ, 802, L2

Cassak, P. A., & Shay, M. A. 2012, Space Sci. Rev., 172, 283

Christe, S., Hannah, I. G., Krucker, S., McTiernan, J., & Lin, R. P. 2008, ApJ, 677, 1385

Christe, S., Glesener, L., Buitrago-Casas, C., et al. 2016, Journal of Astronomical Instrumentation, 5, 1640005

Christe, S., Krucker, S., Glesener, L., et al. 2017, ArXiv e-prints, arXiv:1701.00792

Christe, S. D., Shih, A., Rodriguez, M., et al. 2013, in Society of Photo-Optical Instrumentation Engineers (SPIE) Conference Series, Vol. 8862, Solar Physics and Space Weather Instrumentation V, 886206

Christensen, F. E., Hornstrup, A., Westergaard, N. J., et al. 1992, in Society of Photo-Optical Instrumentation Engineers (SPIE) Conference Series, Vol. 1546, Multilayer and Grazing Incidence X-Ray/EUV Optics, ed. R. B. Hoover, 160–167

Craig, I. J. D., & Brown, J. C. 1986, Inverse problems in astronomy: A guide to inversion strategies for remotely sensed data (CRC Press)

Crosby, N. B., Aschwanden, M. J., & Dennis, B. R. 1993, Sol. Phys., 143, 275

Culhane, J. L., Harra, L. K., James, A. M., et al. 2007, Sol. Phys., 243, 19

De Pontieu, B., McIntosh, S. W., Hansteen, V. H., & Schrijver, C. J. 2009, ApJ, 701, L1

De Pontieu, B., McIntosh, S. W., Carlsson, M., et al. 2011, Science, 331, 55

Del Zanna, G., Dere, K. P., Young, P. R., Landi, E., & Mason, H. E. 2015, A&A, 582, A56

Delaboudinière, J.-P., Artzner, G. E., Brunaud, J., et al. 1995, Sol. Phys., 162, 291

Dere, K. P., Landi, E., Mason, H. E., Monsignori Fossi, B. C., & Young, P. R. 1997, A&A, 125, doi:10.1051/aas:1997368

Drake, J. F., Shay, M. A., & Swisdak, M. 2008, Physics of Plasmas, 15, 042306

Edlén, B. 1943, Zeitschrift für Astrophysik, 22, 30

Emslie, A. G., Dennis, B. R., Shih, A. Y., et al. 2012, ApJ, 759, 71

Feldman, U. 1992, Physica Scripta Volume T, 46, 202

Filippov, B., Martsenyuk, O., Srivastava, A. K., & Uddin, W. 2015, Journal of Astrophysics and Astronomy, 36, 157

Fletcher, L., & Hudson, H. S. 2008, ApJ, 675, 1645

Fontenla, J. M., Avrett, E. H., & Loeser, R. 1990, ApJ, 355, 700

Freeland, S. L., & Handy, B. N. 1998, Sol. Phys., 182, 497

Gabriel, A. H. 1976, Philosophical Transactions of the Royal Society of London Series A, 281, 339

Giacconi, R., Reidy, W. P., Zehnpfennig, T., Lindsay, J. C., & Muney, W. S. 1965, ApJ, 142, 1274

Giacconi, R., & Rossi, B. 1960, JGR, 65, 773

Giacconi, R., Branduardi, G., Briel, U., et al. 1979, ApJ, 230, 540

Gibson, E. 1977, The quiet sun. (University of California Libraries)

Glesener, L., Krucker, S., Christe, S., et al. 2016, in Society of Photo-Optical Instrumentation Engineers (SPIE) Conference Series, Vol. 9905, Society of Photo-Optical Instrumentation Engineers (SPIE) Conference Series, 99050E

Gold, T. 1964, NASA Special Publication, 50, 389

Golub, L., Hartquist, T. W., & Quillen, A. C. 1989, Sol. Phys., 122, 245

Golub, L., Krieger, A. S., Silk, J. K., Timothy, A. F., & Vaiana, G. S. 1974, ApJ, 189, L93

Golub, L., Deluca, E., Austin, G., et al. 2007, Sol. Phys., 243, 63

Gorenstein, P. 2012, Optical Engineering, 51, 011010

Gosling, J. T. 1993, JGR, 98, 18937

Graham, D. R., Hannah, I. G., Fletcher, L., & Milligan, R. O. 2013, ApJ, 767, 83

Grefenstette, B. W., Glesener, L., Krucker, S., et al. 2016, ApJ, 826, 20

Grotrian, W. 1939, Naturwissenschaften, 27, 214

Handy, B. N., Acton, L. W., Kankelborg, C. C., et al. 1999, Sol. Phys., 187, 229

Hannah, I. G., Christe, S., Krucker, S., et al. 2008, ApJ, 677, 704

Hannah, I. G., Hudson, H. S., Battaglia, M., et al. 2011, Space Sci. Rev., 159, 263

Hannah, I. G., Hudson, H. S., Hurford, G. J., & Lin, R. P. 2010, ApJ, 724, 487

Hannah, I. G., Hurford, G. J., Hudson, H. S., Lin, R. P., & van Bibber, K. 2007, ApJ, 659, L77

Hannah, I. G., Grefenstette, B. W., Smith, D. M., et al. 2016, ApJ, 820, L14

Harrison, F. A., Christensen, F. E., Craig, W., et al. 2005, Experimental Astronomy, 20, 131

Harrison, F. A., Craig, W. W., Christensen, F. E., et al. 2013, ApJ, 770, 103

Harrison, R. A., Harra, L. K., Brković, A., & Parnell, C. E. 2003, A&A, 409, 755

Harrison, R. A., Sawyer, E. C., Carter, M. K., et al. 1995, Sol. Phys., 162, 233

Henriksson, G. 2009, in Astronomical Society of the Pacific Conference Series, Vol. 409, Cosmology Across Cultures, ed. J. Rubiño-Martín, J. Belmonte, F. Prada, & A. Alberdi, 166

Hill, S. M., Pizzo, V. J., Balch, C. C., et al. 2005, Sol. Phys., 226, 255

Hirayama, T. 1974, Sol. Phys., 34, 323

Hodgson, R. 1859, MNRAS, 20, 15

Holman, G. D. 1985, ApJ, 293, 584

Hoyng, P., Duijveman, A., Boelee, A., et al. 1981, ApJ, 244, L153

Hudson, H. S. 1991, Sol. Phys., 133, 357

Hudson, H. S., Acton, L. W., DeLuca, E. E., et al. 2012, in Astronomical Society of the Pacific Conference Series, Vol. 455, 4th Hinode Science Meeting: Unsolved Problems and Recent Insights, ed. L. Bellot Rubio, F. Reale, & M. Carlsson, 25

Hurford, G. J., Schmahl, E. J., Schwartz, R. A., et al. 2002, Sol. Phys., 210, 61

Iida, Y. 2012, PhD thesis, Univ. of Tokyo

Ishikawa, S., Saito, S., Tajima, H., et al. 2011, IEEE Transactions on Nuclear Science, 58, 2039

Ishikawa, S.-n., Glesener, L., Christe, S., et al. 2014, PASJ, 66, S15

Jansen, F., Lumb, D., Altieri, B., et al. 2001, A&A, 365, L1

Janvier, M. 2017, Journal of Plasma Physics, 83, 535830101

Kariyappa, R., Deluca, E. E., Saar, S. H., et al. 2011, A&A, 526, A78

Klimchuk, J. A. 2006, Sol. Phys., 234, 41

—. 2012, Journal of Geophysical Research (Space Physics), 117, A12102

—. 2015, Philosophical Transactions of the Royal Society of London Series A, 373, 40256

Klimchuk, J. A., & Bradshaw, S. J. 2014, ApJ, 791, 60

Klimchuk, J. A., Patsourakos, S., & Cargill, P. J. 2008, ApJ, 682, 1351

Koch, H. W., & Motz, J. W. 1959, Reviews of Modern Physics, 31, 920

Kontar, E. P., Brown, J. C., Emslie, A. G., et al. 2011, Space Sci. Rev., 159, 301

Kopp, R. A., & Pneuman, G. W. 1976, Sol. Phys., 50, 85

Kosugi, T., Makishima, K., Murakami, T., et al. 1991, Sol. Phys., 136, 17

Krucker, S., & Benz, A. O. 1998, ApJ, 501, L213

—. 2000, Sol. Phys., 191, 341

Krucker, S., Benz, A. O., Bastian, T. S., & Acton, L. W. 1997, ApJ, 488, 499

Krucker, S., Hudson, H. S., Glesener, L., et al. 2010, ApJ, 714, 1108

Krucker, S., Hurford, G. J., MacKinnon, A. L., Shih, A. Y., & Lin, R. P. 2008, ApJ, 678, L63

Krucker, S., Christe, S., Glesener, L., et al. 2013, in Society of Photo-Optical Instrumentation Engineers (SPIE) Conference Series, Vol. 8862, Solar Physics and Space Weather Instrumentation V, 88620R

Kuhar, M., Krucker, S., Hannah, I. G., et al. 2017, ApJ, 835, 6

Lemen, J. R., Title, A. M., Akin, D. J., et al. 2012, Sol. Phys., 275, 17

Lin, R. P. 1974, Space Sci. Rev., 16, 189

—. 2011, Space Sci. Rev., 159, 421

Lin, R. P., Feffer, P. T., & Schwartz, R. A. 2001, ApJ, 557, L125

Lin, R. P., & Hudson, H. S. 1976, Sol. Phys., 50, 153

Lin, R. P., Dennis, B. R., Hurford, G. J., et al. 2002, Sol. Phys., 210, 3

López Fuentes, M., & Klimchuk, J. A. 2016, ApJ, 828, 86

Madsen, K., Alexander, D., Bhalerao, V., et al. 2011, in AAS/High Energy Astrophysics Division, Vol. 12, AAS/High Energy Astrophysics Division, 43.08

Madsen, K. K., Harrison, F. A., Markwardt, C. B., et al. 2015, ApJS, 220, 8

Mallette, L. A. 1982, in 9th Communications Satellite Systems Conference, ed. W. F. Rector, III, 541–547

Maran, S. P. 2001, Physics Today, 54, 54

Masuda, S., Kosugi, T., Hara, H., Tsuneta, S., & Ogawara, Y. 1994, Nature, 371, 495

McIntosh, S. W., de Pontieu, B., Carlsson, M., et al. 2011, Nature, 475, 477

McTiernan, J. M. 2009, ApJ, 697, 94

Miceli, M., Reale, F., Gburek, S., et al. 2012, A&A, 544, A139

Mitsuda, K., Bautz, M., Inoue, H., et al. 2007, PASJ, 59, S1

Mullan, D. 2009, Physics of the Sun, doi:10.1201/b15843

Oka, M., Krucker, S., Hudson, H. S., & Saint-Hilaire, P. 2015, ApJ, 799, 129

Parker, E. N. 1957, JGR, 62, 509

—. 1983, ApJ, 264, 642

—. 1988, ApJ, 330, 474

Parnell, C. E., & De Moortel, I. 2012, Philosophical Transactions of the Royal Society of London Series A, 370, 3217

Parnell, C. E., & Jupp, P. E. 2000, ApJ, 529, 554

Peres, G., Orlando, S., Reale, F., Rosner, R., & Hudson, H. 2000, ApJ, 528, 537

Peterson, L., & Winckler, J. R. 1958, Physical Review Letters, 1, 205

Petrosian, V., & Liu, S. 2004, ApJ, 610, 550

Petschek, H. E. 1964, NASA Special Publication, 50, 425

Phillips, K. 1995, Guide to the Sun (Cambridge University Press)

Phillips, K. J. H. 2004, ApJ, 605, 921

Priest, E., & Forbes, T., eds. 2000, Magnetic reconnection : MHD theory and applications (Cambridge University Press)

Ramaty, R., Mandzhavidze, N., Kozlovsky, B., & Murphy, R. J. 1995, ApJ, 455, L193

Ramsey, B. D., Alexander, C. D., Apple, J. A., et al. 2002, ApJ, 568, 432

Raymond, J. C., Krucker, S., Lin, R. P., & Petrosian, V. 2012, Space Sci. Rev., 173, 197

Reale, F., McTiernan, J. M., & Testa, P. 2009, ApJ, 704, L58

Reale, F., & Orlando, S. 2008, ApJ, 684, 715

Reames, D. V. 1999, Space Sci. Rev., 90, 413

Reep, J. W., Bradshaw, S. J., & Klimchuk, J. A. 2013, ApJ, 764, 193

Reeves, K. K., McCauley, P. I., & Tian, H. 2015, ApJ, 807, 7

Rutherford, E. 1911, Phil. Mag. Ser.6, 21, 669

Schmelz, J. T., & Pathak, S. 2012, ApJ, 756, 126

Schmelz, J. T., Kashyap, V. L., Saar, S. H., et al. 2009, ApJ, 704, 863

Schwabe, M. 1844, Astronomische Nachrichten, 21, 233

Sheeley, Jr., N. R., & Golub, L. 1979, Sol. Phys., 63, 119

Shimizu, T. 1995, PASJ, 47, 251

Shimojo, M., & Shibata, K. 1999, ApJ, 516, 934

Smith, D. M., Lin, R. P., Turin, P., et al. 2002, Sol. Phys., 210, 33

Somov, B. V., & Kosugi, T. 1997, ApJ, 485, 859

Srivastava, A. K., Shetye, J., Murawski, K., et al. 2017, Scientific Reports, 7, 43147

Sturrock, P. A. 1966, Nature, 211, 695

Su, Y., Veronig, A. M., Holman, G. D., et al. 2013, Nature Physics, 9, 489

Sun, J. Q., Cheng, X., Ding, M. D., et al. 2015, Nature Communications, 6, 7598

Sweet, P. A. 1958, in IAU Symposium, Vol. 6, Electromagnetic Phenomena in Cosmical Physics, ed. B. Lehnert, 123

Sylwester, J., Kuzin, S., Kotov, Y. D., Farnik, F., & Reale, F. 2008, Journal of Astrophysics and Astronomy, 29, 339

Takakura, T., Tsuneta, S., Nitta, N., et al. 1983, ApJ, 270, L83

Tobias, S. M. 2002, Philosophical Transactions of the Royal Society of London Series A, 360, 2741

Tripathi, D., Klimchuk, J. A., & Mason, H. E. 2011, ApJ, 740, 111

Tsuneta, S., & Naito, T. 1998, ApJL, 495, L67

Ugarte-Urra, I., & Warren, H. P. 2014, ApJ, 783, 12

van Beek, H. F., Hoyng, P., Lafleur, B., & Simnett, G. M. 1980, Sol. Phys., 65, 39

Veronig, A., Temmer, M., Hanslmeier, A., Otruba, W., & Messerotti, M. 2002, A&A, 382, 1070

Veronig, A. M., & Brown, J. C. 2004, ApJL, 603, L117

Viall, N. M., & Klimchuk, J. A. 2012, ApJ, 753, 35

Viall, N. M., & Klimchuk, J. A. 2015a, in AAS/AGU Triennial Earth-Sun Summit, Vol. 1, AAS/AGU Triennial Earth-Sun Summit, 213.03

—. 2015b, ApJ, 799, 58

Walker, Jr., A. B. C., Lindblom, J. F., Barbee, Jr., T. W., & Hoover, R. B. 1988, Science, 241, 1781

Warren, H. P., Brooks, D. H., & Winebarger, A. R. 2011, ApJ, 734, 90

Warren, H. P., Winebarger, A. R., & Brooks, D. H. 2012, ApJ, 759, 141

Warren, H. P., Winebarger, A. R., & Mariska, J. T. 2003, ApJ, 593, 1174

Weisskopf, M. C., Tananbaum, H. D., Van Speybroeck, L. P., & O'Dell, S. L. 2000, in Society of Photo-Optical Instrumentation Engineers (SPIE) Conference Series, Vol. 4012, X-Ray Optics, Instruments, and Missions III, ed. J. E. Truemper & B. Aschenbach, 2–16

Withbroe, G. L., & Noyes, R. W. 1977, ARA&A, 15, 363

Wolter, H. 1951a, Annalen der Physik, 444, 65

—. 1951b, Annalen der Physik, 444, 57

Zharkova, V. V., Arzner, K., Benz, A. O., et al. 2011, Space Sci. Rev., 159, 357

Zweibel, E. G., & Yamada, M. 2009, ARA&A, 47, 291